DISSERTATION FOR THE DEGREE OF DOCTOR OF PHILOSOPHY (PHD)

EGR2 is an epigenomic regulator of alternative macrophage polarization and a nexus modulator of alveolar macrophage-related antifungal immunity

by Zsuzsanna Kolostyak MD

Supervisor: Laszlo Nagy MD, PhD, DSc, MHAS

UNIVERSITY OF DEBRECEN
DOCTORAL SCHOOL OF MOLECULAR CELLULAR AND IMMUNE BIOLOGY

DEBRECEN, 2025

Table of Contents

I. Abbreviations

ACK - Ammonium-Chloride-Potassium

AF – *Aspergillus fumigatus*

AIDS - Acquired Immunodeficiency Syndrome

AM - alveolar macrophage

AP-1 - Activator Protein 1

APC – antigen presenting cell

ARA - arachidonic acid

ATAC-seq - Assay for Transposase-Accessible Chromatin using sequencing

ATP – adenosine triphosphate

BAL - bronchoalveolar lavage

BALF - bronchoalveolar lavage fluid

BCA - bicinchoninic acid

BHLHE40 - Basic Helix-Loop-Helix Family Member E40

BMDM - bone marrow-derived macrophage

BOOP - bronchiolitis obliterans with organizing pneumonia

bp - base pair

BRD4 - Bromodomain Containing 4

BSL2 - biosafety level 2

C5a - Complement component 5a

CCD - Charge-coupled Device

CD – cluster of differentiation

C/EBP - CCAAT-enhancer-binding Protein

CCL - C-C Motif Chemokine Ligand

cDNA- complementary DNA

CFU - colony-forming unit

ChIP-seq - Chromatin immunoprecipitation coupled with sequencing

CLR - C-type lectin receptor

COX - Cyclooxygenase

CP - cyclophosphamide

CV - coefficient of variation

CXCL - C-X-C motif chemokine

CSF - Colony Stimulating Factor

CT – computed tomography

CUT&RUN - Cleavage Under Targets and Release Using Nuclease

DAMP – damage-associated molecular pattern

DAR - differentially accessible region

DC – dendritic cell

DEG - differentially expressed gene

DMEM - Dulbecco's Modified Eagle Medium

DMSO - dimethyl sulfoxide

DNA - Deoxyribonucleic acid

DOX - doxycyclin

ECAR - extracellular acidification rate

ECM – extracellular matrix

EDTA - ethylenediaminetetraacetic acid

EGR2 - Early Growth Response 2

ELISA - enzyme-linked immunosorbent assay

ENCODE - Encyclopedia of DNA Elements

eRNA - enhancer RNA

ESC – embryonic stem cell

FBS - Fetal Bovine Serum

FDR - false discovery rate

FGF - Fibroblast Growth Factor

FOXP3 - Forkhead box P3

FPKM - Fragments Per Kilobase of transcripts per Million mapped reads

FPR2 - Formyl Peptide Receptor 2

GAS - gamma-activated sequences

GEO - Gene Expression Omnibus

GM-CSF - Granulocyte-Macrophage Colony-Stimulating Factor

GPCR - G-protein Coupled Receptor

H&E - hematoxylin and eosin

HETE - hydroxyeicosatetraenoic acid

HPLC - high-performance liquid chromatography

HSC – haemopoetic stem cell

ID2 - Inhibitor Of DNA Binding 2

IFNγ- Interferon γ

IFNγR - Interferon γ Receptor

IgG – Immunoglobulin G

IGV - Integrative Genomic Viewer

IKK - Inhibitory κB kinase

IL – Interleukin

iNOS – Inducible Nitric Oxide Synthase

IM – interstitial macrophage

IRF - Interferon Regulatory Factor

JAK - Janus kinase

KAR - Killer Activating Receptor

kbp - kilobase pair

KEGG - Kyoto Encyclopedia of Genes and Genomes

KLF4 - Krüppel-Like Factor 4

KO - knock-out

LC-MS/MS - Liquid Chromatography with tandem Mass Spectrometry

LDTF - lineage-determining transcription factor

LDH - lactate dehydrogenase

LIF - Leukemia Inhibitory Factor

LOX - lipoxygenase

LPS - lipopolysaccharide

LTA4H - Leukotriene A4 Hydrolase

LT - leukotriene

LX - lipoxane

LysCre - lysozyme-Cre

MAPK - Mitogen-Activated Protein Kinase

MAR1 – Maresin 1

MCP-1 - Monocyte Chemoattractant Protein-1

MCSF - Macrophage Colony-stimulating Factor

MDA5 - Anti-melanoma Differentiation-Associated protein 5

MDS - multi-dimensional scaling

MFI - median fluorescence intensity

MHC – major histocompatibility complex

MMP - Matrix Metalloproteinase

MPO – myeloperoxidase

MR - Mannose Receptor

MRM - multiple reaction monitoring

mRNA - messenger RNA

NA - numeric aperture

NADPH - nicotinamide adenine dinucleotide phosphate

ncRNA – non-coding RNA

NF-κB - Nuclear Factor κB

NGS – Next-generation sequencing

NK – natural killer

NLR - NOD-like Receptor

NO – nitric oxide

NOD - Nucleotide-binding Oligomerization Domain

NOS - Nitric Oxide Synthases

OCR - oxygen consumption rate

PAMP - pathogen-associated molecular pattern

PAS – periodic acid–Schiff

PBS - Phosphate Buffered Saline

PCR – polymerase chain reaction

PDGF - Platelet-Derived Growth Factor

PFA - paraformaldehyde

PG - prostaglandin

PI - phosphatidyl-inositol

PMN - polymorphonuclear cell

PPARγ - Peroxisome Proliferator-Activated Receptor Gamma

PRR - pathogen recognition receptor

PU.1 - Purine Rich Box-1

PUFA - polyunsaturated fatty acid

QC – quality control

RIG-I - Retinoic acid-Inducible Gene I

RLR - RIG-I-like Receptor

RNA – ribonucleic acid

RNA-seq - RNA-sequencing

ROS - reactive oxygen species

RPKM - Reads Per Kilobase of transcript, per Million mapped reads

rRNA – ribosomal RNA

RT-qPCR - real-time quantitative polymerase chain reaction

RUNX - Runt-Related Transcription Factor

RV – Resolvin

SNP - Single Nucleotide Polymorphisms

SPE - solid-phase extraction

SPF - specific pathogen-free

STAT – Signal Transducer and Activator of Transcription

TAM – tumor-assoiated macrophage

TGF-β - Transforming Growth Factor β

Th – T helper

TIMP - tissue inhibitors of metalloproteinase

TLR - Toll-like receptor

TNFα – Tumor Necrosis Factor α

TRIF - TIR domain-containing adaptor inducing interferon-β

TSS - transcription start site

TTBS - Tween-Tris-buffered saline

TX - thromboxane

UTR - untranslated region

V-ATPase - Vacuolar-type ATPase

VEGF - Vascular Endothelial Growth Factor

WT - wild-type

II. Introduction

Macrophages are dominant parts of innate immune system and create the first line of protection against different pathogens. The adaptive action of macrophages is a result of a rapid and plastic environment-induced response based on special epigenomic, gene expressional and functional program. The gene expression of macrophages is regulated by three main ways. First, a permanent developmental program established by lineage-determining transcription factors (LDTFs) such as Purine Rich Box-1 (PU.1), CCAAT/enhancer binding protein (C/EBP), and Activating Protein-1 (AP-1). Second, an adaptation to surrounding microenvironment by polarization signals (Amit 2016; Guilliams 2020; Atri 2018; Figure 1) influencing transcription factors activity (Bonnardel 2019); i.e. interleukin 4 (IL-4) or interleukin 13 (IL-13) via the activation of signal transducer and activator of transcription 6 (STAT6). The third regulatory mechanism takes place transiently following pathogen exposition or inflammation stimuli (Glass and Natoli 2016).

The internal surfaces of lung are directly being encountered to inhaled air pollutants and bacterial, viral or fungal pathogens. The tissue resident alveolar macrophages (AMs) associate with the bronchoalveolar epithelial lining. They pivotal roles are the recognition and elimination of pathogens and harmful agents, and parallelly they initiate the inflammatory response. AMs recognize the pathogen-associated molecular patterns (PAMPs) of targets by pathogen recognition receptors (PRRs). Next, AMs internalize the bound particles by phagocytosis and inactivate the microbes in phagolysosomes. The intracellular killing of pathogens based on lysosome acidification, reactive oxygen species (ROS) formation, and enzymatic degradation (Palstra 2012).

In turn, the induced downstream inflammation-associated signaling cascades through complex transcriptional regulatory steps lead to diverse proinflammatory cytokine production and numerous lipid mediator secretion, which orchestrate the multicellular response of acute

inflammation of the lung. Finally, AMs, as the gatekeepers of lung tissue homeostasis, switch to resolving phenotype and take part in the regeneration of injured lung (Allard 2018). The coordinated action of immune mechanisms is sufficient to create defense against infective agents. However, the inadequate program of molecular and cellular events leads to manifest diseases such as pneumonitis, pneumonia, acute lung injury or chronic inflammatory pathologies, and pulmonary fibrosis (Herold 2011, Figure 2).

In our study we focused on the details of alternative macrophage polarization mechanisms and based on our primary results we followed our work with the examination of Early Growth Response 2 (EGR2) mediated changes in AMs.

III. Theoretical background

Innate immunity – The first line of defense against pathogens

The innate immune system is the body's primary defense mechanism against pathogens, providing immediate but non-specific responses to invading microorganisms. It plays a vital role in controlling infections, initiating adaptive immune responses, and maintaining tissue homeostasis. The recognition of different agents based on the detection of conserved molecular patterns associated with pathogens (pathogen-associated molecular patterns, PAMPs) or damaged cells (damage-associated molecular patterns, DAMPs).

There are four key cell types in innate immunity, the macrophages and neutrophil granulocytes/polymorphonuclear cells (PMNs) as the phagocytes, the natural killer (NK) cells and the dendritic cells (DCs). The macrophages reside in different tissues and engulf pathogens, different substances and debris through different mechanism of endocytosis and secrete cytokines and chemokines that orchestrate the immune response (Shapouri-Moghaddam 2018). The PMNs in addition to phagocytotic activity, release a variety of enzymes and toxic chemicals, such as lysozymes and ROS, that kill and break down the invaders (Liew 2019).

NK cells are cytotoxic lymphocytes fulfill critical roles in immune surveillance by recognizing stress signals through Killer Activating Receptors (KARs). This recognition triggers their activation, leading to cytotoxicity, cytokine production, and immunomodulation, all of which are crucial for effective defense against infections and tumorigenesis (Caligiuri 2008).

DCs act as professional antigen-presenting cells (APCs) that capture and process pathogens, then migrate to lymph nodes where they activate the adaptive immune response by presenting the special antigens to T lymphocytes (Collin and Ginhoux 2019)

Upon detection of pathogens, the innate immune system triggers an inflammatory response, which serves to isolate and eliminate the threat. The complex cellular and humoral response lead to vasodilation and increased vascular permeability allowing different immune cells, proteins, nutrients and other signal molecules to immigrate and exit to the site of infection.

The innate immune system plays a critical role in shaping the adaptive immune response by presenting antigens and releasing cytokines, DCs and other innate immune components activate T and B cells, which are essential for a targeted response to specific pathogens. This interaction establishes immunological memory, providing long-term protection against previously encountered pathogens.

Finally, after termination of pathogen elimination and inflammation, the innate immune cells take part in the regeneration of damaged tissue.

Diversity and importance of macrophages

The diversity of macrophages arises from their ability to respond to a wide variety of environmental signals, allowing them to specialize and perform distinct functions in different tissues and contexts.

Tissue-resident macrophages such as microglia, Kupffer cells, Langerhans cells, and alveolar macrophages (AMs) are primarily derived from yolk sac progenitors or fetal liver monocytes during embryogenesis. These cells seed tissues before birth and undergo self-renewal, largely exempt from adult hematopoiesis. In adults, circulating monocytes, derived from bone marrow hematopoietic stem cells, can be recruited to tissues, where they differentiate into macrophages in response to inflammatory cues. This monocyte infiltration is crucial during immune response and tissue repair, enabling macrophage population turnover and enhancement.

While there are numerous common treats of different macrophage populations such as initiation of inflammatory response, engulfment of pathogens or debris and resolution of inflammation, based on tissue localization, they also fulfill specific functions (Lazarov 2023). For example, AMs regulate surfactant homeostasis of lung, Kupffer cells of liver are involved in blood filtration, microglia cells in the central nervous system participate in synaptic pruning and immune surveillance, and the osteoclasts are specialized to resorb bone.

From the aspect of activation and polarization, macrophages demonstrate extreme plasticity influenced by the cytokine milieu and tissue microenvironment. However, the polarization state of macrophages represents a wide spectrum, canonically the literature distinguishes the two end points, the classical polarization state or "M1 phenotype" via the activation of Toll-Like Receptor (TLR) or different inflammatory cytokine signaling pathways such as interferon γ (IFNγ), and the alternative polarization state or "M2 phenotype" induced by microenviromental IL-4 or IL-13 cytokines (Murray et al. 2014). Functionally, classically polarized macrophages exhibit high microbicidal activity through the production of pro-inflammatory cytokines (e.g., Tumor Necrosis Factor α (TNF-α), interleukin-1 β (IL-1β), interleukin-6 (IL-6), ROS and nitrogen species (NOS), while the alternatively polarized macrophages act in parasitic infections, support wound healing mechanisms, support the resolution of inflammation and maintenance of tissue integrity (Shapouri-Moghaddam 2018).

Depending on the phenotypical status of macrophages, they can either promote or block the progression of different pathological processes. The tumor-associated macrophages (TAMs) influenced by the surrounding microenvironment can enhance tumor progression through i.e. angiogenesis, tissue remodeling, and immunosuppression or exhibit anti-tumor activity by fighting against malignantly transformed cells (Pan 2020). Especially the alternatively polarized macrophages contribute to the development of tissue fibrosis by producing fibrogenic mediators that activate fibroblasts and lead to excessive deposition of

extracellular matrix components such as fibrin (Wynn 2016). In autoimmune illnesses they have also dual roles. While they can act as effector cells driving autoimmune pathology, regulatory macrophages can also help resolve autoimmune responses by promoting tissue repair and modulating adaptive immune functions. The complexity and adaptability of macrophage roles, making them integral players in both maintaining tissue homeostasis and mediating disease pathogenesis.

The regulation of macrophage phenotype

Macrophage phenotype regulation is a dynamic process influenced by a combination of intrinsic and extrinsic factors. This regulation allows macrophages to adapt to diverse physiological and pathological contexts, thereby performing specialized functions ranging from host defense to tissue repair and homeostasis.

First, the cytokine environment largely modulates the macrophage phenotype. Pro-inflammatory cytokines such as IFN-γ and TNF-α, along with microbial products like lipopolysaccharide (LPS), promote the classical activation or M1 phenotype. IFN-γ binds to its receptor (IFN-γR), and activating the Janus Kinase/Signal Transducer and Activator of Transcription 1 (JAK/STAT1) signaling pathway. The phosphorylated STAT1 transcription factor undergos nuclear translocation, and the STAT1 homodimers bind to gamma-activated sequences (GAS) in the promoter regions of target genes inducing the expression of key M1-associated genes, including inducible nitric oxide synthase (iNOS) and various inflammatory cytokines. Engagement of TLRs by PAMPs, such as LPS interacting with TLR4, initiates downstream signaling through MyD88- and TIR domain-containing adaptor inducing interferon-β (TRIF)-dependent pathways, leading to Nuclear Factor κB (NF-κB) and Mitogen-Activated Protein Kinase (MAPK) activation, which are crucial for the transcription of pro-

inflammatory mediators. NF-κB activation is tightly regulated by Inhibitory κB kinase (IKK) complexes and subsequent proteasomal degradation of IκB proteins.

The interleukin 10 (IL-10) and Transforming Growth Factor β (TGF-β) cytokines are involved in dampening inflammation and promoting macrophage transition to a more regulatory or resolving phenotype. They inhibit key pathways (e.g., NF-κB, STAT1) and can induce alternative activation markers (Shapouri-Moghaddam 2018, Atri 2018).

The cytokines IL-4 and IL-13 initiate a signaling cascade which lead a phosphorylation of STAT6 transcription factor which mediates the downstream gene expression program of alternative polarization. The binding of DNA by STAT6 changes the expression of hundreds of target genes during the first few hours of stimulation, moreover it influences the level of several transcription factors. The DNA-binding of STAT6 is just a transient action, the majority of STAT6 is released from the affected chromatin regions after 24 hours of cytokine exposure (Czimmerer 2018).

The STAT6-induced transcription factors have been proved as fundamental mediators of the M2 macrophage phenotype, such as the peroxisome proliferator-activated receptor γ (PPARγ) (Odegaard 2007), Interferon Regulatory Factor 4 (IRF4) (Satoh 2010), Krüppel-Like Factor 4 (KLF4) (Liao 2011), MYC (Pello 2012), and Basic Helix-Loop-Helix Family Member E40 (BHLHE40) (Jarjour 2019).

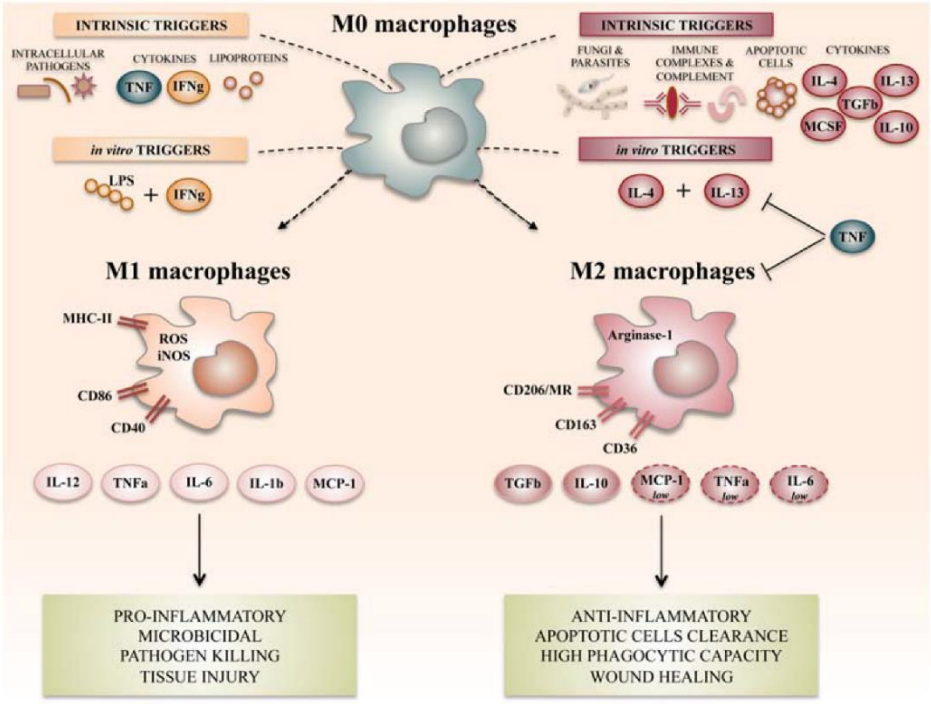

Figure 1. The summary of M1 and M2 macrophage polarization (taken from: Atri et al. 2018, https://www.mdpi.com/1422-0067/19/6/1801)

In addition to cytokines, other factors in tissue microenvironment have impact in macrophage phenotype. During hypoxia the low oxygen levels (often present in tumors or injured tissues) can drive macrophages towards a phenotype that supports angiogenesis and tissue repair, often resembling M2-like characteristics. Local metabolites such as lactate or adenosine can also influence macrophage function promoting an immunoregulatory or pro-repair state in inflammation-resolution contexts and the composition and integrity of the extracellular matrix impact macrophage behavior, with specific matrix proteins or fragments acting as signals for activation or resolution pathways (Shapouri-Moghaddam 2018).

Finally, lipid mediators also play crucial roles in regulating macrophage function. These mediators are derived from polyunsaturated fatty acids (PUFAs) and act through specific receptors to initiate or resolve inflammatory processes. Prostaglandins (PGs) are primarily derived from arachidonic acid (ARA) via the cyclooxygenase (COX) pathway, PGs like PGE2 have complex roles but generally promote inflammation. PGE2 can enhance macrophage

migration to inflammatory sites and modulate their cytokine production. It has dual action on a context dependent manner, it is able promoting resolution through increased secretion of anti-inflammatory cytokines like IL-10.

Leukotrienes (LTs) are also ARA derivatives synthetized through the lipoxygenase (LOX) pathway. They are potent chemoattractants, i.e. LTB4 enhances the recruitment of macrophages and other leukocytes to the sites of inflammation, amplifies inflammatory responses, and enhance the phagocytic activity of cells (Vassiliou 2023).

Lipoxins, resolvins, protectins and maresins are anti-inflammatory and pro-resolving lipid mediators. They generally inhibit macrophage migration and pro-inflammatory cytokine production, promote the resolution of inflammation by enhancing macrophage-mediated efferocytosis (uptake and clearance of apoptotic cells), and promote macrophage-mediated tissue repair and regeneration (Videla 2023).

Lipid mediators act through specific G-protein coupled receptors (GPCRs) on macrophages. For example, lipoxane A4 (LXA4) acts through the Formyl Peptide Receptor 2 (FPR2) to mediate its effects, while resolvins act through receptors like ChemR23 and GPR32. By interacting with their receptors, these lipid mediators influence NF-κB and MAPK pathways affecting the transcription of genes involved in inflammation and resolution.

Gaining a deeper understanding of these regulatory mechanisms opens up potential pathways for developing therapeutic interventions. These strategies aim to bolster the host's defense against infections and tumors while also addressing chronic inflammatory conditions. By focusing on the modulation of macrophage phenotypes, these interventions can promote either the deactivation of pro-inflammatory states or the switching of macrophages to more beneficial phenotypes that support tissue repair and resolution of inflammation. This approach has the potential to improve patient outcomes by optimizing the immune response to various pathogens and diseases.

The differentiation and function of alveolar macrophages

AMs are specialized immune cells located in the alveoli of the lungs. They play a crucial role in maintaining pulmonary homeostasis and defending the respiratory system against inhaled pathogens and particulates.

AMs embryonically derived by fetal liver. During embryonic development the fetal liver monocytes translocate to the parenchyma of fetal lung at embryonic day 13.5-14.5 (Hoeffel 2012; Guilliams 2013). Here, the local microenvironment, especially the presence of two cytokine, the Granulocyte-Macrophage Colony-Stimulating Factor (GM-CSF) and the TGF-β lead the maturation of pre-AM stage through the activation of PU.1, Runt-Related Transcription Factor 3 (RUNX3), PPARγ, and Inhibitor Of DNA Binding 2 (ID2) transcription factors (Shibata 2001; Yu 2017; Schneider 2014). The maturation of AMs terminates after birth around at 4-month-old age (Cohen 2018). The terminally mature and functional AMs show the expression of CD45 as a general immune cell marker, the F4/80 and CD11c as a macrophage marker and the SiglecF as a specific AM surface marker protein, however constant downregulation and finally the loss of CD11b expression occurs during the maturation process (Ginhoux et al. 2014).

The well-differentiated AMs are capable to supply widespread functions. They provide alveolar clearance through the recognition and elimination of inhaled pathogens, detoxifying air pollutants and regulate the surfactant homeostasis. They detect chemotactic signals released at sites of infection or tissue damage, including substances such as chemokines (e.g., C-X-C Motif Chemokine Ligand 8 (CXCL8), complement fragments (e.g., Complement component 5a (C5a), and formyl peptides or other PAMPs originate from different microbes. AMs utilize several distinct classes of PRRs to identify invading agents. TLRs are found on the cell surface (TLR 1, 2, 4, 5, 6) and within endosomal compartments (TLR 3, 7, 8, 9). TLR4 recognizes LPS from gram-negative bacteria, TLR2 binds peptidoglycan from bacterial cell

walls and TLR3 is specialized for double-stranded RNA from viruses (Kovach 2011). C-type Lectin Receptors (CLRs) bind carbohydrates and are essential for recognizing fungal and some bacterial pathogens. Dectin-1 identify β-glucans and zymosan from fungal cell walls while mannose receptor (MR/CD206) binds mannose-rich glycoproteins, facilitating the uptake of microbes and apoptotic cells (Hou 2017). NOD-like receptors (NLRs) are cytoplasmic receptors that respond to intracellular pathogens and stress signals. Nucleotide-binding Oligomerization Domain 1 and 2 (NOD1 and NOD2) recognize specific peptidoglycan motifs from bacterial cell walls and activate signaling pathways leading to inflammation (Snaka and Fasel 2020). RIG-I-like Receptors (RLRs) such as Retinoic acid-Inducible Gene I (RIG-I) and Anti-melanoma Differentiation-Associated protein 5 (MDA5) detect different types of viral RNA, leading to the production of type I interferons and an antiviral response (Onomoto 2021).

Upon ligand binding, PRRs activate various intracellular signaling pathways that lead to the expression of pro-inflammatory cytokines and chemokines. The MyD88-dependent pathway is mainly used by TLRs (except TLR3) and involves the recruitment of the MyD88 adapter protein, leading to the activation of transcription factors like NF-κB, which promotes the expression of inflammatory genes. The TRIF-dependent pathway is utilized by TLR3 and TLR4, this pathway activates IRF3, leading to the production of type I interferons. NLRs may form inflammasomes that activate caspase-1 and lead to the maturation and secretion of pro-inflammatory cytokines such as IL-1β and Interleukin 18 (IL-18).

In addition to PPRs which directly bind the microbial PAMPs, AMs are also recognize opsonized surfaces Fc receptors and complement receptors (CRs). As a result of activation by PRRs, Fc receptors or CRs, the AMs start to engulf the identified particles.

Binding to the target activates intracellular signaling pathways that lead to actin polymerization at the site of contact. This cytoskeletal reorganization results in the formation

of pseudopodia. The pseudopodia extend around the target particle, eventually enclosing it completely, forming a sealed phagosome. This process is facilitated by dynamic membrane remodeling and the involvement of phagocytic cup proteins. The next step is phagosome maturation**.** The nascent phagosome sequentially fuses with early endosomes, late endosomes, and ultimately lysosomes to form a phagolysosome. This process involves changes in pH, the acquisition of Vacuolar-type ATPase (V-ATPase) to acidify the phagosomal lumen, and the delivery of proteolytic enzymes and antimicrobial peptides into the phagosome. Within the acidic environment of the phagolysosome, a range of enzymes such as proteases, lipases, nucleases, and glycosidases work to degrade the phagocytosed material completely. The phagosome membrane NADPH oxidase complex generates ROS which are crucial for microbial killing and Nitric Oxide (NO), produced by iNOS, can react further to form various nitrosating agents contributing to antimicrobial activity. Indigestible material that cannot be further degraded accumulates within the phagolysosome in structures known as residual bodies. These remnants are eventually expelled from the cell via exocytosis (Brown 2023).

AMs process and present antigens on their surface using MHC molecules. This presentation is crucial for the activation of T lymphocytes, linking innate and adaptive immune responses. By presenting antigens, these macrophages help activate CD4+ Th cells, which orchestrate a more tailored immune response.

AMs also modulate levels of pulmonary surfactant by phagocytosing surfactant components, aiding in both their recycling and degradation. This regulation is vital for maintaining low alveolar surface tension and stability.

After phagocytosis, surfactant components are delivered to lysosomes where they can be broken down. Lipid components are hydrolyzed by lysosomal enzymes, and proteins are degraded to amino acids. Some breakdown products, especially lipids, may be recycled and reused by alveolar type II cells for the synthesis of new surfactant.

AMs secrete cytokines and other signaling molecules that can modulate surfactant production by alveolar type II cells. For example, certain cytokines can influence the proliferation and activity of type II cells, thereby impacting surfactant synthesis and secretion (Trapnell 2002).

In response to lung injury or inflammation, they can enhance their uptake of damaged surfactant and cellular debris, helping maintain alveolar stability and function during the repair process. On the other hand, they fulfill a dominant role in other mechanisms of tissue repair and remodeling following lung injury. They engage in the active removal of apoptotic cells, extracellular debris, and damaged cellular components through efferocytosis. This clearance is crucial to prevent secondary necrosis and promote a conducive environment for tissue regeneration. The efferocytosis, triggers anti-inflammatory responses, further reinforcing the transition from injury to repair. During resolution of inflammation AMs shift their cytokine profile from pro-inflammatory to anti-inflammatory (Herold 2011).

They release IL-10 and TGF-β, which reduce the recruitment and activation of additional immune cells. The synthesis of lipid mediators such as lipoxins and resolvins supporting to terminate the inflammatory response and promote healing. Growth factors secreted by alveolar macrophages, such as TGF-β, platelet-derived growth factors (PDGFs), and fibroblast growth factors (FGFs), play pivotal roles in stimulating epithelial and endothelial cell proliferation and migration, which are vital for repairing damaged tissue. Vascular endothelial growth factors (VEGFs) released by macrophages facilitates the formation of new blood vessels, enhancing oxygen and nutrient supply to the regenerating tissue, which is critical for healing.

Macrophages produce matrix metalloproteinases (MMPs) that degrade damaged extracellular matrix (ECM) components, clearing the path for tissue reconstruction. They also produce tissue inhibitors of metalloproteinases (TIMPs) to regulate MMP activity, ensuring

that matrix degradation and formation are balanced and remodeling proceeds without excessive tissue destruction. By engaging fibroblasts via cytokines like IL-4 and IL-13, alveolar macrophages encourage fibroblast proliferation and ECM production, necessary for structural support and tissue integrity (Cheng 2021).

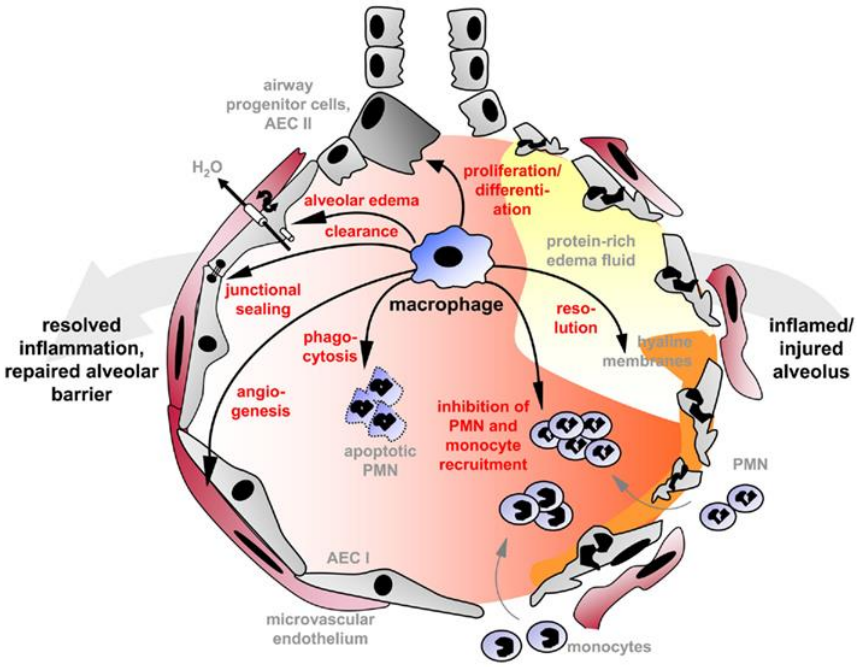

Figure 2. The roles of AMs during lung injury (taken from: Herold et al. 2011, https://www.frontiersin.org/files/Articles/14194/fimmu-02-00065-HTML/image_m/fimmu-02-00065-g001.jpg)

In summary, alveolar macrophages serve multifaceted roles that are crucial for respiratory immune defense, maintaining homeostasis, and facilitating repair processes. Their ability to switch between pro-inflammatory and anti-inflammatory roles depending on the context underscores their importance in the dynamic environment of the lung.

Invasive *aspergillosis*

Invasive *aspergillosis* is a severe fungal infection primarily caused by the species *Aspergillus fumigatus (AF)*, although other species such as *Aspergillus flavus*, *Aspergillus niger*, and *Aspergillus terreus* can also be involved. These fungi are ubiquitous in the environment, particularly in decaying organic matter and soil. Inhalation of airborne conidia

(spores) is the primary route of entry into the human body. The spores are usually cleared by a competent immune system; however, they can germinate and invade tissues in immunocompromised hosts.

The incidence of invasive *aspergillosis* has increased, particularly among patients with hematological malignancies, hematopoietic stem cell (HSC) transplants, solid organ transplants, and those undergoing prolonged immunosuppressive therapies. It is also seen in patients with advanced acquired immunodeficiency syndrome (AIDS) and severe neutropenia.

The lungs are the most affected site, leading to pulmonary invasive *aspergillosis*. Key clinical symptoms include persistent fever despite broad-spectrum antibiotic therapy, pleuritic chest pain, cough, hemoptysis, and dyspnea. If not diagnosed and treated promptly, the infection can disseminate hematogenously to other organs, including the brain, skin, liver, and kidneys.

Diagnosis is challenging due to the non-specific nature of symptoms and the need for early detection. It typically involves high-resolution computed tomography (CT) of the chest may reveal characteristic findings such as nodules, halo signs, or cavitations, culture of *Aspergillus* from a sterile site or histopathological evidence of tissue invasion, and detection of *Aspergillus* antigens, such as galactomannan, in serum or bronchoalveolar lavage fluid (BALF) using enzyme immunoassays or use of polymerase chain reaction (PCR) assays to detect *Aspergillus* DNA.

The mainstay of treatment for invasive *aspergillosis* is antifungal therapy. Voriconazole is considered the first-line treatment, supported by extensive clinical evidence. Alternative antifungal agents include liposomal amphotericin B, posaconazole, and isavuconazole. In some cases, surgical resection of localized sites of infection may be necessary. Managing underlying immunosuppression and reversing neutropenia, when possible, are crucial components of patient management.

The prognosis of invasive *aspergillosis* is generally poor without treatment, particularly in severely immunocompromised individuals. The overall mortality remains high, but early diagnosis and appropriate antifungal therapy can significantly improve survival rates (Machado 2024).

In conclusion, invasive *aspergillosis* is a life-threatening opportunistic infection requiring rapid diagnosis and aggressive treatment to mitigate its high mortality risk, particularly in vulnerable patient populations.

The Early Growth Response 2 transcription factor

EGR2 is part of the early growth response (EGR) family of zinc-finger transcription factors, which also includes EGR1, EGR3, and EGR4. These proteins are characterized by having multiple C2H2-type zinc finger motifs, which enable them to bind DNA and regulate gene expression. The EGR response element is a GC-rich sequence, often characterized by the presence of the hexanucleotide consensus sequence: 5'-GCG(T/G)GGGCG-3'. The target genes are involved in various cellular processes, such as growth, differentiation, and response to environmental stimuli (Beckmann and P. A. Wilce 1997).

EGR2 is critically involved in the development of the peripheral nervous system. It is required for embryonic development and the generation of hindbrain as a positive regulator of r3 and r5 rhombomeres (Giudicelli 2001) and as a repressor of the alternate r2 and r4 rhombomeres. It specifically regulates the expression of genes necessary for the proliferation and differentiation of Schwann cells, crucial for the process of myelination. During development, EGR2 is expressed in Schwann cell precursors and is essential for their maturation into myelinating cells. Mutations in the EGR2 gene can cause several neuropathies. Notably, these include Charcot-Marie-Tooth disease types 1D (DiVincenzo 2014) and Dejerine-Sottas syndrome, both of which are characterized by demyelination, muscle atrophy,

and sensory loss. Such mutations often disrupt EGR2's ability to bind DNA effectively, leading to impaired Schwann cell differentiation and defective myelination (Beckmann and P. A. Wilce 1997).

Related to the immune system, we know that EGR2 is especially important in T lymphocytes. EGR2 is expressed during the development of T cells in the thymus, where it takes part in the differentiation of developing thymocytes (Gao 2023). Moreover, EGR2 contributes to the development and function of regulatory T cells (Tregs), which are essential for maintaining immune tolerance and preventing autoimmune responses (Morita 2016). It regulates genes that are crucial for Treg identity and suppressive function. It helps regulate the activation-induced cell death and anergy in T cells, both of which are mechanisms to ensure immune tolerance.

EGR2 show expression in activated macrophages and is a marker transcription factor of AMs. Just limited number of studies touched slightly the mechanism of action and exact function of this transcription factor in these cell types.

Genome-wide techniques for study the regulation of gene expression

From the early days of understanding the role of RNA in protein synthesis, to the development of Northern blots, PCR, microarrays, and next-generation sequencing (NGS), the field of gene expression measurement has transformed dramatically. Today, we have access to a wide range of advanced technologies that enable detailed analysis of gene expression genome-wide across various contexts and at unprecedented resolutions. In this session we would like to summarize the basic concepts behind the applied methods in our studies.

Chromatin immunoprecipitation coupled with sequencing (ChIP-seq)

ChIP-seq is a powerful and commonly used technique that allows to analyze the interaction between proteins and DNA within the context of chromatin. This method is

particularly important for studying transcription factors, histone modifications, and other DNA-binding proteins that play critical roles in regulating gene expression and chromatin structure.

The main steps of this method are the followings:

- **Crosslinking**: Cells are treated with formaldehyde to crosslink DNA and associated proteins. This step preserves the protein-DNA interactions.
- **Chromatin Shearing**: The crosslinked chromatin is then fragmented into smaller pieces through sonication or enzymatic digestion, allowing access to specific regions of DNA associated with proteins.
- **Immunoprecipitation**: An antibody specific to the protein of interest is used to pull down the protein-DNA complexes from the chromatin. This step employs a method called immunoprecipitation, where the antibody binds to the target protein, and the bound DNA is captured.
- **Reversal of Crosslinking**: The crosslinks are reversed by heating, and proteins are removed, leaving behind the purified DNA that was associated with the target protein.
- **Sequencing**: The purified DNA fragments are then prepared for sequencing. This usually involves the generation of libraries followed by high-throughput sequencing, enabling the identification of the DNA regions that were bound by the protein of interest. The sequencing output consists of millions of short DNA reads that correspond to regions of the genome associated with the queried protein. Bioinformatics tools are used to align these reads to a reference genome and to analyze their distribution to identify peaks where the protein binds to (Nakato 2021).

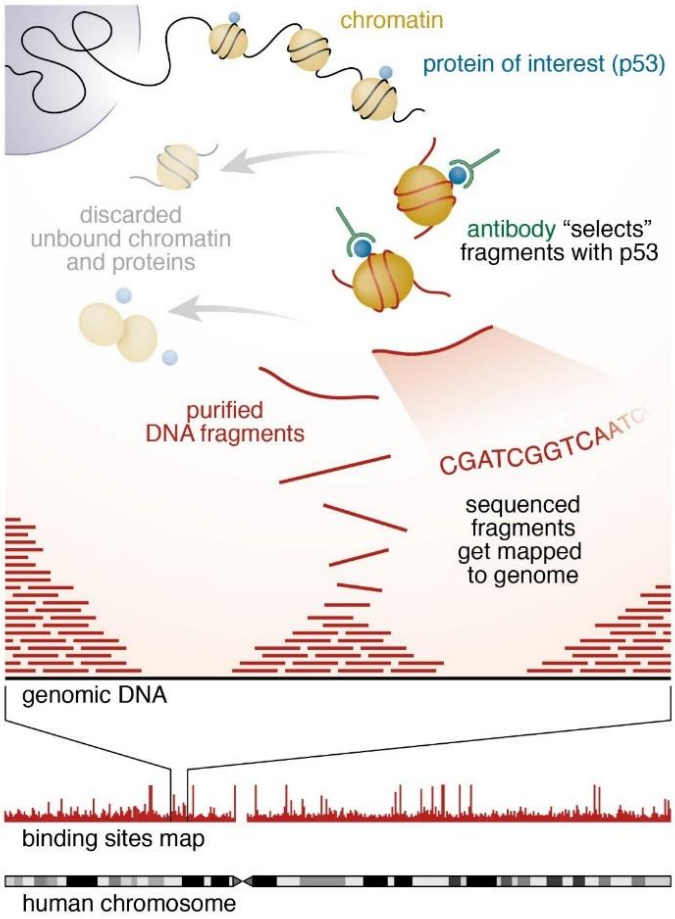

Figure 3. The basic steps of ChIP-seq (taken from: Walsh et al. 2011, https://hbctraining.github.io).

Assay for Transposase-Accessible Chromatin using sequencing (ATAC-seq)

ATAC-seq is a state-of-the-art technique in the field of genomics and epigenetics, providing detailed insights into the chromatin architecture and regulatory landscape of the genome. By revealing regions of open chromatin, it helps to understand how gene regulation is controlled and how these processes may change in various biological contexts.

ATAC sequencing leverages a hyperactive form of the Tn5 transposase enzyme, which facilitates the insertion of sequencing adapters into accessible regions of chromatin. Regions of DNA that are not tightly bound by nucleosomes are more accessible to the transposase, allowing it to integrate adapters into these regions directly. The general workflow is the following:

- **Cell Preparation**: Cells of interest are lysed, and the nuclei are isolated.
- **Transposase Treatment**: The Tn5 transposase is added to the chromatin. It cuts the accessible DNA and inserts sequencing adapters simultaneously, effectively tagging regions of accessible chromatin.
- **PCR Amplification**: The tagged DNA is then amplified using PCR to increase the amount of material available for sequencing.
- **Sequencing**: The resulting library is sequenced using NGS technology, generating millions of short reads that represent the accessible regions of the genome. The sequenced reads are aligned to a reference genome, allowing researchers to identify regions of the genome that are accessible. Peaks in the sequencing data indicate open chromatin regions, which can be further analyzed to determine potential regulatory elements associated with gene expression (Grandi 2022).

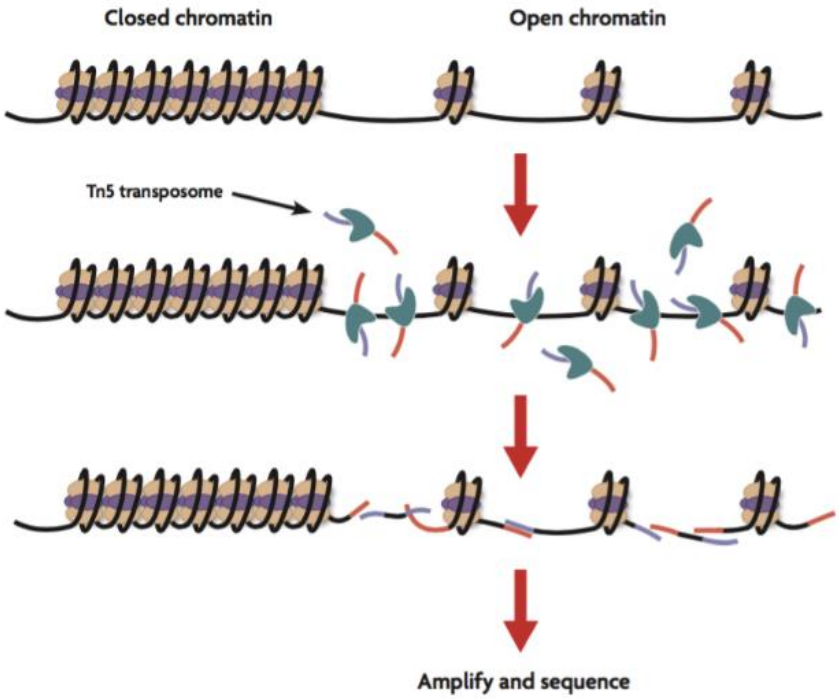

Figure 4. The theoretical background of ATAC-seq (taken from: Dillinger et al. 2021, https://www.activemotif.com/blog-atac-seq)

RNA sequencing (RNA-seq)

RNA-seq is a high-throughput sequencing technique utilized to analyze the complete transcriptome of cells, revealing insights into gene expression levels, transcript structure, and the functional complexity of RNA molecules. This approach has transformed transcriptomics by allowing researchers to obtain a genome-wide view of RNA expression and discover novel transcripts. The basic steps are the followings:

- **RNA Isolation**: Total RNA is extracted from biological samples (cells, tissues, etc.) using organic extraction methods (e.g., phenol-chloroform) or column-based purification techniques. This process isolates both coding (mRNA) and non-coding RNAs (ncRNAs), such as microRNAs, long non-coding RNAs, and ribosomal RNAs.
- **Library Preparation**:
  - **cDNA Synthesis**: mRNA is typically enriched (via poly-A selection or rRNA depletion) and converted into cDNA) using reverse transcriptase.
  - **Fragmentation and Adapter Ligation**: The cDNA is fragmented, and sequencing adapters are ligated to both ends of the cDNA fragments. These adapters contain sequences necessary for binding to the sequencing flow cell as well as indices for multiplexing samples.
- **Amplification**: The cDNA library undergoes PCR amplification to enrich for the desired fragments while adding additional sequences that facilitate sequencing.
- **Sequencing**: The prepared cDNA library is sequenced using a high-throughput NGS platform (e.g., Illumina, Ion Torrent, PacBio). This generates millions of short reads (often 50-150 base pairs) that represent the mRNA population of the original sample.
- **Data Processing**: Raw sequencing data undergo quality control (QC) assessments to filter out low-quality reads and contain adapter sequences. High-quality reads are

aligned to a reference genome or transcriptome using alignment algorithms (e.g., STAR, HISAT2). This step facilitates the mapping of reads back to their respective genomic loci. The number of reads aligned to each gene or transcript is counted, yielding a quantitative measure of gene expression. Tools like featureCounts or HTSeq can be employed for this purpose (Withanage 2022).

Cleavage Under Targets and Release Using Nuclease (CUT&RUN)

CUT&RUN is a cutting-edge technique for studying protein-DNA interactions *in vivo*, offering researchers an effective and efficient means of understanding gene regulation and chromatin dynamics. Its enhanced sensitivity and specificity compared to traditional methods position it as a valuable tool in the fields of genomics and epigenetics. CUT&RUN is based on the targeted cleavage of DNA by a specific nuclease (typically protein A fused with a cleaving enzyme, like micrococcal nuclease) in the presence of an antibody that recognizes a protein of interest. The method allows for the release of DNA fragments associated with the bound protein while minimizing the background noise from unbound DNA.

The steps of workflow:

- **Cell Preparation**: Cells are harvested and subjected to a controlled permeabilization step to allow access to the chromatin.
- **Antibody Binding**: A specific antibody against the protein of interest is added to the cells. The antibody binds to the target protein, which is associated with the chromatin region of interest.
- **Nuclease Treatment**: The complex is treated with a nuclease (e.g., micrococcal nuclease) that cleaves the DNA in the vicinity of the bound proteins, releasing the DNA fragments that are associated with the target protein.

- **Release of Cleaved DNA**: The released DNA fragments are purified. The reaction is generally carried out in such a way that only the DNA linked to the protein is isolated from the rest of the chromatin.
- **Library Preparation and Sequencing**: The purified DNA is prepared for sequencing. Typically, sequencing adapters are ligated to the ends of the DNA fragments, and the library is amplified via PCR. NGS is then used to sequence these fragments. The obtained sequence data are aligned to a reference genome to identify the binding sites of the protein. Bioinformatics tools are employed to analyze the peaks in the data, which indicate regions where the protein binds to DNA (Meers 2019).

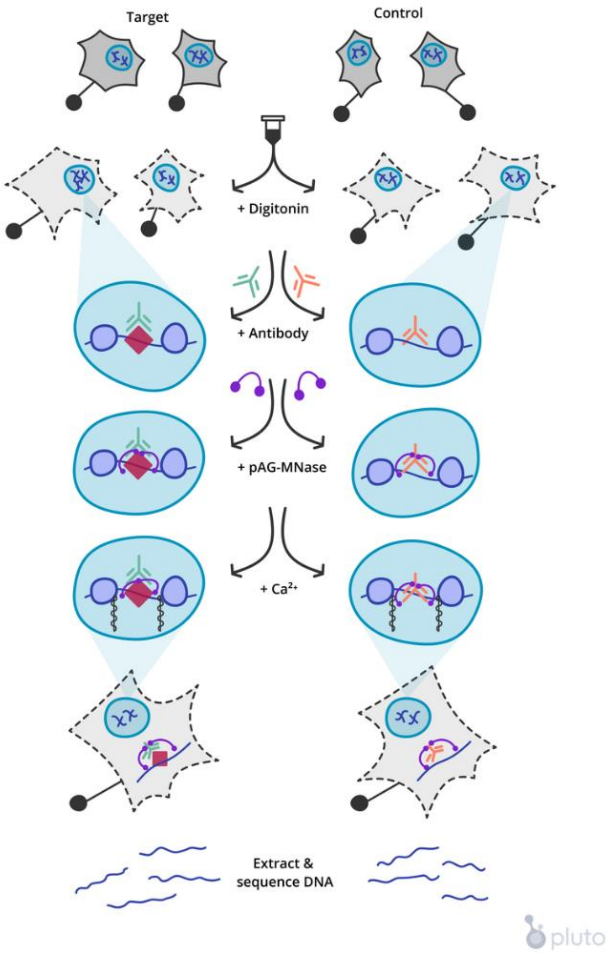

Figure 5. The schematic overview of the CUT&RUN (taken from: Brunetti 2022, https://pluto.bio/blog/getting-started-with-cut-and-run)

IV. Aims

In the first part of our study, the general aim was to identify transcriptional regulators in alternative macrophage polarization via unbiased genome-wide profiling.

1. We aimed to map the active enhancers of bone marrow-derived macrophages (BMDMs) in short term and long term IL-4-induced alterative polarization.
2. Based on the action of defined genomic regions we wanted to categorise the temporal dynamic of regulatory events.
3. We planned to find DNA binding transcriptional regulators which fulfill pivotal role in the mediation of genomic changes.
4. We aimed to examine the potential tissue specific importance of the novel found regulators.

Next, after describing EGR2 transcription factor as a candidate modulator of AM phenotype, we expanded our aims by the followings:

1. Analyze the cellular composition of lung in myeloid-specific EGR2 deficient mice.
2. Describe the EGR2-mediated epigenomic, transcriptomic and functional changes in AMs.
3. Put into *in vivo* context the EGR2 dependent alterations.
4. Examine the importance of EGR2 in pathological processes in the lung.

V. Materials and methods

Bone marrow-derived macrophage culture and treatment conditions

Isolation and differentiation of bone marrow progenitors were completed as described previously (Daniel 2014). BMDMs were differentiated by addition of L929 cells' supernatant (source of M-CSF). On day 3, the cell culture supernatant was collected, the cells were separated by centrifugation and we replaced them into the same cell culture plates and fresh media was added. On the 6^{th} day, the cells were treated with IL-4 (20 ng/ml) for 1 hour or 24 hours.

Chromatin immunoprecipitation

The experiment was performed as previously described with minor modifications (Daniel 2014). Ovation Ultralow Library Systems V2 (Nugen) was applied for library preparation following the manufacturer's instructions. The used antibodies: P300 (sc-585), and H3K27ac (ab4729).

Analysis of ChIP-seq

Reads were mapped to the mouse reference genome (mm10) using BWA MEM aligner (https://arxiv.org/abs/1303.3997). Low mapping quality reads (MAPQ<10), reads mapping to Encyclopedia of DNA Elements (ENCODE) mouse blacklisted regions and duplicated reads were discarded from the downstream analyses by samtools rmdup and bedtools intersectBed. Coverage profiles were calculated by deeptools2 bamCoverage. Putative binding sites were described by MACS2 (5% false discovery rate (FDR). ChIP-seq read density profiles for region set summits were calculated using deeptools2 computeMatrix and plotHeatmap functions.

P300 differential binding analysis

To determine differentially bound genomic regions (FDR 5%, fold change > 1.5), we used the limma-voom model, through the DEApp shiny API.

De novo motif enrichment analysis and motif mapping

De novo motif enrichment analysis was performed by HOMER's findMotifsGenome on the summit 200 bp regions of identified peaks. 10, 12, 14, and 16 bp were the targeted motif lengths. P-values were generated by HOMER by comparing the target regions and random set of regions (background). For motif distribution plots, matrices of the enriched motifs were mapped following the order of regions in the tag density heat maps by using the -mbed parameter of HOMER's annotatePeaks in 20 bp windows within 2 kbp frames relative to the peak centers. The top motif score for the different sets of ATAC-seq regions was determined by using the -mscore parameter of HOMER's annotatePeaks.

Mouse strains

The experimental animals were bred at the Laboratory Animal Core Facility of the University of Debrecen under specific pathogen-free (SPF) conditions. The genetic background of applied mouse strains was C57BL/6. The *Egr2*$^{fl/fl}$ mouse strain was a kind gift from Patrick Charnays's laboratory. We crossed the lysozyme Cre (LysCre) mice with *Egr2*$^{fl/fl}$ strain to reach the myeloid cell specific knock out (KO) condition (referred to *Egr2*$^{fl/fl}$). These mice were crossed back with C57BL/6J strain for eight generations. We used *Egr2*$^{+/+}$ LysCre littermates (referred to *Egr2*$^{+/+}$) as control animals. We applied 3-month-old female and male mice for experiments.

Real-time quantitative polymerase chain reaction for enhancer RNA and messenger RNA detection

We isolated total RNA of cells by TRIZOL (Invitrogen) reagent following the manufacturer's instruction. High-Capacity cDNA Reverse Transcription Kit (Applied Biosystems) was applied for reverse transcription according to the suggested steps from manufacturer. The eRNA and mRNA transcript detection was run by SYBR Green (BioRad) intercalation. We calculated the expression values applyin the delta Ct method. The raw expression values were normalized to *Ppia* expression.

EGR2-expressing embryonic stem cell-derived myeloid progenitor cell generation

The EGR2-expressing doxycycline-inducible murine embryonic stem cells (ESCs) were cultured in Dulbecco's Modified Eagle Medium (DMEM) (Thermo-Fischer Scientific) complemented with 15% Fetal Bovine Serum (FBS) (Thermo-Fischer Scientific), 1000 U/ml Leukemia Inhibitory Factor (LIF) (Merck), streptomycin (50 μg/ml), and penicillin (100 U/ml) (Merck) in the presence of 200 μg/ml G418.

The embryoid bodies (EBs) were created with minor changes as previously described (Boto 2021). ESCs were cultured in Iscove′s Modified Dulbecco′s Medium (Thermo-Fisher Scientific) containing 15% FBS, iron-saturated transferrin (200 ng/ml, Sigma), 4.5 mM monothioglycerol (Sigma) and ascorbic acid (50 ng/ml, Sigma). Petri dishes were kept under slow rotation for 6 days. EBs were harvested with trypsin-EDTA treatment. The dissociated cells were cultured for 3 further days in alpha-Minimum Essential Medium (alpha-MEM) supplemented with 20% FBS, GM-CSF (50 ng/ml, PeproTech, London, UK), and 50 μM β-mercaptoethanol (Merck) in monolayers. The induction of EGR2 was initialized by the addition of 1 μg/ml of doxycycline. Finally, the cells for experiments were harvested with the solution of trypsin/EDTA.

ATAC-seq

25000 cells served as template for ATAC-seq. The nuclei of AMs were isolated by ATAC-LB (10mM Tris-HCl pH7.4, 10mM NaCl, 3mM MgCl2, 0.1% IGEPAL). The isolated nuclei were used for tagmentation by Nextera DNA Library Preparation Kit (Illumina). We purified the DNA applying the MinElute PCR Purification Kit (Qiagen). We amplified the tagmented DNA by Kapa Hifi Hot Start Kit (Kapa Biosystems). The libraries were purified using again the MinElute PCR Purification Kit (Qiagen). We analyzed the quality of fragment distribution of libraries with Agilent Bioanalyzer. The sequencing was performed by HiSeq 2500 platform.

Analysis of ATAC-seq

Raw sequence reads were aligned to the mm10 reference genome assembly with default parameters by using the BWA tool v07.17 and BAM files were generated with SAMtools v1.7. Peaks were predicted with the callpeak function of MACS2 and their widths were fixed to 200 bp relative to their summits. Artifacts were removed according to the blacklisted genomic regions of ENCODE. Genome coverage (bedgraph) files were generated by HOMER's makeUCSCfile. Differentially accessible chromatin regions between the WT and EGR2 KO AM-derived samples were defined by DiffBind in R v3.5.1. Peaks that could be predicted from at least two samples were used for the comparison in which a $p \leq 0.05$ cut-off was applied. Read distribution (tag density) heat maps of the different peak sets were carried out by HOMER's annotatePeaks in 10 bp windows within 2 kbp frames relative to the peak summits. The separation of the promoter (promoter-TSS and 5' UTR) and enhancer (introns, intergenic, exons, 3' UTR, and TTS) regions was based on the HOMER's annotatePeaks. Genomic distribution of the peaks was also determined by HOMER's annotatePeaks, where promoter-

TSS covers both promoter-transcription start site (TSS -1000 bp/+100 bp) and 5′ untranslated regions (UTRs), and intergenic includes both intergenic and non-coding regions.

RNA-seq

The cells total RNA content was isolated by TRIZOL (Invitrogen) reagent according to the manufacturer's instructions. We performed quality check of total RNA samples by Eukaryotic Total RNA Nano Kit following the protocol of manufacturer and applying Agilent BioAnalyzer. Samples with >7 RNA integrity number were processed for library preparation by Ultra II RNA Sample Preparation Kit (New England BioLabs). Poly-T oligonucleotid attached magnetic beads were use for poly-A tailed RNA selection. Then, the samples were eluted and fragmented (94°C). We generated cDNA by random priming reverse transcription. After end repair, single adenine base addition and barcode-adaptor ligation steps the libraries were generated by adapter-specific PCRs. The samples were sequenced on Illumina NextSeq 500 instrument with single-end 75-cycle sequencing.

Analysis of RNA-seq

Raw sequence reads were aligned to the mm10 reference genome with HISAT2 v2.1.0 using default parameters and from the BAM files, transcripts were assembled with StringTie v1.3.4d. Bam files were indexed with SAMtools v1.7, then coverage (bedgraph) files were generated by HOMER's makeUCSCfile program. We defined the expression levels in Fragments Per Kilobase of transcript per Million (FPKM) values.

The multi-dimensional scaling (MDS) plot was generated by the plotMDS function of the limma package in R. The Kyoto Encyclopedia of Genes and Genomes (KEGG) biological pathways were predicted with the -go options of HOMER's annotatePeaks package. K-means

clustering of the gene sets was carried out by Cluster 3.0, and the applied similarity metric was the centered correlation.

RNA-seq and ATAC-seq data integration

The assignment of the DARs to the DEGs was based on the linear proximity from the TSSs: gene TSSs were extended to ±100 kbp or to the nearest gene(s) and the changing ATAC-seq peaks overlapped with these extended regions were considered as potential regulatory regions. Overlaps were done with intersectBed commands of BEDtools v2.27.1. For the distance distribution of the repressed ATAC-seq peaks relative to the repressed genes, the presence of the neighboring genes was not taken into account, only the distance itself (11 bins were defined from <100 to >1000 kbp).

CUT&RUN

80000 AMs were aliquoted per sample. The CUT&RUN was performed by the CUTANA ChIC/CUT&RUN Kit (EpiCypher) according to the manufacturer's instructions. The DNA was purified by the CUTANA DNA Purification Kit. Sample concentration was measured applying the Qubit fluorometer. For library preparation 1 ng of DNA was used and performed by the NEBNext Ultra II DNA Library Prep Kit (New England Biolabs) following to the manufacturer's guideline. Libraries were assessed by the Agilent Bioanalyzer. Illumina NextSeq 500 was used for sequencing with a Mid Output Kit (150 cycles).

Analysis of CUT&RUN

Raw sequence reads were analyzed with default parameters by using the nfcore/cutandrun pipeline v1.1. The reads were aligned to the mm10 reference and spike-in (Escherichia_coli_K_12_MG1655) genome with Bowtie2 v2.4.2. The adapter and quality trimming were performed with Trim Galore! v0.6.6. Bam files were indexed with SAMtools

v1.13, then the duplicated reads were marked by using the MarkDuplicates tool of Picard v2.25.7. Peaks were predicted with the callpeak function of MACS2. Genome coverage (bedgraph) files were generated by HOMER's makeUCSCfile. The H3K4me3 signal was measured as Reads Per Kilobase of transcript, per Million mapped reads (RPKM) value on the downstream 500 bp regions of gene TSSs by using the coverageBed command of BEDtools.

Bronchoalveolar lavage (BAL) for alveolar macrophage isolation

First, mice were put into a glass container and euthanized by isoflurane (Forane, Baxter) inhalation. After gentle anatomical preparation of the trachea and lung, we inserted a 20 G diameter endotracheal cannula (Kent Scientific) to the trachea and we washed out the bronchoalveolar space three times with 800 µl of Phosphate Buffered Saline (PBS) solution supplemented with 200 mM Ethylenediaminetetraacetic Acid (EDTA, pH: 7.4) and 1% FBS. The isolated BALF was centrifuged at 4°C (10 minutes, 800 g) to separate the cellular components. Then we removed the supernatant, and we resuspended the cells in 200 µl of Ammonium-Chloride-Potassium (ACK) lysis buffer for 2 minutes at room temperature to lyse contaminating blood cells. To pellet cells, we centrifuged them with the same settings.

Generation of single cell suspension from total lung for flow cytometric analysis

The experimental animals were euthanized by application of isoflurane inhalation. After perfusion of lung vessels through the cardiac right ventricle with PBS solution, the lungs were removed and cut into small pieces on ice. After this step, a Lung Dissociation Kit (Miltenyi Biotec) was applied for further preparation following to the manufacturer's guideline.

Flow cytometry and cell sorting

The cells were incubated with Fc Receptor Blocking Reagent (Miltenyi Biotec) in 1:100 dilution (10 minutes, 4 °C), then they were stained by antiody mix (0.04 μg/μl, 25 minutes, 4 °C in dark). In intracellular stainings the AMs were fixed and permeabilized by the Forkhead box P3 (FoxP3)/Transcription Factor Staining Kit's (eBioscienceTM) 1×Fixation/Permeabilization reagent (overnight, 4 °C). The cells were washed with 1×Permeabilization/Wash buffer. Intracellular staining was performed in 100 μL 1×Permeabilization/Wash buffer containing the intracellular antibody mix (1 hour, 4 °C). Cells were washed again with Permeabilization buffer and resuspended in MACS buffer. The flow cytometry analysis and sorting were performed with Cytek Aurora and FACS Aria III (BD Biosciences) spectral flow cytometers.

The used antibodies: anti-CD45.2 (BV421 Mouse Anti-Mouse CD45.2 Clone 104, BD Biosciences and BV750 Clone 30-F11, Biolegend), anti-CD11b (PE-Cy™7 Rat Anti-CD11b Clone M1/70, BD Biosciences and PE-Texas Red Clone M1/70.15, Invitrogen), anti-CD11c (PE Hamster Anti-Mouse CD11c Clone HL3, BD Biosciences and APC-R700 Clone N418, BD Biosciences), anti-F4/80 (APC Rat Anti-Mouse F4/80 Clone T45-2342, BD Biosciences and Pacific Blue Clone BM8, Biolegend), anti-SiglecF (APC-Cy™7 Rat Anti-Mouse Siglec-F Clone E50-2440, BD Biosciences), anti-CLEC7a (BD OptiBuild™ BV711 Rat Anti-Mouse CD369 (Clec7a) Clone 218820, BD Bioscience), anti-Ly6G (PerCP-Cy™5.5 Rat Anti-Mouse Ly-6G Clone 1A8, BD Bioscience and BV510 Clone 1A8, BD Biosciences), anti-CD4 (BUV395 Clone GK1.5, BD Biosciences), anti-CD8 (BUV737, Clone 53-6.7, BD Biosciences), anti-Ly6C (BV605 Clone HK1.4, Biolegend), anti-CD25 (BV650, Clone PC61, BD Biosciences), anti-CD24 (BV711 Clone M1/69, BD Biosciences), anti-CD140a (BV785 Clone APA5, BD Biosciences), anti-CD103 (AF488/FITC Clone 2E7, Invitrogen), anti-CD31 (BB700 Clone MEC 13.3, BD Biosciences), anti-CD64 (PerCP-eFluor 710 Clone X54-5/7.1,

Invitrogen), anti-TCR-γδ (APC Clone GL3, Biolegend), anti-MHCII (APC-Cy7 Clone M5/114.15.2, Biolegend), NK1.1 (APC/Fire 810 Clone S17016D, Biolegend), Foxp3 (PE Clone FJK-16s, Invitrogen), anti-CD3 (PE-Cy5 Clone 17A2, Biolegend), anti-CD45R-B220 (PE/Fire 700 Clone RA3-6B2, Biolegend), and anti-CD326 (PE-Cy7 Clone G8.8, Biolegend). FlowJo v.10 software was applyed for data visualization.

Visualization

Row-normalized gene expression heatmaps were visualized in R by pheatmap package. Read distribution (tag density) and non-normalized heatmaps were visualized by Java TreeView v1.1.6r4. Histograms, pie- and (stacked) bar charts, box-, violin-, line-, scatter- and volcano plots were plotted by using GraphPad Prism v.9. The area-proportional Venn diagram was generated by Intervene. Genome coverage (bedgraph) files were visualized by Integrative Genomic Viewer (IGV) v2.4.16 where the replicates that belong together were overlaid on each other (overlay tracks). Proportional dot plots were visualized by ggplot by using the tidyverse, and ggthemr packages in R.

Phagocytosis assays

The cells were isolated by BAL as previously described from the lungs of *Egr2*$^{+/+}$ and *Egr2*$^{fl/fl}$ mice and CD45^{+} AMs were purified applying magnetic bead selection (Miltenyi Biotec). We created a cell culture by plating 100.000 cells at 6-well dishes in 1 mL RPMI medium supplemented with 10% FBS, and 5%-5% of penicillin and streptomycin. When the cells were attached, we applied 1x10^{6} pHrodo-Red labeled zymosan, *E. coli*, *S. aureus* or dextrane bioparticles (Invitrogen) per one well. Upon 20-, 60-, 120- or 180 minutes incubation period we scraped up the attached AMs and measured them by FACS Aria III flow cytometer (BD Biosciences).

Confocal microscopy

For confocal microscopy, we plated 50000 AMs into 8-well chambered coverslips (Ibidi) and we kept the in 300 µl of RPMI medium supplemented with 5% streptomycin, 5% penicillin, and 10% FBS until the attachment of cells. We added $2x10^6$ Texas-Red labeled zymosan bioparticles (Invitrogen™, Z2843) per one well. After incubation we washed the cells with PBS solution and recorded the confocal images by Zeiss LSM 880 microscope (Carl Zeiss, Jena, Germany) using 40× magnitude (1,2 numeric aperture (NA), C-Apochromat water immersion objective. Texas Red fluorescence images and transmitted light images were recorded by using a 543 nm HeNe laser; fluorescence emission was detected between 540-642 nm. The images were analyzed using the FIJI distribution of ImageJ v2.0.0-rc-69/1.52i and the particles within cells were counted manually.

Cytokine Array

Quantibody® Mouse Cytokine Array 1000 Kit (QAM-CAA-1000) was applied for the analysis of cytokine concentrations and the experiment was performed by RayBiotech company. Hierarchical clustering of log-scaled protein amount (µg/ml) values was carried out by Cluster 3.0 and the non-scaled heatmap was visualized by JavaTreeView. The applied similarity metric was Euclidean distance, and the clustering method was by single linkage.

Fungal strains

AF 293 *Aspergillus fumigatus* strain was applied for all mentioned experiments. It was cultured on a standard nitrate minimal medium at 37°C. To harvest conidia for experiments, the fungi were grown for 6 days and were concentrated in PBS solution supplemented with 0.1% Tween 80.

Zymosan-induced *in vivo* lung inflammation model

Egr2$^{+/+}$ and *Egr2*$^{fl/fl}$ animals were anesthetized by the inhalation of isoflurane. 300 μg zymosan bioparticles (Invitrogen) were intranasally administered in 40 μl final volume. Finally, the mice were euthanized upon 6 hours or 24 hours incubation time. We harvested the lungs for further experiments, or we isolated the bronchoalveolar cellular components by BAL and we performed flow cytometric analysis and cell sorting.

Ex vivo zymosan treatment of alveolar macrophages

The cells were isolated by BAL as previously described from the lungs of *Egr2*$^{+/+}$ and *Egr2*$^{fl/fl}$ mice and CD45^{+} AMs were purified applying magnetic bead selection (Miltenyi Biotec). We created a cell culture by plating the cells at 24-well dishes in 0.5 mL RPMI medium supplemented with 10% FBS, and 5%-5% of penicillin and streptomycin. When the cells were attached, we applied zymosan bioparticles (unlabeled, Invitrogen) in 50 μg/ml concentration. Upon 6- and 24 hours incubation period we isolated the total RNA by TRIZOL (Invitrogen) for eRNA and mRNA measurements.

Aspergillus fumigatus – alveolar macrophage *ex vivo* co-treatment model

The AMs were isolated and purified by CD45 magnetic bead selection (Miltenyi Biotec). The cells (10^5 AMs per well) were cultured in RPMI medium containing 5% penicillin, 5% streptomycin and 10% FBS. After the attachment of cells, we treated them with *AF* conidia (10^6/well). We replaced the medium upon 1-hour and we incubated the cells for 6 hours. After scratching the AMs we prepared decimal dilution series. We inoculated the samples in nitrate minimal media agar slants at 37°C and after 48 hours we counted the colony forming units (CFUs).

Time-lapse microscopy

The isolation of AMs, the culture and treatment conditions were the same than in CFU assay. After washing out the *AF* conidia, in every 5 second time-lapse images were snaped by Olympus upright microscope (Tokyo, Japan) using 10x magnutude, 0.25 NA plan achromatic objectives (Carl Zeiss, Jena, Germany), and 2-megapixel UVC USB 2.0 camera boards (Asus Computer International, Fremont, CA, USA). We counted manually the hyphas in the cells and the time-point of hypha breakout. The representative images were analyzed applying the ImageJ v1.39d software.

Aspergillus fumigatus in vivo infection model

Mice were housed in plastic cages (425/135/120 mm, 573.75 cm2) in groups of 5-6 with mesh covers according to 2010/63/EU guidelines. Animals were fed with pelleted mouse chow (Purina) and tap water *ad libitum*. Automated room illumination of 12 hours light and 12 hours dark, and room temperature (22–25 °C) was maintained. As the immunosuppression, we administered CP (250 mg/kg) i.p. The first treatment was 3 days prior infection and we repeated it on day 1 post infection. On the same days, we applyied gentamicin prophylaxis (5-mg/kg body weight). We instillated $3.5x10^6$ *AF* conidia in 50 μl per mouse. After infection, we followed for 11 days the symptoms and body weight.

Histological analysis

Before lung harvesting, we perfused the vessels through the cardiac right ventricle with 10 mL of PBS solution. The isolated organs were fixed in 4% buffered paraformaldehyde (PFA, pH7.4) then embedded in paraffin. The sections were created followed by deparaffinization, and rehydration visualized by haematoxylin and eosin (H&E), Masson's trichrome, Periodic acid–Schiff (PAS) and Grocott staining using standard methods. The

myeloperoxydase (MPO) immunohistochemistry was carried out applying rabbit monoclonal primary antibodies with Envision (biotin-free) Peroxidase-based Detection Kit (Dako) and DAB substrate chromogen (Vector Labs), according to the vendor's protocol. The stained sections were scanned by Panoramic MIDI digital slide scanner (3D-Histech-Zeiss, Budapest, Hungary) combined with a Charge-coupled Device (CCD) camera (Hitachi, HV-F22CL). The further analysis of digitalized sections were performed by Mirax Viewer v.1.6.2.4.

Determination of lipid mediators by Targeted Liquid Chromatography with tandem Mass Spectrometry (LC-MS/MS)

The total lungs samples were snap frozen in liquid nitrogen. After we put the sampels to ice-cold methanol containing deuterated internal standards (d_4-LTB_4, d_4-PGE_2, d_5-LXA_4, d_5-Maresin1 (MAR1), d_5-Resolvin D2 (d_5-RVD2), and d_8-5-hydroxyeicosatetraenoic acid (d_8-5-HETE), Cayman Chemical, Ann Arbor, MI). The lungs were minced and placed to -80°C for 1 hour. After centrifugation (13,000 rpm; 10 min; 4°C), the supernatants were separated and the protein pellets were lysed by RIPA lysis buffer (Thermo). The total protein content was determined using bicinchoninic acid (BCA) assay (Thermo). Supernatants were went out solid-phase extraction (SPE) using C18 columns (Biotage, preconditioned with washes of methanol and water). Prior to SPE extraction, the samples were diluted with water acidified (pH approximatly 3.5). The samples were washed with hexane, then lipid mediators were eluted by methyl formate. The solvent was evaporated under a stream of N_2 gas and samples were resuspended in methanol:water (50:50, v/v). Samples were measured applying a high-performance liquid chromatography system (HPLC; Shimadzu, Kyoto, Japan) equipped with refrigerated autosampler and a Poroshell reverse-phase C18 column (100 mm x 4.6 mm x 2.7mm; Agilent Technologies) that was held at 50°C. A gradient method was used that started with methanol/water/acetic acid (50:50:0.01 v/v/v) and was ramped to 98:2:0.01 using a

constant flow rate of 0.5ml/min. A Qtrap5500 mass spectrometer (AB Sciex, Framingham, MA) was coupled to the HPLC and was operated in negative ionization mode. Data acquisition was accomplished using Analyst software v.1.7. A scheduled multiple reaction monitoring (MRM) method was used to identify lipid mediators based on specific parent ion/daughter ion pairs that were established using synthetic standards for each individual lipid mediator (Cayman Chemical, Ann Arbor, MI). Identification of lipid mediators in the samples was accomplished using Sciex OS-Q v.1.7 by comparing the retention time of mediators in the samples to authentic standards run in parallel, using diagnostic MRM transitions. In selected samples, we also assessed full MS/MS spectra that were acquired utilizing information-dependent enhanced product ion mode scanning.

Lipid mediators were quantified by integrating peak areas above the baseline and interpolation based on external standard curves for each individual mediator, followed by accounting for extraction recovery based on internal deuterated standards with similar chromatographic retention times. Levels of lipid mediators were then normalized to the protein content of the tissue taken for extraction. The lower limit of quantification was established for each mediator and was defined as the lowest amount that could be quantified in replicate injections with a coefficient of variation (CV) of less than 20%.

Analysis of bronchoalveolar lavage fluid protein contents

The protein level of BALF was measured by BCA assay (Thermo Fisher Scientific, A55860). We determined lactate dehydrogenase (LDH) activity by applying LDH Activity Assay Kit (Sigma-Aldrich, cat.no. MAK066). The cytokine levels were detected using TNFα, IL-6 (Biolegend), CXCL9 (cat.no. #EMCXCL9), CXCL11 (cat.no. #EMCXCL9), and CXCL13 (cat.no. #EMCXCL13) enzyme-linked immunosorbent assay (ELISA) Kits (Invitrogen) following the instructions of manufacturers.

Seahorse analysis of extracellular acidification rate (ECAR) and oxygen consumption rate (OCR)

We compared 110.000 BAL-isolated AMs from *Egr2*$^{+/+}$ and *Egr2*$^{fl/fl}$ mice. XF96 oximeter (Seahorse Biosciences, North Billerica, MA, USA) wa sapply for the measurement of OCR and ECAR values. AMs were seeded in a 96-well plates (specific for Seahorse assay) one day prior to the experiment. 1 hour prior to the assay, the cell culture medium was replaced with unbuffered medium and we put the cells into a CO2-free incubator (evaporation of remaining CO2). The values were recorded after 5 minutes of 30 sec mixing cycle and we repeted these steps 5 times. The baseline OCR and ECAR values were record without treatment. Then, we applied inhibitors in the following concentrations: 50 μM of Etomoxir, 2 μM of Oligomycin and 10 μM of Antimycin A. 5-cycle measurement round was used. We terminated the assay by the lysis of cells with 1M NaOH. The recorded data were normalized to total protein contents determined by BCA Kit (Thermo Fisher Scientific, A55860).

Western Blot

BMDMs and *Egr2*$^{+/+}$ and *Egr2*$^{fl/fl}$ AMs were the templates of measurements. We generated whole cell lysates applying RIPA lysis buffer. The prepared lysates were resolved in a 4-16% gradient Bis-Tris polyacrylamide gel by electrophoresis and transferred to immobilon-P transfer membrane. The membrane was incubated for 5 minutes with REVERT Total Protein Stain before imaging total protein loading. We blocked the membranes for 1 hour at room temperature then we probed them with 1:1000 anti-EGR2 antibody (Abcam, ab108399) overnight (4 °C). We was washed the membranes with Tween-Tris-buffered saline (TTBS) solution 5 times for 5 minutes and added 1:20000 of anti-Rabbit IgG (R&D Systems, HAF008) as secondary antibody for 1 hour at room temperature. After wash with 0.1% TTBS as same as

previously the membranes were incubated with SuperSignal West Pico PLUS Chemiluminescent Substrate for 5 minutes.

Data and software availability

The performed and referred next-generation sequencing data are available in the National Center for Biotechnology Information (NCBI) Gene Expression Omnibus (GEO) repository under GSE151015 and GSE181087.

Statistics

The differentially expressed genes (DEGs, RNA-seq experiment) were described applying one-way analysis of variance (ANOVA) test supplemented with a post-hoc Tukey honestly significant differences test (R: stats, tidyverse, and sqldf packages). Considering all samples, the genes that showed higher expression value than 1 FPKM at least in two independent samples, were considered as expressed and were included in the comparative analyzes, in which $p \leq 0.05$ cut-off threshold was used. We applied one-way ANOVA test with Tukey post hoc test to determine the significance of proteins measured by ELISA cytokine array. In all other experiments Student's t test was applied. Significant differences between groups were considered if p-value was ≤ 0.05 (Indicated by asterisks: *$p \leq 0.05$, **$p \leq 0.01$, ***$p \leq 0.001$, ****$p \leq 0.0001$).

VI. Results

The genome activity patterns of short- and long-term alternative macrophage polarization

To identify the genomic events of alternative macrophage polarization we applied IL-4 treated murine BMDM polarization model. We analyzed the temporal changes of cistrome and transcriptome by unbiased datasets. We used unstimulated BMDMs as control and we detected the short-term polarization after 1 hour and the long-term polarization upon 24 hours IL-4 cytokine treatment. To map active enhancers, we designed a ChIP-seq-based approach. We determined the genomic binging sites of P300, a transcriptional co-activator, and the level of active histone mark H3K27ac. The combined occupancy of these signs represents the active enhancers (Creyghton 2010) that we used as a pool of further analysis.

As a first action to get insight to the epigenomic events, we defined genomic regions with differential levels of P300 and H3K27ac. Based on these sequences, we performed *de novo* motif enrichment analysis applying HOMER. We identified nearly similar amount of activated (n=16735) and repressed (n=17582) regulatory elements during alternative BMDM polarization. 14353 genomic sites were unchanged. We clustered the regulatory elements based on activity pattern. We separated them to “early transient” and “sustained” and “late” categories. We selected a region as “early transient” if it was activated or repressed upon 1 hour IL-4 treatment and lost activity or relieved of repression by 24 hours. We added the regions to “early sustained” group when they were activated or repressed at 1 hour and retained their activity or repression at 24 hours. The “late” category containes only the regions that became activated or repressed at 24 hours after IL-4 treatment (Figure 6).

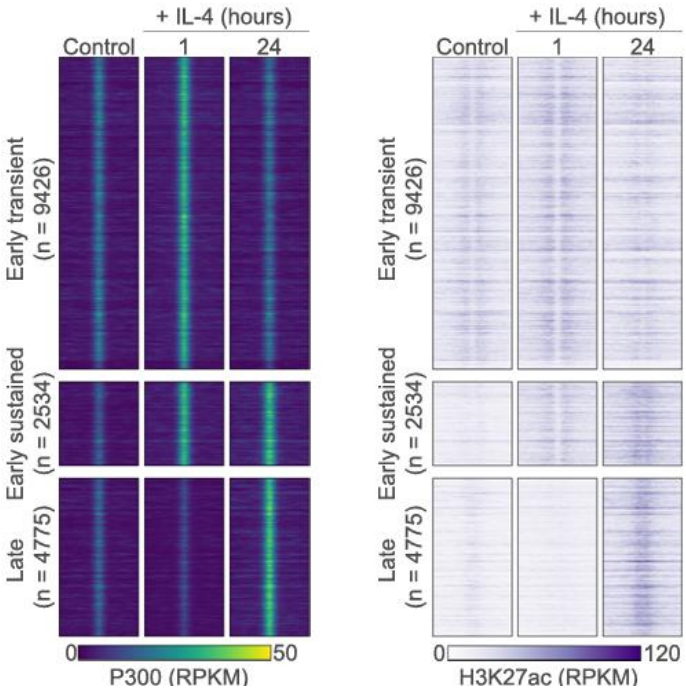

Figure 6. The temporal dynamic of genome activity during alternative macrophage polarization. Read distribution plot of P300 binding (dark blue) and H3K27ac signal (light blue) in the three activity categories (late n=4775, early sustained n=2534 and early transient n=9426) showing distinct pattern in control and IL-4 (20 ng/ml) polarized BMDMs for the indicated time periods (RPKM). P300 summits are in the middle of the visualized regions.

These experiments described the alternative macrophage polarization induced temporal dynamics of the cistromic changes in BMDMs and open the possibility to identify the dominant driver transcriptional regulators which mediates these epigenomic alterations.

The EGR2 is a late-stage regulator of alternative macrophage polarization

To find potential transcription factors mediating different genome activity patterns during alternative macrophage polarization, we run motif enrichment analysis based on the sequences of changing genomic regions. The found motifs are associated with known macrophage-specific transcription factor binding sites (e.g. PU-1, AP-1, Interferon Regulatory Factor (IRF), Runt-related transcription factor (RUNX), and C/EBP) in all genome activity category (Horvath 2019). We confirmed the enrichment of STAT6 binding motif using

the defined genomic regions of early activation (both transient and sustained ones) as we expected based on that STAT6 is a known initiator of this process. In addition to STAT6, we found the enrichment of other novel transcription factor motifs which show high specificity to sustained genomic activity. Among these factors the EGR was enriched in both early sustained and late categories, indicating the potential significance of EGR transcription factor family in the regulation and maintenance of alternative macrophage polarization (Figure 7).

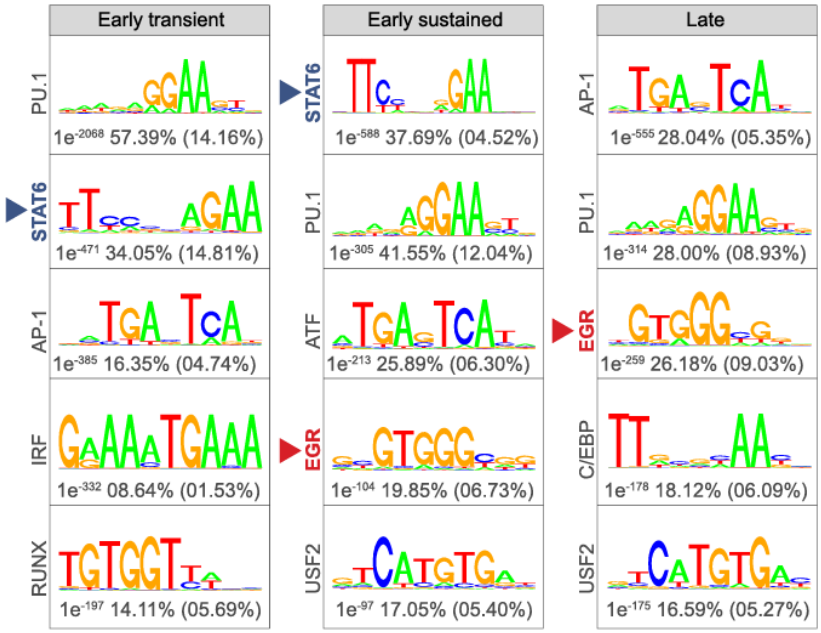

Figure 7. Regulatory elements with distinct genome activity link the EGR motifs to IL-4 mediated alternative polarization. The figure shows the enriched motifs logo and their significance values under "early transient", "early sustained" and "late" dynamic genomic regions defined by P300 bound regions in IL-4 (20 ng/ml) polarized BMDMs.

To determine which member of the EGR family affects the genomic activity of alternative macrophage polarization, we analysied the mRNA level of all members of EGRs in unstimulated an IL-4 treated BMDMs in different time points applying RNA-seq datasets. We also checked the mRNA level of *Stat6* and the known M2 markers (*Retnla, Chil3, Arg1*) as controls. Near the presence of *Stat6* and induction of M2 markers, just the *Egr2*'s mRNA was detectable among the EGR members and this gene showed elevation during alternative

macrophage polarization. We measured the protein level of EGR2 which followed the same expressional tendency in the samples (Figure 8).

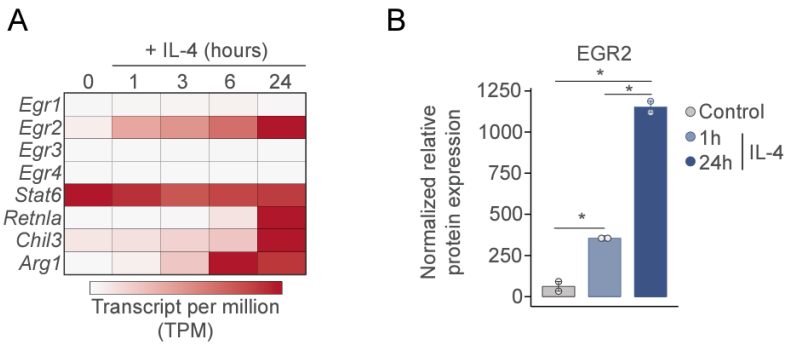

Figure 8. EGR2 is presence in BMDMs from EGR family members and induced upon IL-4 stimulus. (A) Heatmap representation of EGR family members, *Stat6* and macrophage activation marker genes (*Retnla*, *Chil3*, *Arg1*) expression based on RNA-seq in indicated time-points. **(B)** The relative expression of EGR2 protein level in BMDMs during IL-4 treatment quantified based on Western Blot by densitometry (mean±SEM, n=2).

We hypothetised that the EGR2 is the modulator of alternative macrophage polarization from EGR family based on these gene expressional results.

Next, we created a EGR2 knock-out (KO) mouse model, specific for myeloid cells to examine the role of this transcription factor in alternative polarization. We reached this phenomenon using the cross of Lysozyme-Cre (LysCre) mouse line and *Egr2*$^{fl/fl}$ mouse line on the C57BL6 genetic background (referred here as *Egr2*$^{+/+}$ for the wild-type (WT), control and *Egr2*$^{fl/fl}$ as the KO genotype). The applied modification results in total loss of EGR2 protein in control and IL-4 treated BMDMs (Figure 9).

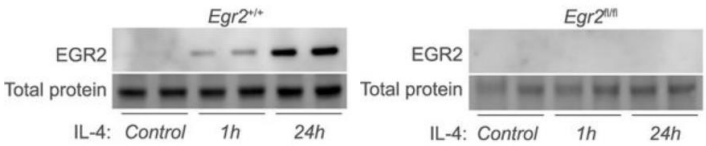

Figure 9. EGR2 is presence in BMDMs from EGR family members and induced upon IL-4 stimulus. Western blot analysis of EGR2 in control, 1 hour and 24 hours IL-4 treated BMDMs and total protein imput of samples (representative images).

We generated BMDMs from control and *Egr*$^{fl/fl}$ mice and we treated them with IL-4 in different time point between 0 and 24 hours. Then we measured the expression of alterative polarization marker genes' (*Retnla, Ccl17, Chil3, Chil4, Arg1 and Mrc1*) mRNA level by RT-qPCR (Figure 10).

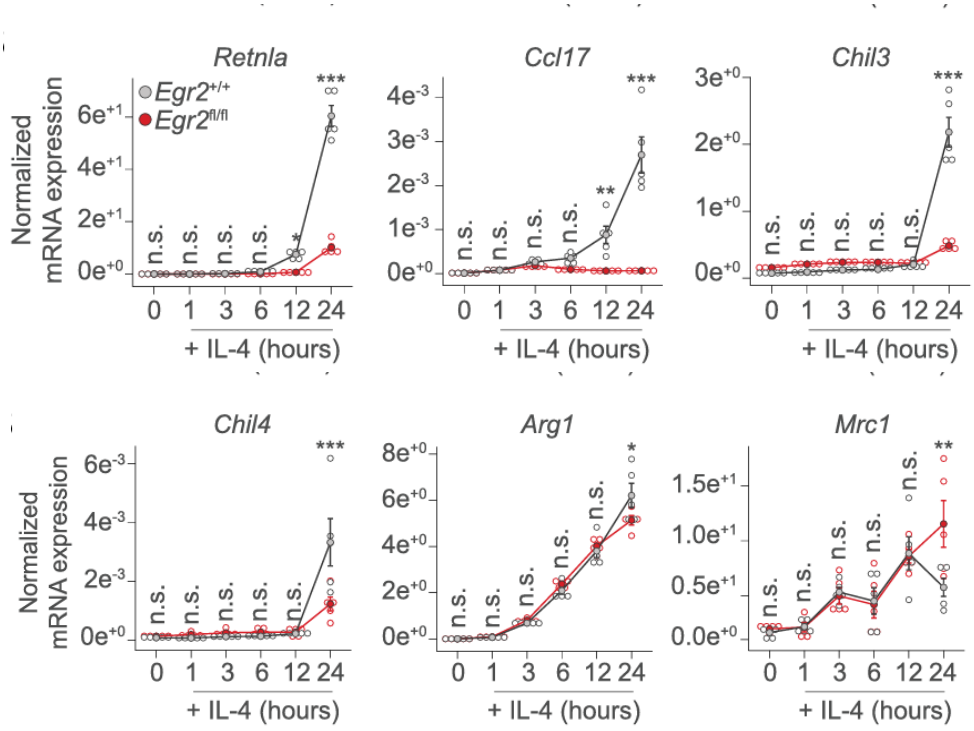

Figure 10. M2 marker genes show EGR2-dependent expression at late-stage of IL-4 treatment. The graphs indicate the relative mRNA expression values of indicated genes (*Retnla, Ccl17, Chil3, Chil4, Arg1, Mrc1*) at different time points (0, 1, 3, 6, 12 and 24 hours) of IL-4 (20 ng/ml) treatment in control (n=5) and EGR2 deficient (n=5) BMDMs.

We detected significant repression in all cases in late (12 or 24 hours) time points after IL-4 exposure. Based on this, EGR2 is a late-stage regulator of alternative macrophage polarization.

To check the influence of EGR2 in opposite way, we performed gain of function experiments transfecting mouse ESC-derived myeloid progenitors with doxycycline (DOX)-inducible EGR2 genetic construct (Figure 11).

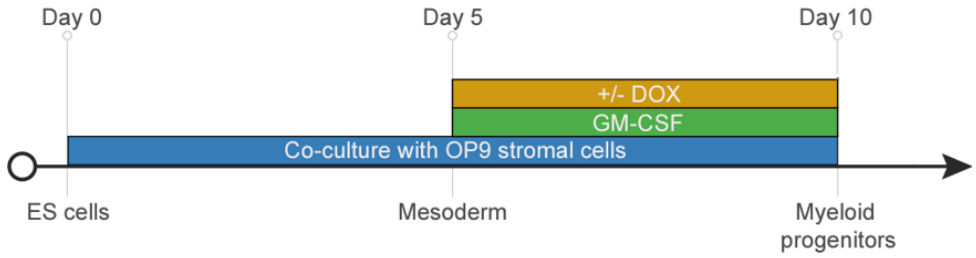

Figure 11. The treatment protocol of doxycycline inducible EGR2 expressing myeloid progenitor model.

Applying this system, first, we confirmed the overexpression of *Egr2* mRNA upon DOX treatment with RT-qPCR measurement. After we measured the same M2 marker gene set than in the loss of function experiment (Figure 12). From these genes, the mRNA level of *Retnla, Chil3, Chil4* and *Ccl17* was elevated upon EGR2 upregulation and showed additional induction after 24 hours IL-4 exposure. These results strengthened the evidence of EGR2's role in the regulation of M2 macrophage polarization.

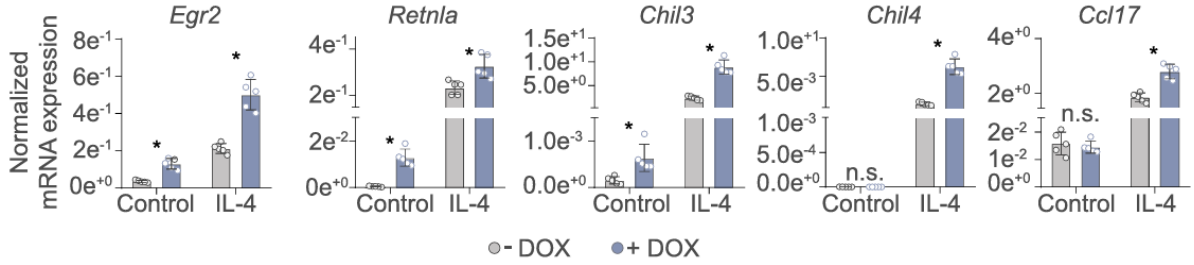

Figure 12. The overexpression of EGR2 enhance the expression of M2 markers in ES-derived myeloid progenitors. The diagrams indicate the relative mRNA expression values of *Egr2* and M2 marker genes (*Retnla, Chil3, Chil4, Ccl17*) in ESC-derived myeloid progenitor cells (n=5) in the presence or absence of DOX (1 µg/ml) and IL-4 (20 ng/ml).

Lung-resident macrophages show high expression of EGR2

After BMDMs, we wanted to examine the potential importance of EGR2 in tissue resident macrophages. By analyzing the expression of EGR family members based on already published RNA-seq datasets (GSE63340) from different tissue resident macrophage population and monocytes (Lavin 2014), we found that *Egr2* has a relative specific and strong expression in AMs (Figure 13).

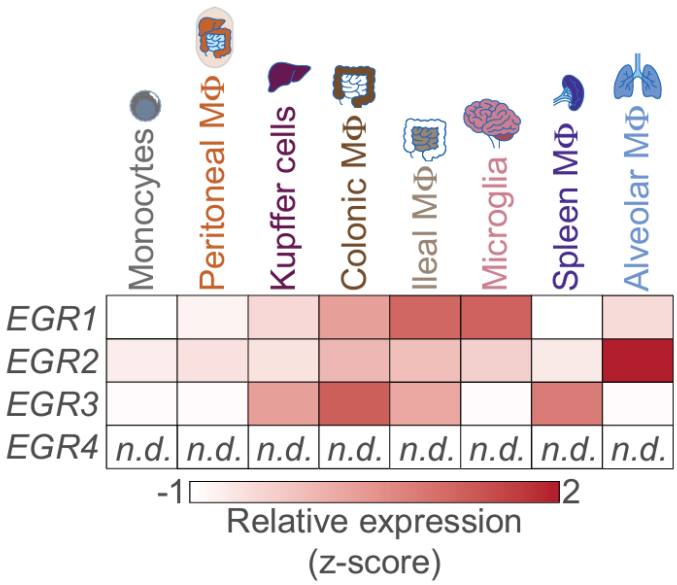

Figure 13. EGR2 is a dominantly expressed transcription factor from EGR family in alveolar macrophages. Heatmap represenation of the mRNA relative expression (z-score) of EGR members in different tissue specific macrophage populations and monocytes (reanalyzed data: GSE133747). The n.d. abbreviation means "not detected".

Based on publicly available bulk RNA-seq (Gautier 2012) and scRNA-seq data (Cohen 2018) from different stages of AM maturation we reanalyzed the expression values of different transcription factors (Figure 14).

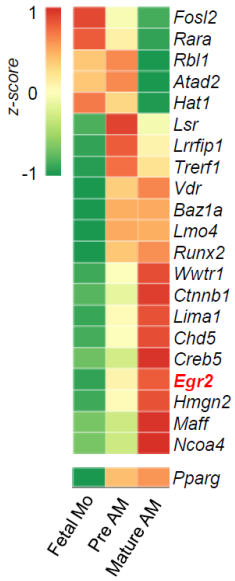

Figure 14. EGR2 is a terminal transcription factor marker of alveolar macrophage maturation. Heatmap representation of average gene expression values (z-score) of different transcription factors in the merged population of fetal monocytes (Fetal Mo), pre-AMs (Pre AM) and mature AMs (Mature AM) based on scRNA-seq data (GSE119228) at steady state.

We found that the mRNA level of EGR2 is elevated especially at the final stage of differentiation. This intriguing pattern raises the opportunity to the role of EGR2 in the coordination of specific cellular functions through epigenomic regulation of gene expression.

The myeloid-specific EGR2 deficiency leads to altered immune cell composition of lung and affects alveolar macrophage phenotype

To test our hypothesis, we started to analyze the changes upon myeloid-specific loss of EGR2 in the lung. First, we created a strategy with high dimensional flow cytometry, to measure the different cell populations of lung. The staining panel contained CD45, CD31, CD326, CD140a, CD3, CD4, CD8, CD45R-B220, TCR-γδ, CD11c, CD11b, CD64, CD103, MHCII, CD24, Ly6G, SiglecF, and Ly6C markers. We compared the total number of different cells isolated from the whole lungs of control and EGR2 myeloid-deficient mice.

The number of endothelial cells ($CD31^+$), epithelial cells ($CD326^+$), and fibroblasts ($CD140a^+$) were relatively identical (Figure 15) in the lungs of control and EGR2 myeloid KO animals.

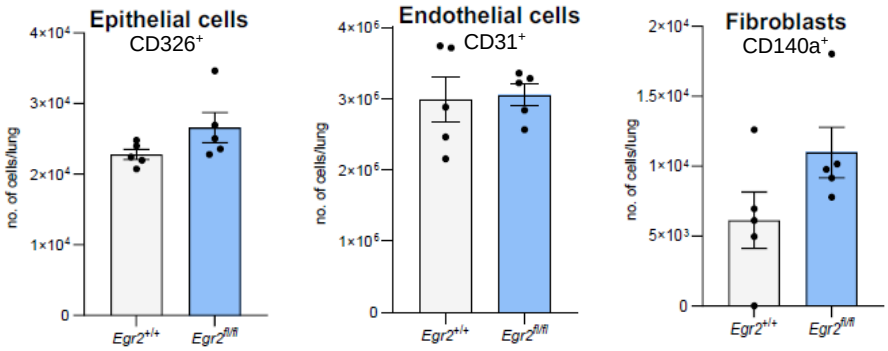

Figure 15. The number of non-immune cells of lungs are unaltered near myeloid-specific deficiency of EGR2. The columns indicate the number of epithelial cells (CD326+), endothelial cells (CD31+) and fibroblast (CD140a+) per lung of 3-month-old control (n=5) and *Egr2*$^{fl/fl}$ (n=5) mice at steady state.

Within immune cell populations we detected significant reduction in the number of mature AMs ($CD11b^-$, $CD11c^+$, and $CD64^+$) and interstitial macrophages ($CD11b^-$, $CD11c^-$,

and CD64^{+}), Ly6C^{+} monocytes, NK cells (NK1.1^{+}), B cells (CD45-B220^{+}), CD4+ and CD8+ T cells. Only the dendritic cells (CD103^{+}) showed significant elevation from analyzed populations, the number of Ly6C^{-} monocytes, neutrophil granulocytes (Ly6G^{+}), eosinophils (CD24^{+}, Ly6G^{-}, SiglecF^{+}) and γδ T (TCR-γδ^{+}) cells were roughly identical in the lungs of WT and EGR2 KO mice (Figure 16).

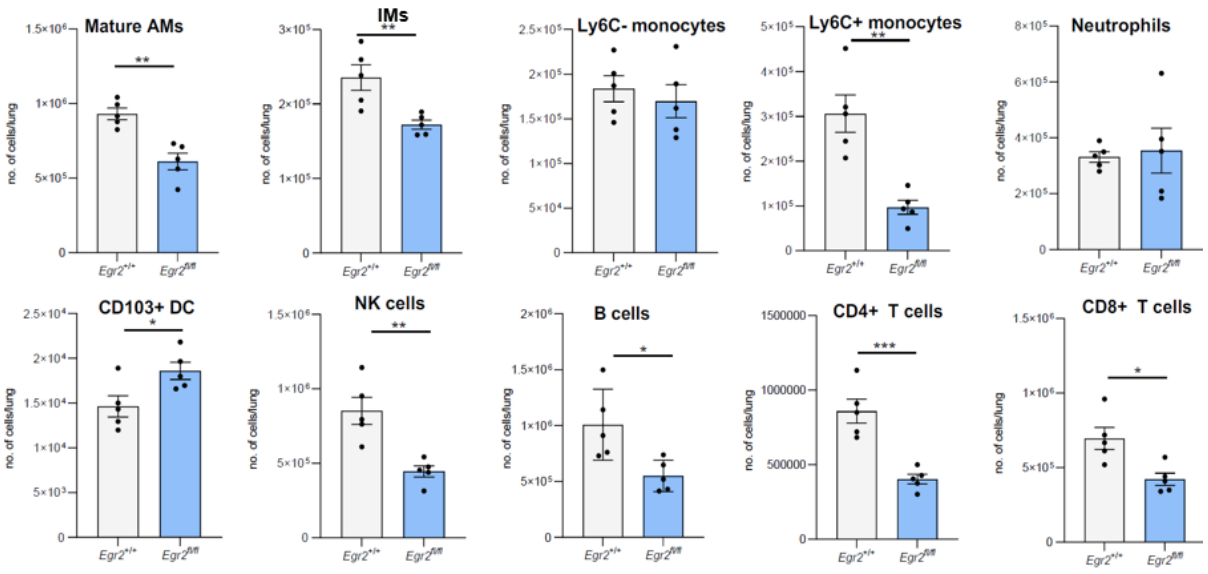

Figure 16. The number of immune cells show different distribution in the lungs of EGR2 KO mice. The column diagrams represent the number of different immune cells in the lung of 3-month-old control (n=5) and *Egr2*$^{fl/fl}$ (n=5) mice at steady state.

Our results show that EGR2 influences via direct and indirect ways the composition of myeloid and lymphoid immune cells, but not affect the presence and number of non-immune populations in the lung.

Next, we prepared formalin-fixed, paraffin embedded histological samples from EGR2 KO and WT lungs. We applied hematoxylin and eosin (H&E) and myeloperoxidase (MPO) staining for better visualization and distinguishment of cellular components (Figure 17). The general structure of lung is intact in both genetic backgrounds of mice. We observed difference in the ratio of MPO positive AMs between the WT and EGR2 lung samples. The lungs isolated from EGR2 deficient animals represents higher number of AMs within the same area of tissue. The

representative images (Figure 17) show one MPO-positive macrophage in the WT lung and eight MPO-positive cells in the KO condition within the same-sized area. This finding seems to be opposite as the tendency of flow cytometry measurements. To solve the discrepancy, we examined the maturity status of AMs localized in the bronchoalveolar space by quantify the expression of CD11b, CD11c, F4/80 and SiglecF proteins as well-known markers that represents different stages of AM differentiation.

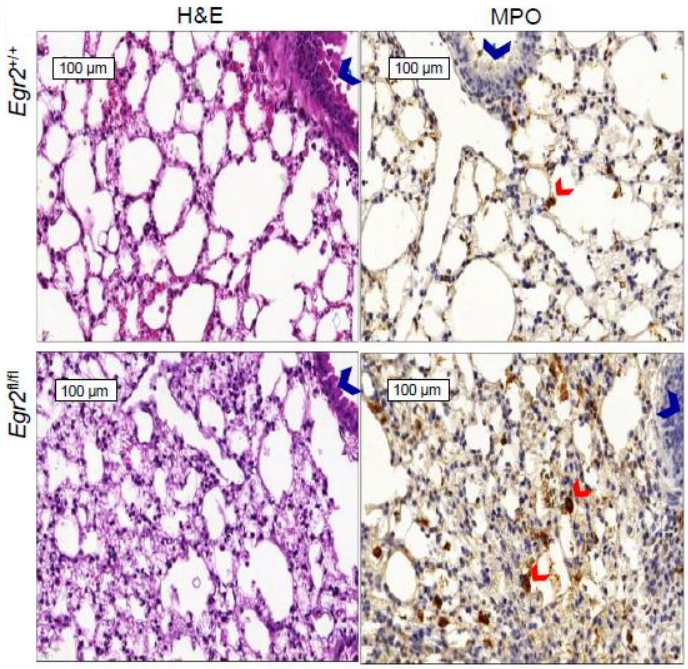

Figure 17. Elevated number of AMs is observed in the lungs of EGR2 KO mice. The H&E- and MPO-stained representative histological images from lungs of WT and EGR2 KO 3 month-old mice at steady state. Blue arrows indicate bronchus and red arrows marks the MPO positive AMs.

The terminally differentiated AMs are positive for the standard immune cell marker CD45, and show high expression of F4/80, CD11c, and SiglecF. The expression of CD11b reduces during AM maturation. We defined the AMs from whole lung homogenate, and we also isolated them by BAL to avoid the potential mistakes that could occur because of unexpected dysregulation of standard markers. We got similar results in both ways.

In the CD45^{+} cell population of control and EGR2 deficient lungs the AM subpopulation was separable based on F4/80 and CD11c expression in both conditions. The number of AM were significantly elevated in *Egr2*$^{fl/fl}$ lungs. We selected this population and analyzed the SiglecF and CD11b expressions. In *Egr2*$^{fl/fl}$ samples we detected a near total loss of SiglecF^{+} subgroup of AMs and the ratio of CD11b^{+} cells were significantly higher (Figure 18).

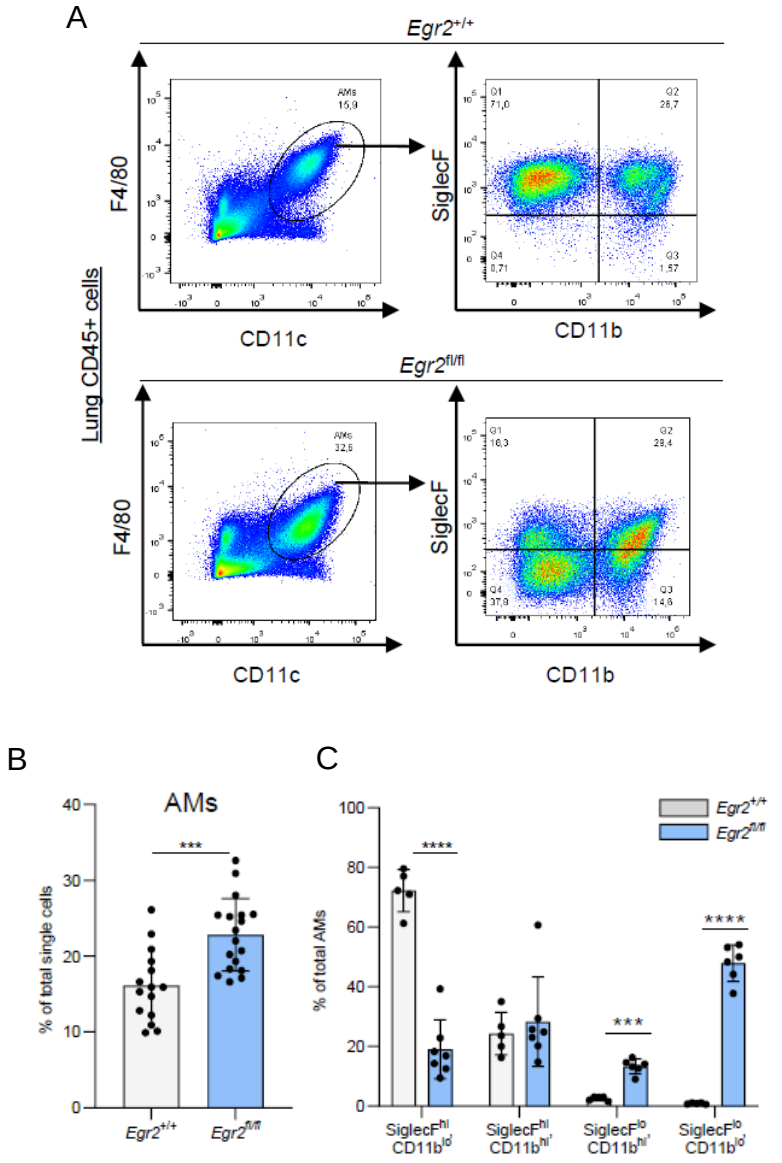

Figure 18. The canonical AM marker expression pattern is influenced by EGR2. (A) Representative pseudo color dot plots of lung CD45^{+} cells from *Egr2*$^{+/+}$ and *Egr2*$^{fl/fl}$ mice stained by F4/80 and CD11c antibodies, and the expression of SiglecF and CD11b within F4/80 and C11c double positive cells (flow cytometry). **(B)** The percentage (mean±SEM) of AMs (F4/80+ and CD11c+ cells) within lung CD45^{+} population from *Egr2*$^{+/+}$ and *Egr2*$^{fl/fl}$ mice. **(C)** The ratio (mean±SEM) of different AM subpopulations based on SiglecF and CD11b expression in the lungs of WT and EGR2 KO mice.

We isolated the bronchoalveolar CD45+ cells and stained them by the same markers. The F4/80 expression was unaltered by EGR2 deficiency and the expression of CD11c significantly but just slightly was reduced in KO samples. The robust reduction of SiglecF was observed and we detected elevation in CD11b expression (Figure 19). These results the same as previous ones from total lung homogenates. We concluded that the definition of AM population was accurate in both ways. The myeloid-specific loss of EGR2 does not completely block the differentiation of AMs but leads to a modulated maturation phenotype.

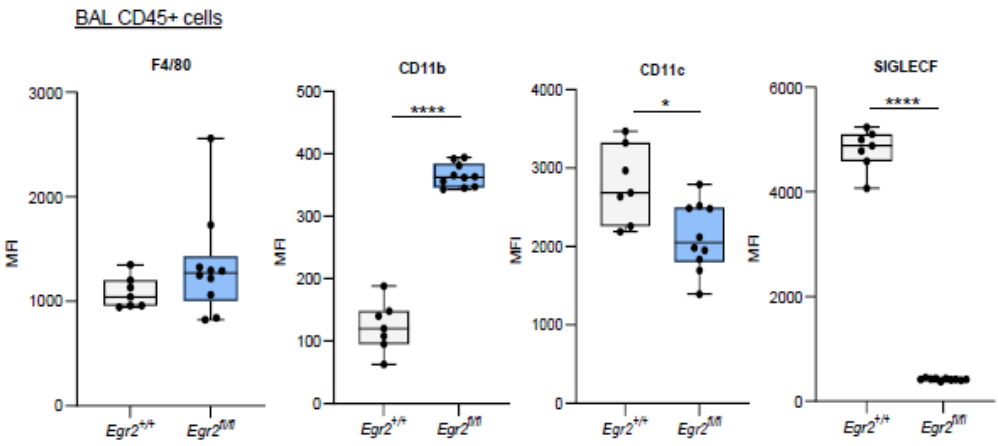

Figure 19. The expression of AM markers in cells isolated by BAL. The box plots represent the median fluorescence intensity (MFI) (mean±SEM) of F4/80, Cd11b, CD11c and SiglecF AM markers in BAL-isolated CD45+ cells measured by flow cytometry from *Egr2*$^{+/+}$ (n=7) and *Egr2*$^{fl/fl}$ (n=10) lung samples at steady state.

To characterize the general metabolic functionality of EGR2 deficient AMs we used Agilent Seahorse XF Analyzer-based experiments, and we determined the mitochondrial oxygen flux and ECAR. We isolated AMs by BAL then we *ex vivo* measured the metabolic processes. In basal, etomoxir-, and oligomycin-dependent respiration essentially identical OCR values have occurred in *Egr2*$^{+/+}$ and *Egr2*$^{fl/fl}$ cells. In the case of ECAR, we detected a low range of reduction in *Egr2*$^{fl/fl}$ cells (Figure 20).

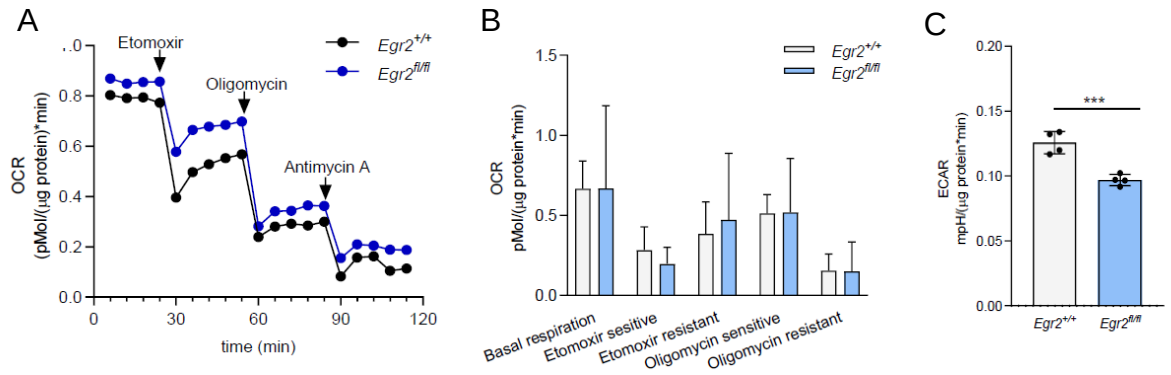

Figure 20. The basal metabolic activity is intact in EGR2 deficient AMs. (A) The OCR (mean±SEM) and **(C)** ECR (mean±SEM) values of *Egr2*$^{+/+}$ and *Egr2* $^{fl/fl}$ AMs measured by Agilent Seahorse Analyzer. **(B)** The bar graph representation of OCR values (mean±SEM) after etomoxir (50 µM), oligomycin (2 µM), and antimycin A (10 µM) treatment in *Egr2*$^{+/+}$ (n=7) and *Egr2* $^{fl/fl}$ (n=5) (n=5) AMs by Agilent Seahorse Analyzer.

Finally, we concluded the myeolid-specific deficiency of EGR2 leads to a metabolically intact macrophage, which locates in the alveolar place in higher ration than normal AMs and represent a unique profile of cell surface markers.

EGR2 as a likely direct DNA bound transcription factor is a dominant modulator of alveolar macrophage epigenome

Next, we sought to understand the molecular events mediated by EGR2 in the chromatin of AMs, so we performed ATAC-seq and described the differences in chromatin openness of EGR2 sufficient and deficient AMs. We applied three biological replicates in different groups, which highly correlated with each other in all conditions (Figure 21).

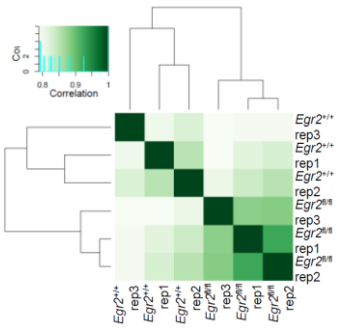

Figure 21. The correlation heatmap shows the high similarity of ATAC-seq samples.

The color intensity represents the correlation between the ATAC-seq samples based on read coverages.

Then we analysed the differences in chromatin accessibility between *Egr2*$^{+/+}$ and *Egr2*$^{fl/fl}$ AMs. We identified 1906 closing and 4792 opening significantly changed genomic regions in the chromatin in *Egr2*$^{fl/fl}$ AMs compared to *Egr2*$^{+/+}$ cells (Figure 22 A). We mapped the genomic distribution profile of differentially accessible regions (DARs). Both classes of DARs were localized in larger proportion at enhancer region than promoter region and the average coverages were lower at enhancers (Figure 22 B).

Although the opening DARs and the unchanged regions exhibit a similar distribution with a relatively high proportion of promoter-transcription start sites (TSS) at 23.8% and 25.8% respectively, there is a notable decrease in the number of closing DARs within the promoter-TSS category, which stands at 10.6% (TSS -1000 bp/+100 bp). Conversely, closing DARs have a greater representation in intergenic regions at 42.5%, compared to 26.2% and 31% for unchanged and opening DARs. This pattern is notably indicative of TF-bound regulatory enhancers (Figure 22 C).

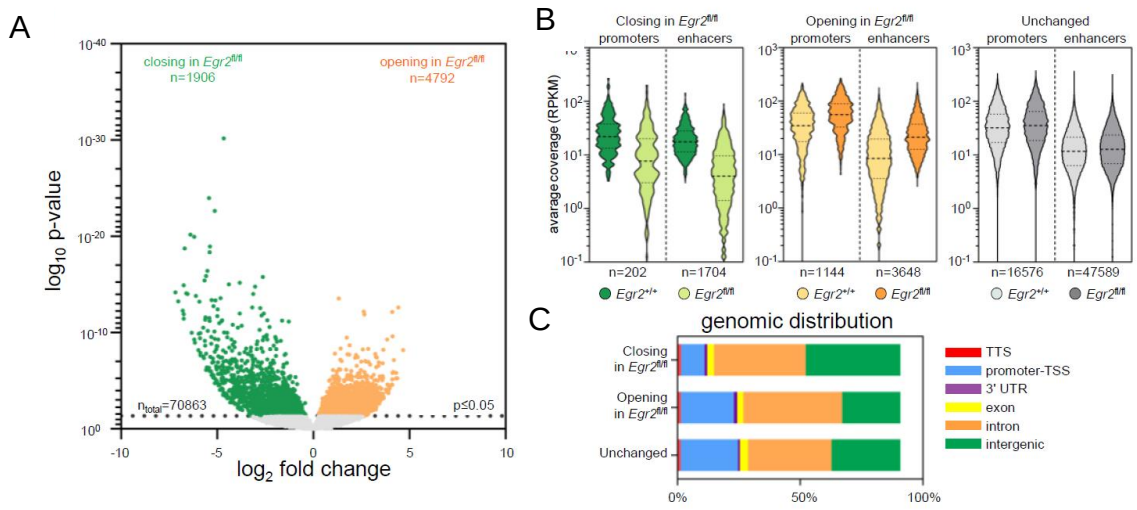

Figure 22. Changing in chromatin openness supports the importance of EGR2 in epigenomic regulation of AMs. (A) The volcano plot shows the opening (n=4792), closing (n=1906), and unchanged (n=64165) differential regions between *Egr2*$^{+/+}$ and *Egr2*$^{fl/fl}$ cells (ATAC-seq). **(B)** The violin plots represent the average coverage (RPKM) values of the closing (green), opening (yellow) regions and unchanged (grey) chromatin regions between *Egr2*$^{+/+}$ versus *Egr2*$^{fl/fl}$ AMs (Paired t-test, p≤0.05) at the promoter and enhancer regions. **(C)** The stacked bar chart represents the genomic distribution of DARs and unchanged chromatin regions between *Egr2*$^{+/+}$ versus *Egr2*$^{fl/fl}$ AMs (TSS: transcription start site; 3′ UTR: 3′ untranslated region; promoter-TSS covers both TSS -1000-bp/+100-bp and 5′ UTRs; intergenic: both intergenic and non-coding regions).

To identify sequence motifs for transcription factors that directly bind to DNA within DARs, we conducted a *de novo* motif enrichment analysis (Figure 23 A). For closed DARs, there was a significant enrichment of EGR motifs (50.53%), followed C/EBP motifs (32.06%). We also identified motifs for general macrophage-specific LDTFs, such as PU.1, AP-1, and RUNX. Analyzing the specificity of EGR, C/EBP, PU.1, and AP-1 motifs revealed that closing regions predominantly featured strong, canonical EGR and C/EBP motifs. In contrast, the strength of PU.1 and AP-1 motifs was similar between unchanged regions and DARs, supporting their proposed role as LDTFs (Figure 23 B).

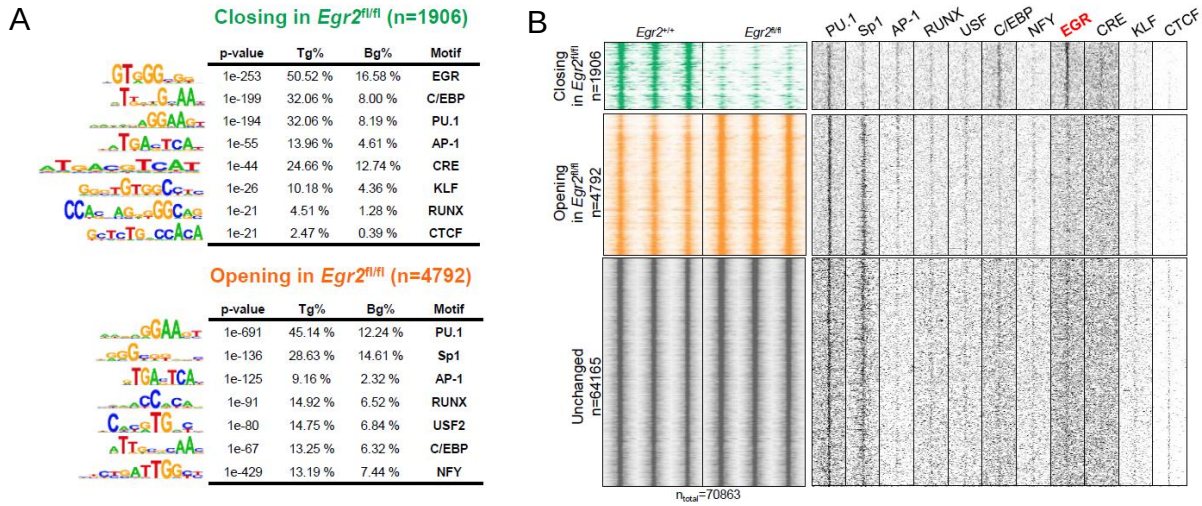

Figure 23. The EGR motif is enriched under reppressed ATAC-seq peaks. (A) *De novo* motif enrichment of differentially closing (green) and opening (orange) chromatin regions for *Egr2*$^{+/+}$ versus *Egr2*$^{fl/fl}$ AMs. The significantly enriched motif matrices are presented along with the p-value rank in the analysis and the target% values are indicated in brackets. **(B)** Read distribution heatmap represents the openness of DARs (closing, opening and unchanged) in *Egr2*$^{+/+}$ and *Egr2*$^{fl/fl}$ cells (2 kbp frames relative to the summit) and the motif distribution heatmaps shows the presence of indicated binding motifs (2 kbp frame relative to the summit).

Notably, the absence of EGR motif enrichment in the opening sites suggests that EGR2 is unlikely to function as a direct repressor through direct DNA binding.

From these results, we concluded that EGR2 functions as a direct DNA-binding transcription factor in AMs, serving as an epigenomic factor essential for maintaining chromatin openness and likely activating gene expression at sites marked by macrophage

LDTFs. To further investigate EGR2's molecular function, we decided to integrate chromatin accessibility studies with transcriptomic analyses.

EGR2 directly regulates transcription in alveolar macrophages

To uncover the molecular specifics of these likely direct activating transcriptional events, we examined the connection between potential EGR2-bound enhancers and their associated regulated genes. Consequently, we conducted bulk RNA-seq experiments on control and *Egr2*$^{fl/fl}$ AMs in their steady state. This led to the identification of 364 significantly repressed and 621 significantly induced genes in AMs lacking EGR2 (Figure 24).

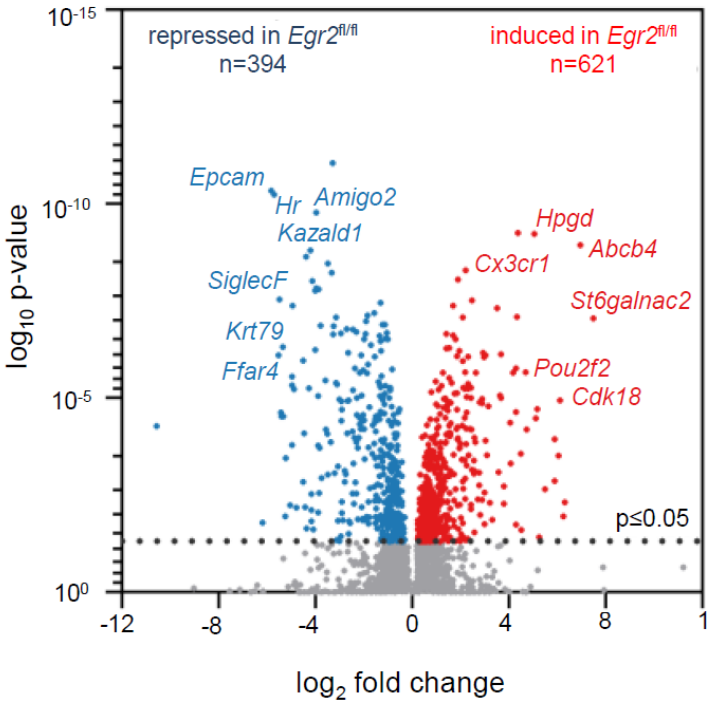

Figure 24. The EGR2 deficiency leads a largely altered gene expressional profile. The volcano plot shows the DEGs (reppressed: blue, induced: red) between *Egr2*$^{+/+}$ (n=3) and *Egr2*$^{fl/fl}$ (n=3) AMs at steady state.

Among the genes that exhibit changes, the mature AM markers *SiglecF*, *Krt79*, and *Kazald1* show a significant decrease, whereas the genes *Cx3cr1* and *Abcd4* are the most highly upregulated ones.

By linking the closing DARs to the repressed differentially expressed genes (DEGs), we discovered that a large number of closed DARs were located within a 100 kilobase pair (kbp) distance (n=373, with 178 of these featuring at least one EGR motif). However, over 1000 DARs were positioned more than 1000 kbp away from a repressed gene, indicating a potential chromatin and/or epigenomic remodeling role of EGR2 (Figure 25).

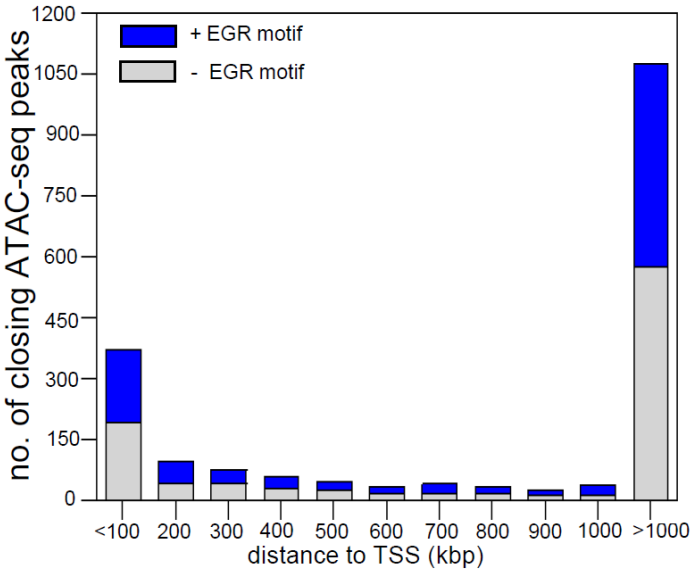

Figure 25. The distribution of DARs relative to altered DEGs. The bar chart illustrates the distribution of distances (kbp) of closing DARs, either containing (blue) or not containing (grey) EGR motifs, relative to the transcription start sites (TSS) of repressed DEGs.

To further investigate the potential direct transcriptional regulatory role of EGR2, we integrated the DARs and DEGs by employing a more stringent criteria of ±100 kbp distance from the gene's TSSs. We adjusted and shortened this integrative region when a gene's coding region was closer (Figure 26).

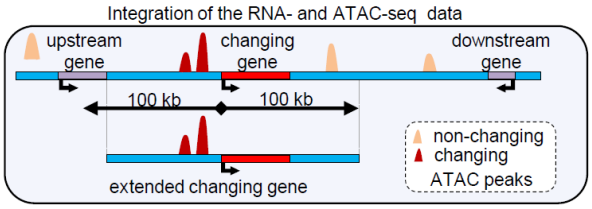

RNA-seq / ATAC-seq	induced in *Egr2*$^{fl/fl}$ (621 genes)	repressed in *Egr2*$^{fl/fl}$ (394 genes)
opening in *Egr2*$^{fl/fl}$ (4792 peaks)	**292 genes** **673 peaks**	67 genes 87 peaks
closing in *Egr2*$^{fl/fl}$ (1906 peaks)	24 genes 26 peaks	**158 genes** **307 peaks**

Figure 26. Diagram illustrating the integration of DARs and DEGs and displays the counts of DEGs and their associated DARs.

We identified 158 repressed DEGs as potential direct targets of EGR2, linked to 307 closed DARs according to our criteria (Figure 26). The closing DARs connected to repressed DEGs and containing EGR motifs suggest that EGR2 likely functions as a transcriptional activator in AMs.

We further categorized these proximal probable direct target genes into repressed (n=52), absolute (n=44), and relative (n=62) EGR2-dependent groups based on the presence of the EGR motif and their gene expression levels. A baseline expression level was set at 2.5 FPKM for the *Egr2*$^{fl/fl}$ condition, with genes below this threshold considered non-expressed. It's important to note that absolute EGR-dependent genes are expressed at lower levels compared to relative EGR-dependent genes (Figure 27).

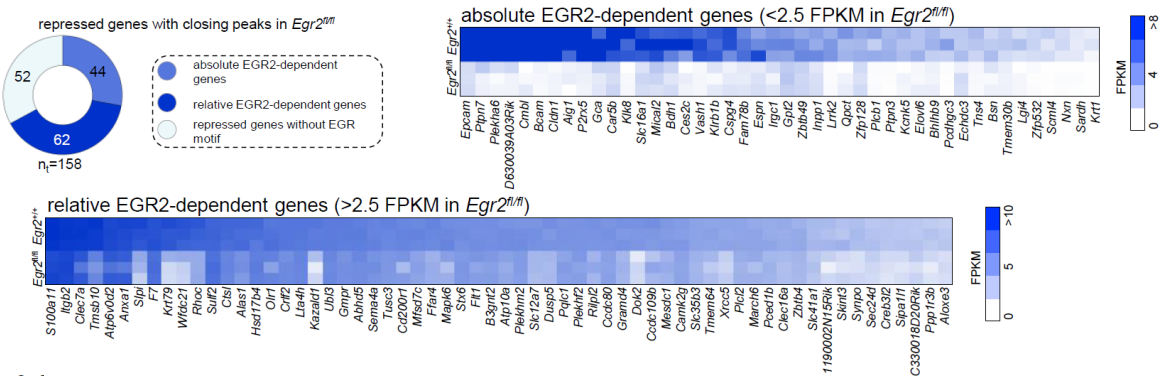

Figure 27. The determination of absolute and relative EGR2 dependent genes in AMs. The pie chart illustrates the proportion of downregulated DEGs with closing DARs in *Egr2*$^{fl/fl}$ AMs: those containing an EGR motif (moderate blue for absolute EGR2-dependent, dark blue for relative EGR2-dependent) and those without an EGR motif (light blue). The heatmaps display gene expression patterns of repressed genes in *Egr2*$^{fl/fl}$ AMs that are associated with closing DARs containing EGR motifs, categorized by their expression levels as either below or above 2.5 FPKM in *Egr2*$^{fl/fl}$ samples.

The identified differentially accessible chromatin regions serve as EGR2-dependent enhancers

To obtain clearer evidence of the epigenetic regulatory role of EGR2 and to further explore the epigenomic differences between WT and EGR2-null cells, we conducted CUT&RUN experiments focusing on the H3K4me3 histone mark to identify active gene promoters and on BRD4 as a marker of active enhancers and promoters. By analyzing the distribution of the H3K4me3 signal in the 500 bp downstream region relative to the TSS of absolute and relative EGR2-dependent genes, we observed that H3K4me3 levels corresponded with differences in gene expression, reinforcing the idea that EGR2 primarily activates chromatin structure and gene regulation. As a control, we also measured the H3K4me3 signal on the TSS of 292 induced genes associated with opening regions, which showed the expected opposite outcome (Figure 28). BRD4 showed a similar pattern at promoters and enhancers, further supporting EGR2's significant role as an epigenetic regulator.

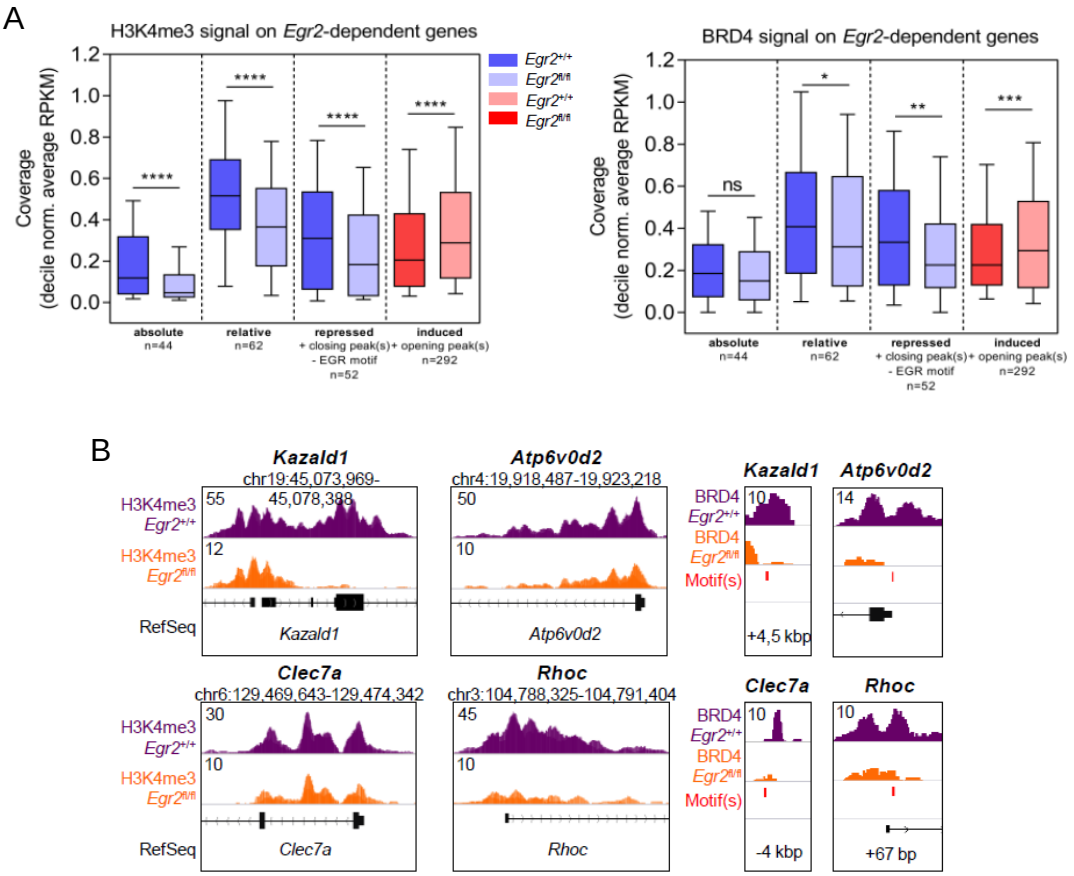

Figure 28. The results of H3K4me3 and BRD4 CUT&RUN experiments. (A) The box plots display the coverage (decile normalized average RPKM) of the H3K4me3 mark at the TSSs and the BRD4 mark at EGR motif-containing associated enhancers for absolute and relative EGR2-dependent repressed genes, for repressed genes linked to closing DARs lacking an EGR motif, and for induced genes linked to opening DARs. **(B)** IGV snapshots illustrate the presence of the H3K4me3 mark at the promoters of the specified genes and the BRD4 signal at the associated EGR motif-containing enhancers.

We also developed an eRNA-specific RT-qPCR assay targeting the DAR containing the EGR motif associated with the *Kazald1* gene to directly evidence enhancer activity dependent on EGR2 presence. The eRNA production decreased in EGR2-null AMs, matching a reduction in the ATAC-seq peak (Figure 29).

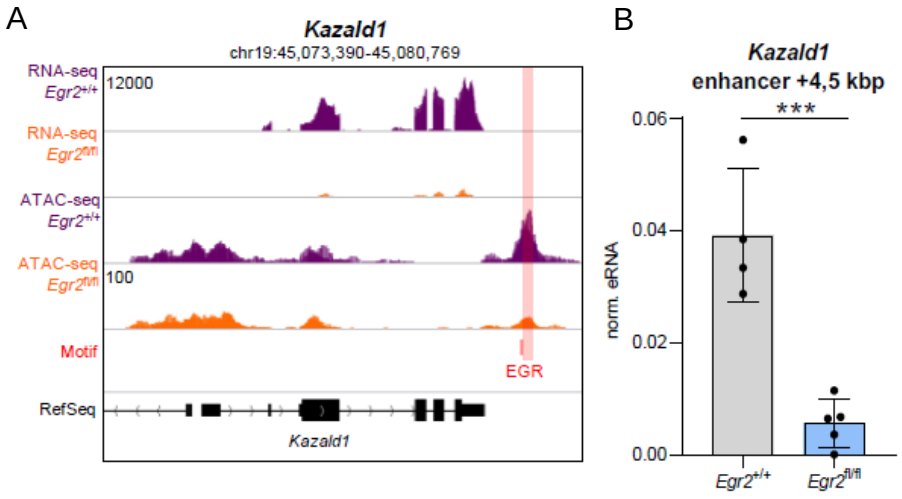

Figure 29. Repressed DARs acts as enhancers of EGR2. (A) IGV visualization of RNA-seq, and ATAC-seq coverages (overlayed) and the EGR motif on *Kazald1*. **(B)** The columns represent the relative eRNA expression (mean±SEM) of *Kazald1*-related closing DAR with EGR motif in *Egr2*$^{+/+}$ and *Egr2*$^{fl/fl}$ samples.

Encouraged by these findings, we performed gain-of-function experiments on ESC-derived myeloid progenitors with a DOX-inducible EGR2 genetic construct. In this system, RT-qPCR analysis confirmed *Egr2* mRNA overexpression upon DOX treatment, resulting in significantly elevated levels of mRNA and protein for the CD11c and SIGLECF AM marker genes (Figure 30 A, B). We also examined transcriptional changes in a selection of potential direct target genes (*Kazald1*, *Clec7a*, *Atp6v0d2*, *Rhoc*) and their associated enhancers, which showed an upregulation trend following EGR2 overexpression (Figure 30 C, D). These experiments led us to conclude that the identified DARs serve as enhancers, and their activity depends on EGR2.

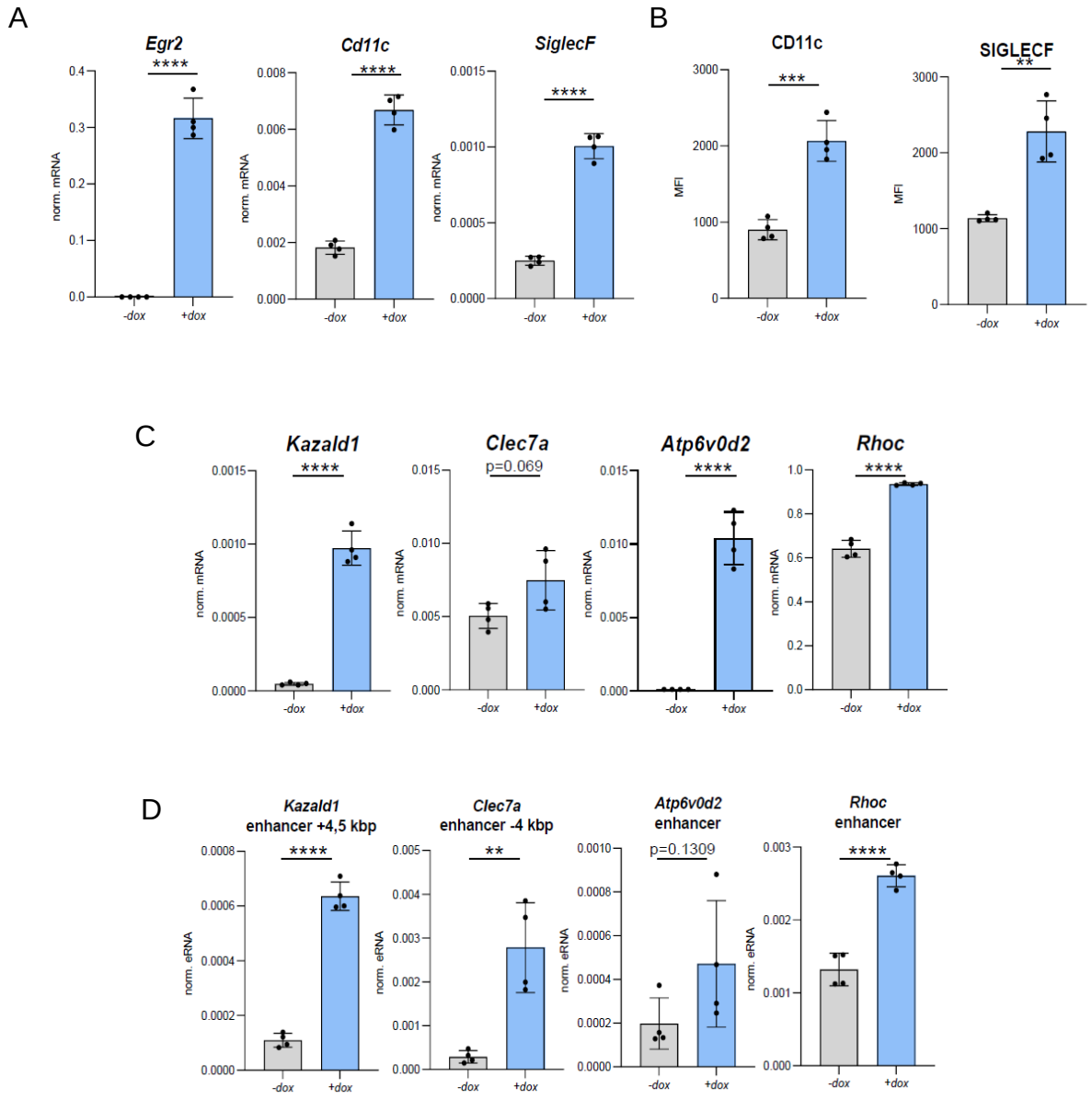

Figure 30. Gain-of-function experiments proved the potency of EGR2 in gene activation. (A) The column charts display the relative mRNA expression levels (mean±SEM) of the *Egr2* gene and the AM marker genes *Cd11c* and *SiglecF* in myeloid progenitors either untreated (-dox) or treated with doxycycline (+dox). (**B**) The box plots present the levels (MFI±SEM) of CD11c and SIGLECF proteins in untreated (-dox) or doxycycline-treated (+dox) myeloid progenitors, as measured by flow cytometry. (**C-D**) Column charts illustrate the relative mRNA expression (**C**) and eRNA expression (**D**) levels (mean±SEM) of representative EGR2-dependent genes (**C**) and their corresponding enhancers (**D**) in untreated (-dox) or doxycycline-treated (+dox) myeloid progenitors.

EGR2 is a transcriptional regulator of terminal AM identity and pathogen inactivation

Next, we analyzed both the potential direct and indirect EGR2-dependent DEGs from a functional perspective. In the absence of EGR2, the mRNA levels of core macrophage marker

genes and AM signature genes were partially altered (Figure 31 A). However, nearly half of the altered AM signature genes, including *Epcam, Krt79, Cldn1*, and *Kazald1*, appeared to be proximal EGR2 targets, with $\log_2$ fold-change values ranging from -4 to -6 (Figure 31 B).

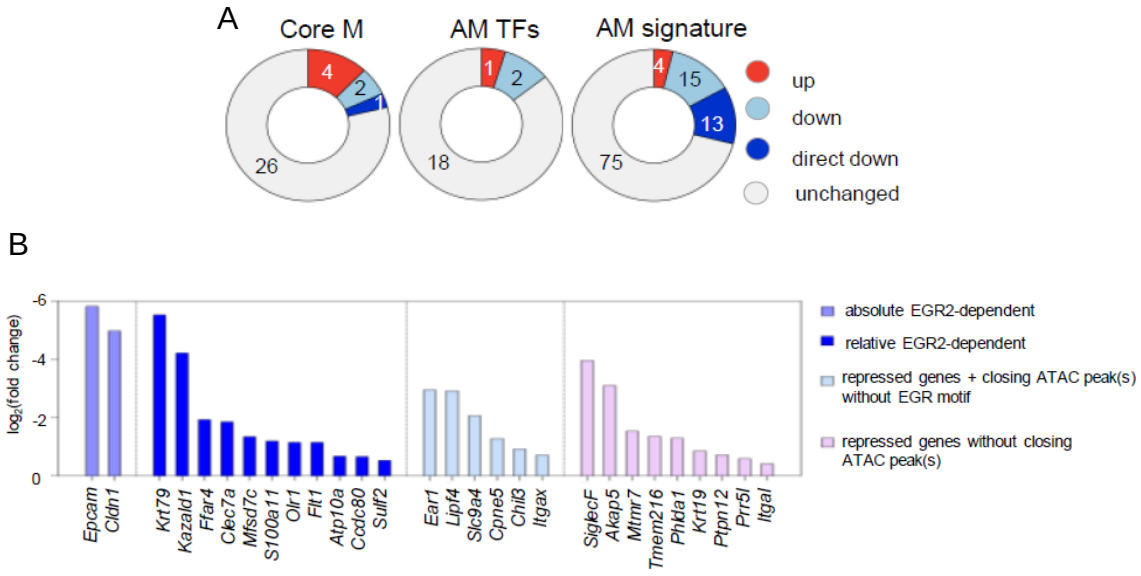

Figure 31. The ratio of altered macorphage or alveolar macrophage specific genes in EGR2 KO mice. (A) The pie charts illustrate the count of genes in *Egr2*$^{fl/fl}$ samples that remain unchanged (gray), are upregulated (red), downregulated (light blue), or directly downregulated (dark blue; linked to EGR motif–containing peaks). These genes overlap with the core macrophage gene set (Core M), the AM-specific transcription factors (AM TFs), and the AM signature gene set (AM signature). **(B)** The column plot displays the $\log_2$ (fold-change) values of downregulated AM signature DEGs, divided into four groups based on their association with closing DARs and the presence of an EGR motif.

It is noteworthy that the *SiglecF* gene shows a significant decrease within the repressed group, as it is the most recognized phenotypic marker of mature AMs (Figure 31). We confirmed a near-total reduction at the protein level through flow cytometric analysis (Figure 19) and demonstrated EGR2-dependent induction of this protein in gain-of-function studies (Figure 30). Next, we used the KEGG database to predict the biological pathways affected by the list of DEGs. The top categories related to pathogen elimination were ranked by the number of DEGs overlapping with each pathway (Figure 32 A). We organized the genes by their primary biological functions according to these pathways. The transcriptional changes

associated with the absence of EGR2 are related to pathogen recognition, ROS formation, phagolysosome acidification, and maturation. Additionally, these DEGs influence cytoskeleton organization, cell adhesion, and movement (Figure 32 B).

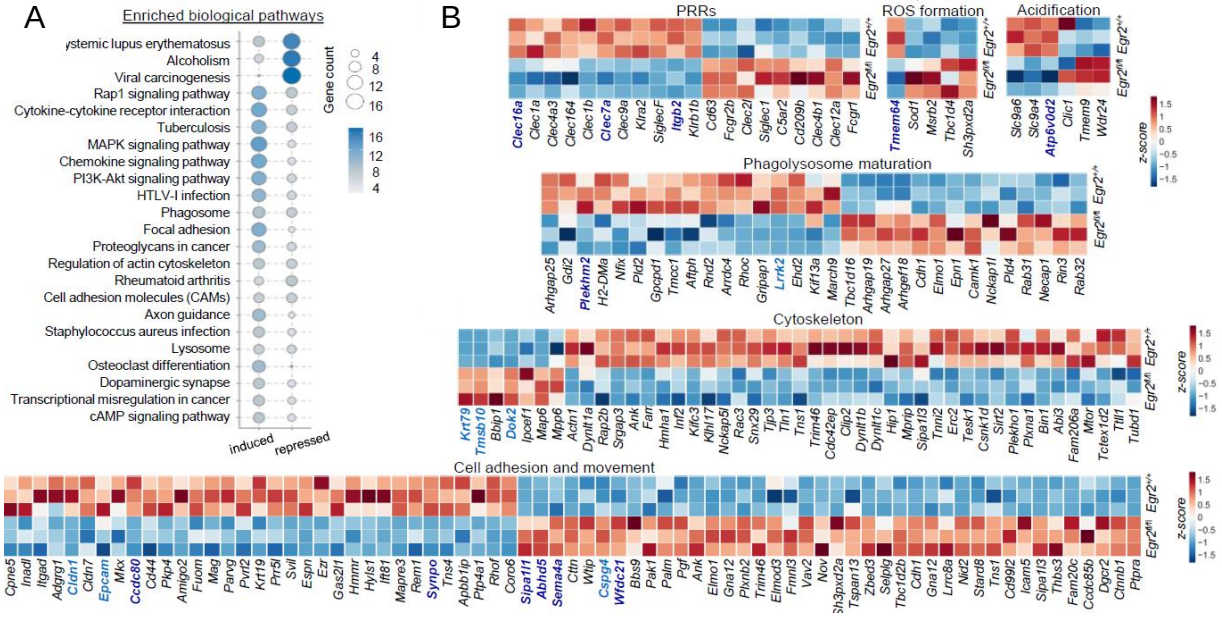

Figure 32. The absence of EGR2 impacts gene networks associated with pathogen recognition and elimination. (A) The proportional dot plot illustrates the enriched KEGG biological pathways associated with the 394 repressed and 621 induced genes in *Egr2*$^{fl/fl}$ as determined by RNA-seq. The top pathways were selected and displayed based on the total number of target genes. **(B)** The row-normalized heatmaps show significant expression changes in phagocytosis-associated genes between *Egr2*$^{+/+}$ (n=3) and *Egr2*$^{fl/fl}$ (n=3) AMs at steady state.

Among these genes, several are part of a transcriptional network involved in regulating pathogen elimination. We identified key proximal targets of EGR2, including *Atp6v0d2*, which codes for an essential proton pump (Murase 2018); *Itgb2*, which codes for a cell adhesion molecule; *Rhoc*, a small GTPase involved in cytoskeleton organization (Egami 2017); and Tmsb10, which encodes beta-thymosin and plays a role in cell motility (Figure 33 A). Once more, utilizing eRNA measurements, we demonstrated that enhancers containing EGR2 binding sites are connected to genes that exhibit reduced activity when EGR2 is absent (Figure 33 B).

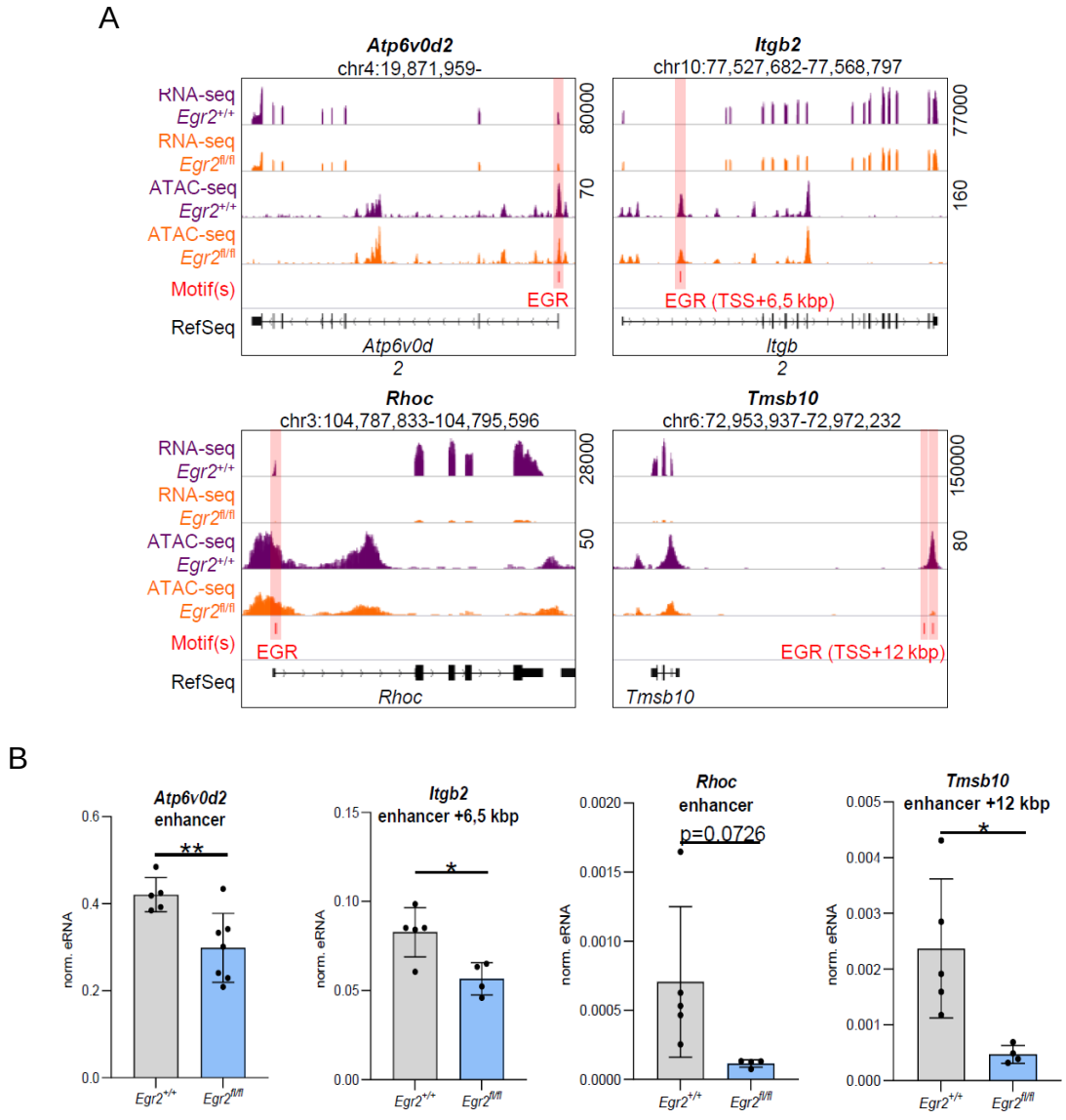

Figure 33. The phagocytosis-related genes potencially regulated by EGR2. (A) IGV visualization illustrates the RNA- and ATAC-seq coverages along with the presence of EGR motifs (highlighted in red) in *Egr2*$^{+/+}$ and *Egr2*$^{fl/fl}$ AMs for four selected probable direct EGR2 target genes (overlaid). **(B)** The columns display the relative eRNA expression (mean±SEM) values of selected repressed EGR2-dependent genes related to phagocytosis, particularly those linked with closing DARs containing EGR motifs, in *Egr2*$^{+/+}$ (n = 5) and *Egr2*$^{fl/fl}$ (n = 4) samples.

Additionally, we observed decreased H3K4me3 signals at the promoter regions, along with reduced BRD4 signals at the enhancers associated with the *Kazald1*, *Atp6v0d2*, and *Rhoc* genes (Figure 28). This evidence supports the conclusion that EGR2 acts as a proximal and likely direct transcriptional regulator of terminal AM identity, phagocytosis, and pathogen inactivation.

The absence of EGR2 results in impaired zymosan phagocytosis

Our findings led us to investigate some of the critical pathways in detail. In EGR2-deficient AMs, the BRD4 marks (Figure 28) and eRNA levels (Figure 34 B) of an enhancer linked to *Clec7a* were significantly reduced, as was the H3K4me3 signal at the gene's promoter (Figure 28), reinforcing this observation. *Clec7a* encodes the Dectin-1 receptor, a well-known pattern recognition receptor (PRR) for fungal cell wall components like zymosan, which is essential in the antifungal response of AMs. We assessed Dectin-1 protein expression on the surface of both control and EGR2-null AMs using flow cytometry on cells isolated from BAL. Reflecting its mRNA levels, the protein levels of Dectin-1 were considerably lower in *Egr2*$^{fl/fl}$ AMs (Figure 34 C).

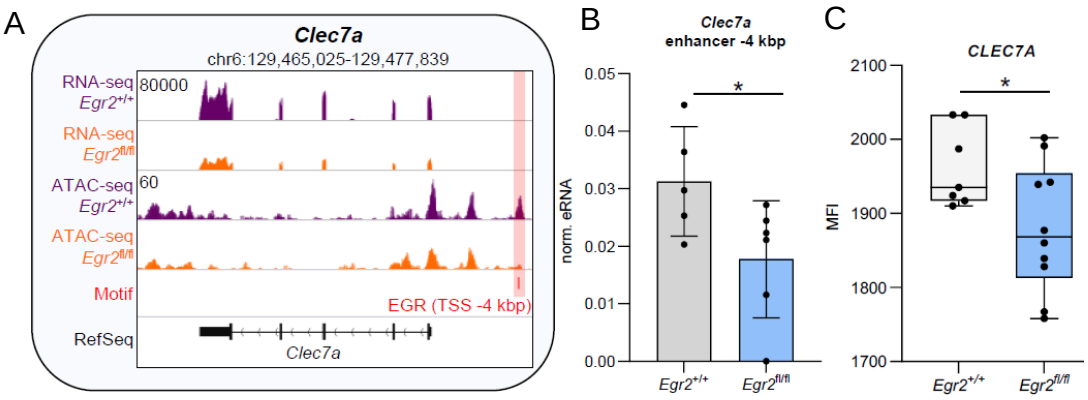

Figure 34. Reduced expression of Dectin-1 occurs in EGR2 KO AMs. (A) IGV visualization showcases the RNA-seq and ATAC-seq coverages for *Egr2*$^{+/+}$ and *Egr2*$^{fl/fl}$ AMs, highlighting the presence of EGR motifs (highlighted in red) at the Clec7a locus. **(B)** The columns illustrate the relative eRNA expression levels (mean± SEM) of Clec7a-associated closing DARs containing EGR motifs in *Egr2*$^{+/+}$ (n = 5) and *Egr2*$^{fl/fl}$ (n = 5) samples. **(C)** The box plot displays the CLEC7A expression (MFI ± SEM) in AMs isolated from BAL in *Egr2*$^{+/+}$ (n = 7) and *Egr2*$^{fl/fl}$ (n = 10), as measured by flow cytometry.

To functionally assess the activity of this protein, we examined the zymosan uptake in *Egr2*$^{+/+}$ and *Egr2*$^{fl/fl}$ AMs *ex vivo* using a pHrodo-conjugated zymosan bioparticle assay. The pHrodo dye emits a pH-dependent fluorescent signal in the acidic environment of the

phagolysosome. After 3 hours, we observed a significant reduction in the proportion of phagocytosing EGR2-null AMs compared to WT AMs, with their phagocytic capacity reduced to approximately 70% (Figure 35 A). Additionally, the MFI of the pHrodo signal was 15% lower in phagocytosing EGR2-deficient AMs (Figure 35 B).

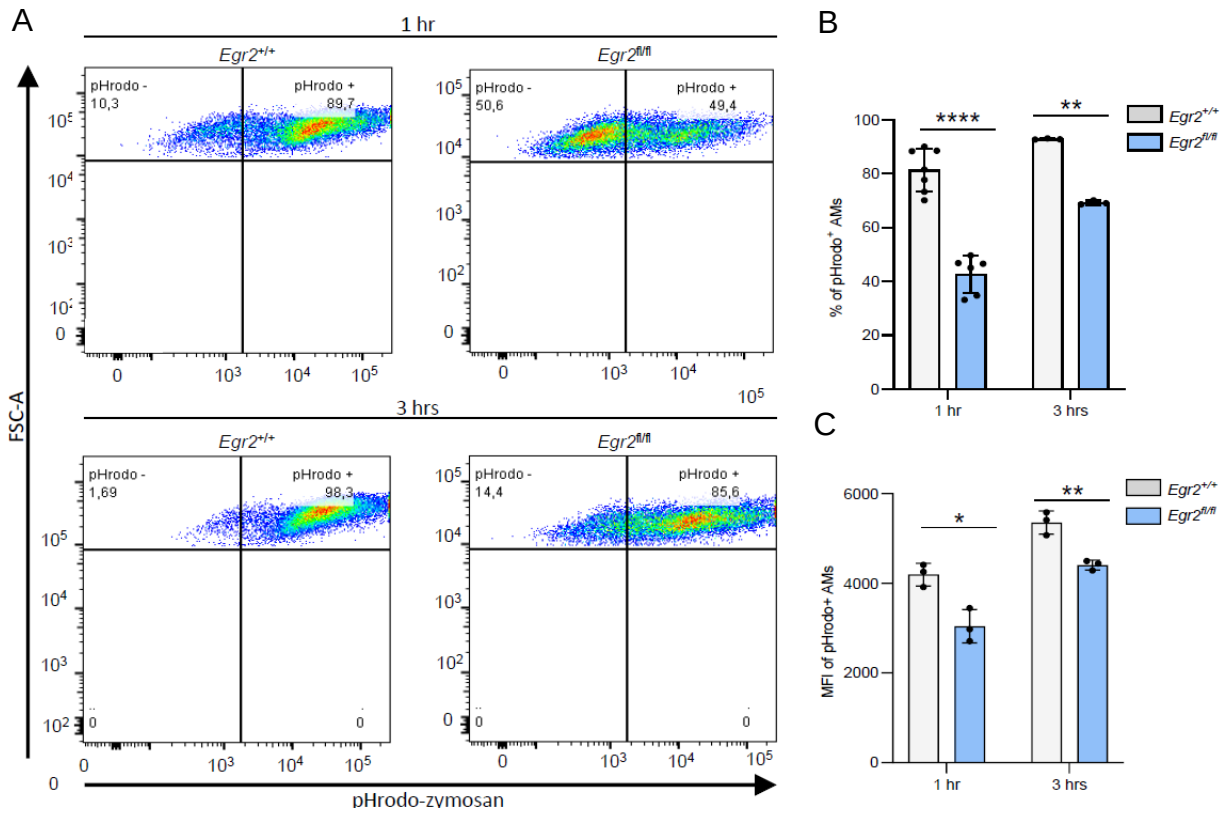

Figure 35. The zymosan uptake is reduced in EGR2 KO AMs. (A) Pseudocolor dot plots of *Egr2*$^{+/+}$ and *Egr2*$^{fl/fl}$ AMs following 1 hour and 3 hours treatments with pHrodo Red-conjugated zymosan (flow cytometry). (B) Bar graphs show the (mean ± SEM) percentage of non-phagocytotic (pHrodo–) and phagocytotic (pHrodo+) AMs after 1 hour and 3 hours pHrodo Red-conjugated zymosan (1x10^6) treatments in *Egr2*$^{+/+}$ (n = 7/n = 3) and *Egr2*$^{fl/fl}$ (n = 6/n = 3) AMs (flow cytometry). (C) The mean ± SEM MFI values for phagocytotic (pHrodo+) AMs after 1 hour and 3 hours pHrodo Red-conjugated zymosan (1x10^6) treatment in *Egr2*$^{+/+}$ (n = 3) and *Egr2*$^{fl/fl}$ (n = 3) AMs (flow cytometry).

Additionally, we used confocal microscopy to monitor the progression of zymosan uptake by AMs during *ex vivo* treatment with Texas Red-conjugated zymosan bioparticles. We counted the number of internalized bioparticles at 0, 20, 60, and 120 minutes post-treatment.

The results indicated a decrease in the average number of internalized zymosan bioparticles in *Egr2*$^{fl/fl}$ AMs compared to the control at 20 minutes and even at 120 minutes. The phagocytic capacity of *Egr2*$^{fl/fl}$ AMs did not reach that of WT AMs, the KO cells internalized fewer zymosan particles (Figure 36).

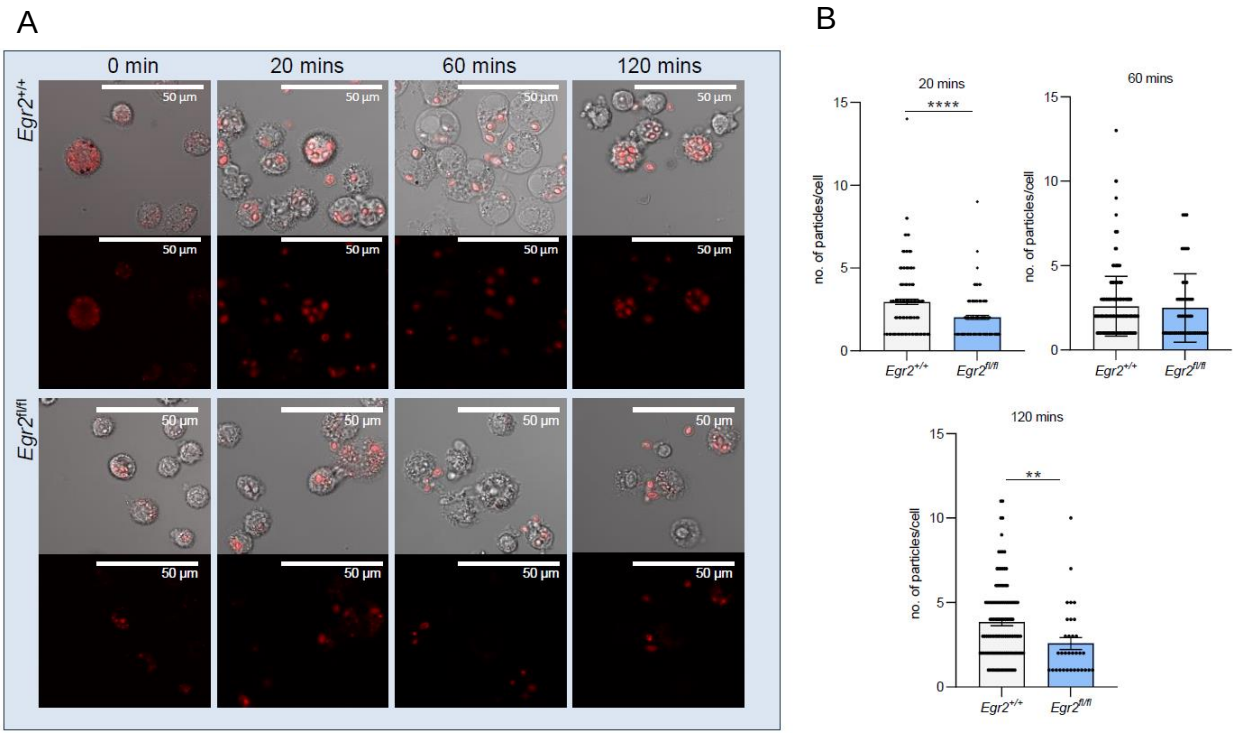

Figure 36. Microscopic examination of zymosan uptake. (A) Confocal microscopy images of *Egr2*$^{+/+}$ or *Egr2*$^{fl/fl}$ AMs at 0, 20, 60, and 120 minutes following treatment with Texas Red-conjugated zymosan (1x10^{6}). **(B)** The number of internalized Texas Red-conjugated zymosan bioparticles per *Egr2*$^{+/+}$ or *Egr2*$^{fl/fl}$ AM at 20, 60, and 120 minutes, as calculated from confocal microscopy images.

We measured the efficiancy of Fc-receptor-mediated phagocytosis of WT and KO AMs using E.coli bioparticles conjugated with pHrodo dye. The cells were able to phagocytose the particles after 3 hours. A relativle small but significant reduction was observable in *Egr2*$^{fl/fl}$ samples compare to the WT cells. However, the absence of EGR2 does not impact the uptake of Staphylococcus aureus bioparticles after 3 hours, nor does it affect dextran macropinocytosis, as determined by pHrodo-conjugated assays (Figure 37).

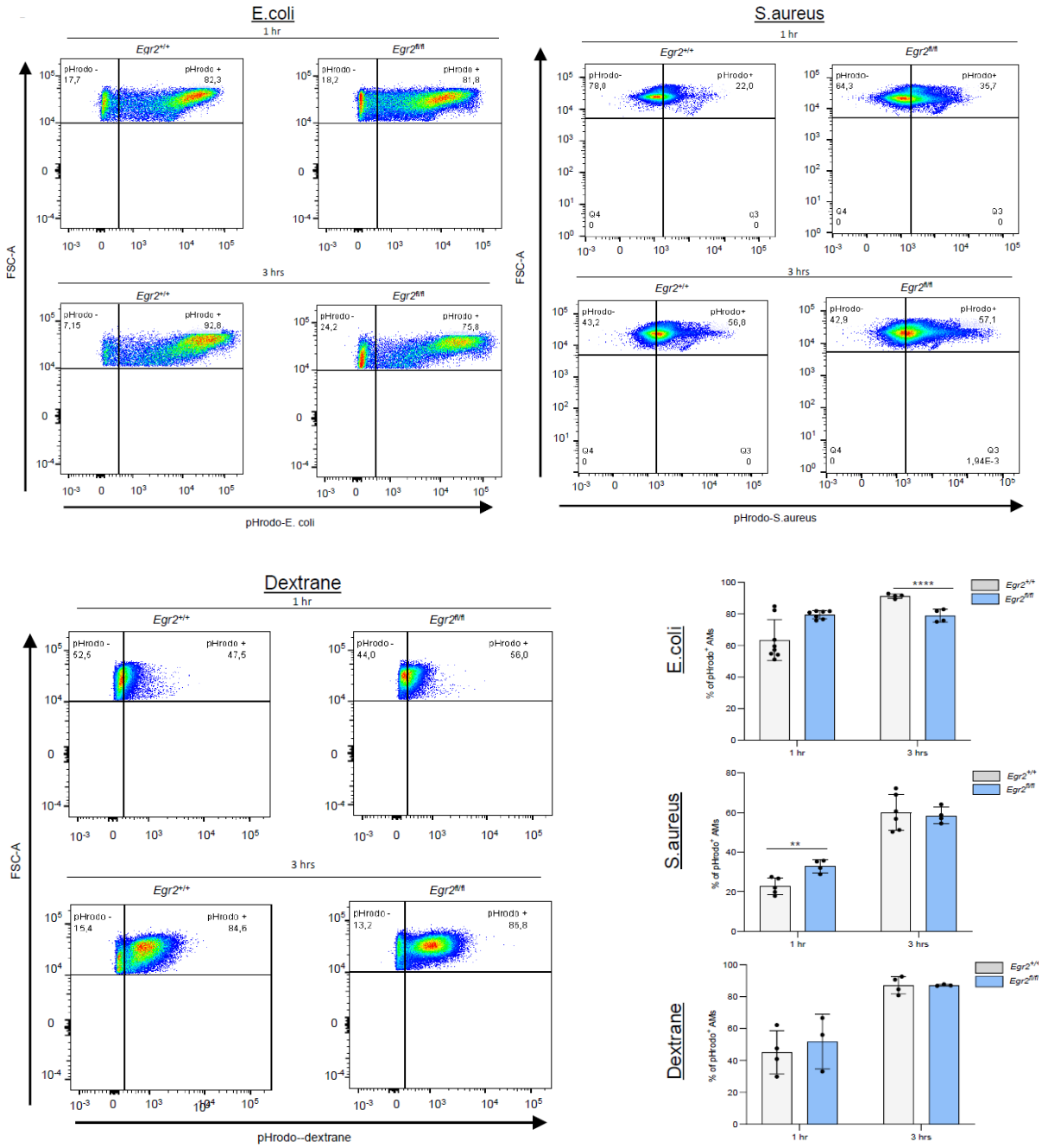

Figure 37. Analysis of E.coli, S. aureus and dextrane uptake *ex vivo*. Representative pseudocolor dot plots of CD45+ and F4/80+ *Egr2*$^{+/+}$ and *Egr2*$^{fl/fl}$ AMs following 1-hour or 3-hour treatment with pHrodo Red-conjugated E. coli, S. aureus, or dextrane using flow cytometry. Bar graphs display the (mean±SEM) percentages of non-phagocytotic (pHrodo-) and phagocytotic (pHrodo+) AMs after 1 hour and 3 hours treatments with pHrodo Red-conjugated E. coli, S. aureus, or dextran in *Egr2*$^{+/+}$ (n=4) and *Egr2*$^{fl/fl}$ (n=3) AMs, as measured by flow cytometry.

Thus, the deficiency of EGR2 results in reduced phagocytic activity and internalization capacity in AMs, particularly when stimulated with zymosan. While the Fc-receptor-mediated

pathway is affected, the Scavenger-receptor-mediated phagocytosis and macropinocytosis remain unaffected.

EGR2 affects the initial transcriptional response to zymosan *in situ* and results in impaired inflammation resolution

Zymosan, which is not only phagocytosed but also triggers a strong inflammatory response, prompted us to further investigate the early phase of the zymosan-induced inflammatory response *in vivo* in *Egr2*$^{+/+}$ and *Egr2*$^{fl/fl}$ mice. We administered 300 µg of zymosan intranasally and analyzed the induced changes at 6 and 24 hours post-administration. This brief timeline was chosen to ensure that the response measured was primarily from AMs, without significant infiltration of circulating monocyte-derived cells into the lungs. We sorted the CD45 positive and F4/80 positive AM populations from control and zymosan-treated groups. Using bulk RNA-seq from four biological replicates, we identified zymosan-responsive and unresponsive gene sets in *Egr2*$^{+/+}$ versus *Egr2*$^{fl/fl}$ AMs, discovering 1755 genes in *Egr2*$^{fl/fl}$ AMs that responded to zymosan compared to controls (Figure 38).

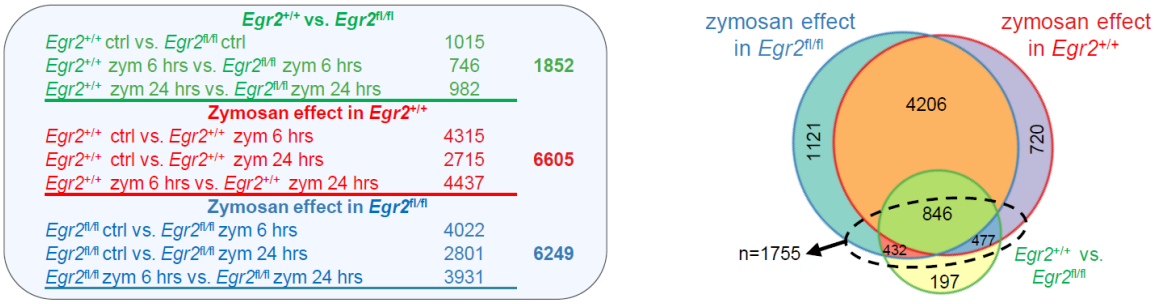

Figure 38. The absence of EGR2 partially and selectively hinders the inflammatory response induced by zymosan. The table lists the number of DEGs identified by RNA-seq: the effect of EGR2 deletion at each time point (green), the effect of zymosan treatment in *Egr2*$^{+/+}$ (red), and in *Egr2*$^{fl/fl}$ (blue). The total values on the right show the number of unique genes that changed in each comparison. The Venn diagram illustrates the overlaps among the gene sets. 1,755 highlighted: the subset responsive to both EGR2 deletion and zymosan treatment.

This EGR2-dependent, zymosan-responsive gene set accounted for about 22.5% (n=1755) of all zymosan-responsive genes. Notably, the majority of EGR2-independent zymosan-responsive genes (n=6047) which showed dynamic expression changes unaffected by the absence of EGR2. This indicates that EGR2 is not essential for inflammatory gene expression in general but plays a distinct and selective role in the early regulation of in situ inflammatory genes.

The 1755 EGR2-dependent and zymosan-responsive genes were organized into ten clusters according to their similar time-dependent expression patterns (Figure 39). These were then reintegrated with the previously identified closed DARs (n=1906) across the ten EGR2-dependent and zymosan-responsive gene clusters.

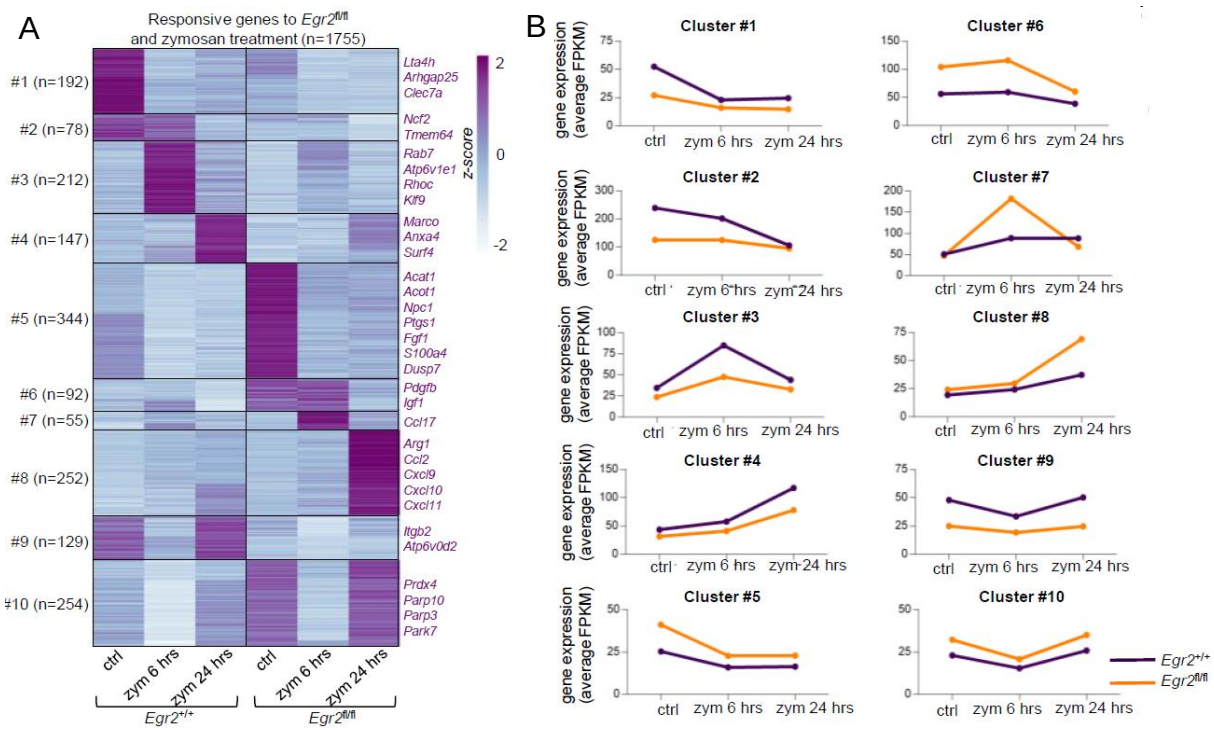

Figure 39. Clusters of zymosan responsive and EGR2 dependent genes in AMs. (A) K-means clustered, row-normalized heatmap displays the average gene expression of 1755 genes across 3 replicates each of control and 6- and 24 hours zymosan treatments in *Egr2*$^{+/+}$ and *Egr2*$^{fl/fl}$ AMs. Representative genes for each cluster are listed on the right. **(B)** Line plots show the average gene expression values for the cluster genes depicted in panel A.

Using the gene TSS extension as defined previously, clusters 1 and 3 were found to be associated with the highest number of EGR motif-containing closing DARs. This association suggests that the inflammatory regulation of these genes might be directly influenced by EGR2.

Moreover, cluster 3 consists of genes that have the same basal expression and early induction. We identified zymosan-responsive and EGR2-dependent repressed DEGs and linked these genes to closed DARs located more than 100 kbp from the TSS of DEGs under control conditions between *Egr2*$^{+/+}$ and *Egr2*$^{fl/fl}$ AMs (Figure 40).

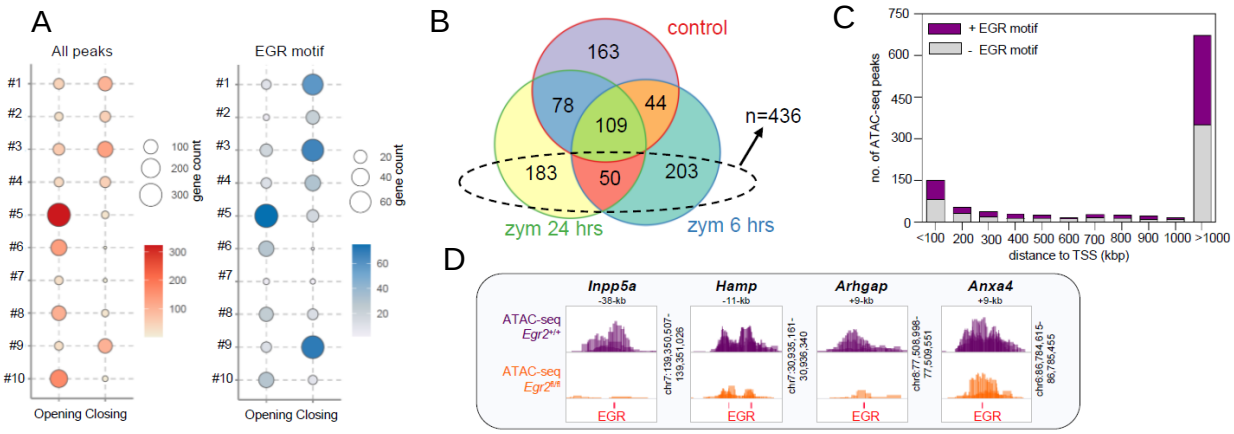

Figure 40. The absence of EGR2 influences certain gene sets that are primarily regulated by zymosan stimulation. (A) Proportional dot plots display the number of associated opening and closing DARs within the ±100 kbp region of gene TSSs or up to the nearest gene(s) (left, highlighted in red), and the number of EGR motifs within these ATAC-seq peaks (right, highlighted in blue) for each of the 10 gene clusters shown in Figure 39. **(B)** The Venn diagram illustrates the overlap of significantly repressed genes between *Egr2*$^{+/+}$ and *Egr2*$^{fl/fl}$ AMs under control conditions or after 6- or 24 hours zymosan (300 µg) treatment. The highlighted 436 genes constitute a zymosan-dependent repressed gene set. **(C)** The bar chart depicts the distance distribution of EGR motif–containing (purple) or non-containing (gray) closing DARs (n = 1075, located more than 1000 kbp from repressed genes) in relation to the TSS position of the repressed zymosan-dependent DEGs (n = 436). **(D)** IGV snapshots display the ATAC-seq coverages of *Egr2*$^{+/+}$ and *Egr2*$^{fl/fl}$ AM samples in control conditions and the presence of EGR motif(s) related to 4 selected genes (overlaid).

The expression of these genes (e.g., *Inpp5a*, *Hamp*, *Arhgap10*, and *Anxa4*) was significantly affected by EGR2 during zymosan-induced inflammation, but not under unstimulated, physiological conditions. As a representative example, we validated the mRNA expression profile of the *Arhgap10* gene *ex vivo* and measured the eRNA level of an associated DAR using RT-qPCR after 6- and 24 hours zymosan treatments. We observed a significant decrease in eRNA levels at the 6-hour mark and in both cases following the 24-hour treatment in the $Egr2^{fl/fl}$ condition (Figure 41).

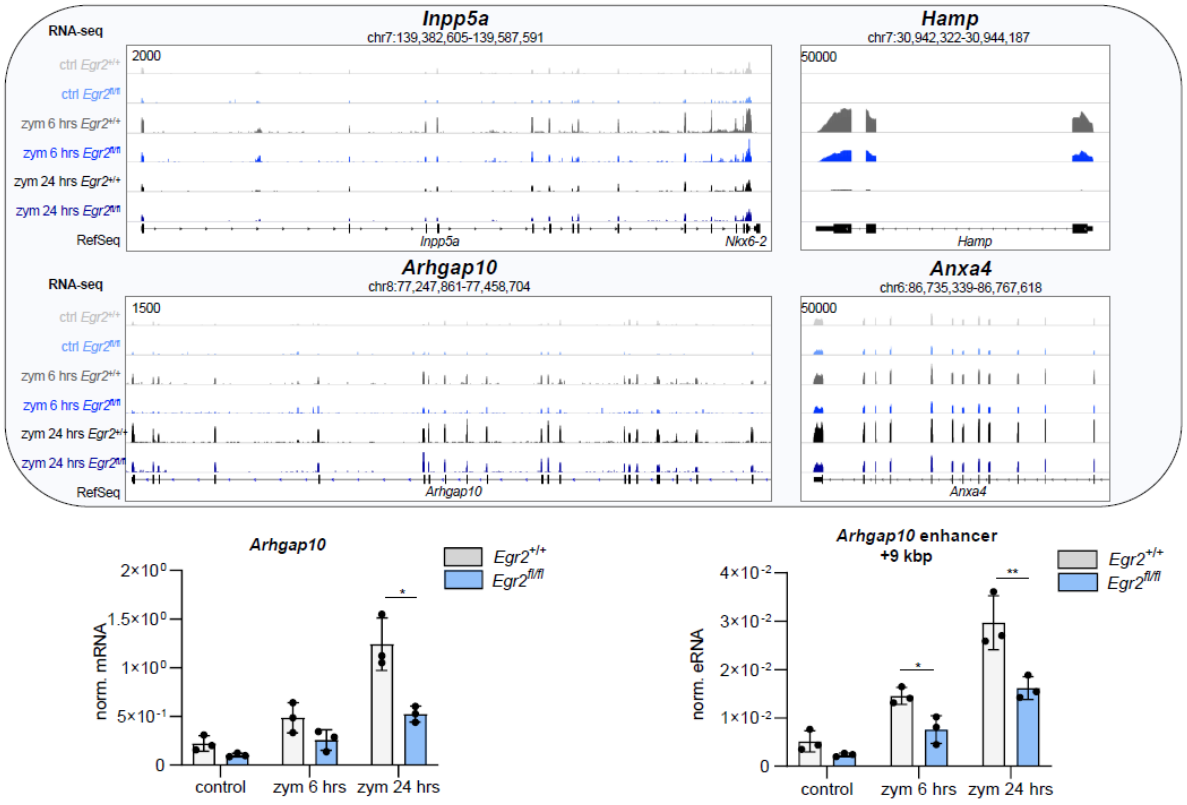

Figure 41. The mRNA expression pattern of selected zymosan responsive and EGR2 bookmarked genes. The IGV snapshots display RNA-seq coverages for selected representative genes in control, in 6 hours and 24 hours zymosan-treated (300 µg) $Egr2^{+/+}$ and $Egr2^{fl/fl}$ AMs (overlaid). Bar graphs illustrate the (mean±SEM) values of normalized mRNA levels for the *Arhgap10* gene and eRNA for the *Arhgap10*-related region in control and *ex vivo* 6- and 24 hours zymosan-treated (300 µg) $Egr2^{+/+}$ and $Egr2^{fl/fl}$ AMs.

This observation indicates that EGR2 plays a dual role in shaping the AM epigenome and modifies various signal-dependent transcriptional responses without affecting the gene's

basal expression. Thus, it functions as an epigenomic bookmarker. Functionally, the EGR2-dependent genes responsive to zymosan were linked to phagocytosis-related signaling pathways and ones important in response to microbial infections (Figure 42).

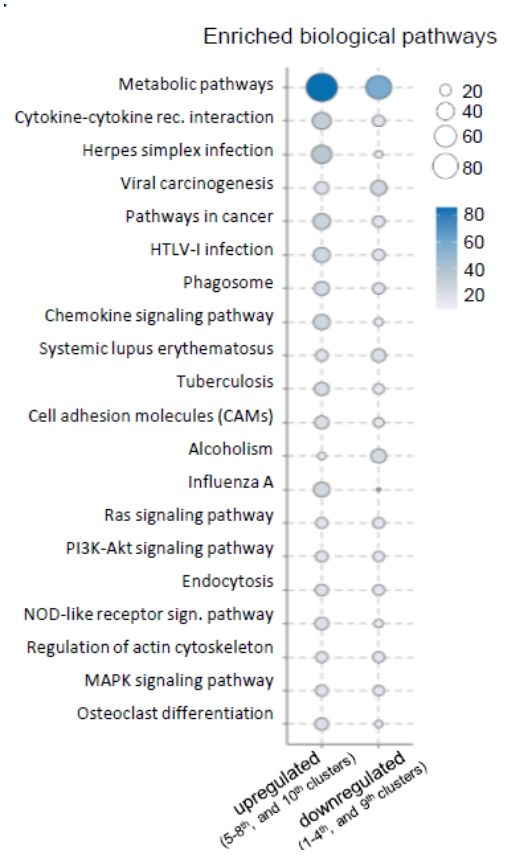

Figure 42. The main pathways affected by EGR2 during zymosan treatment. The dot plot illustrates the top 20 KEGG biological pathways associated with 1755 zymosan responsive and EGR2 dependent genes, selected and ranked according to the total number of target genes within each pathway.

The Integrative Genomic Viewer (IGV) visualization of the expression profiles for phagocytosis-related genes *Rilpl2*, *Cybb*, and *Atp6v1e1*, along with the induction of inflammatory markers *Arg1*, *Nos2*, *Pf4*, and *Cxcl9*, illustrates the significant impact EGR2 has on regulating these processes (Figure 43).

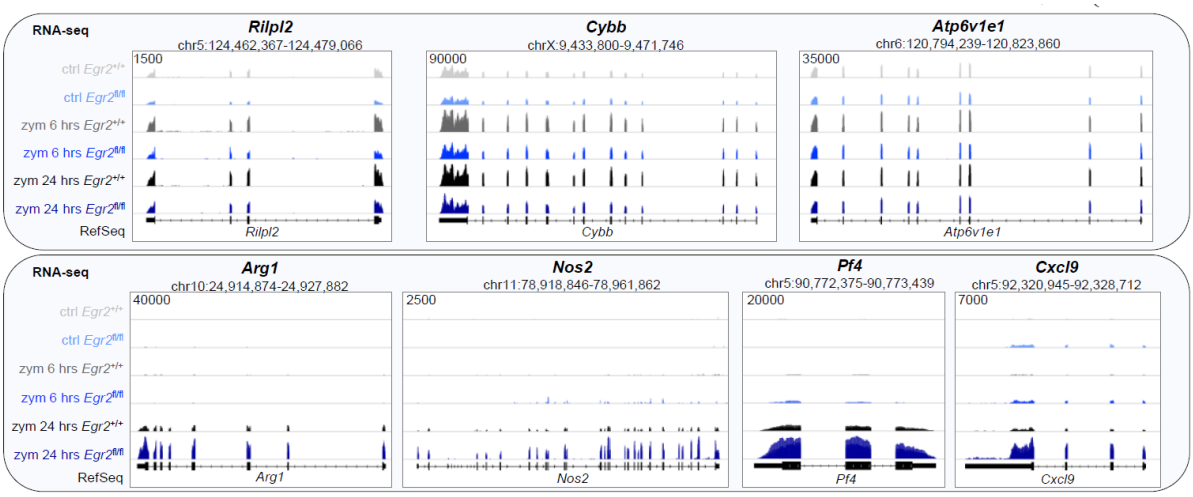

Figure 43. The expression pattern of phagocytosis- and inflammation-related representative genes during zymosan treatment. IGV visualization displays the RNA-seq coverages for *Egr2*$^{+/+}$ and *Egr2*$^{fl/fl}$ samples under control conditions and following 6- and 24 hours zymosan treatment (300 µg) for selected phagocytosis- (*Rilpl2, Cybb, Atp6v1e1*) and inflammation-related genes (*Arg1, Nos2, Pf4, Cxcl9*) (overlaid).

We analyzed KEGG gene sets for TLR, TGF-β, Jak-Stat, phosphatidyl-inositol (PI), and ARA signaling pathways to pinpoint exact EGR2-dependent changes linked to the canonical inflammatory response. While all pathways included DEGs, the impacted genes exhibited varying ratios and expression patterns across the groups (Figure 44). Genes primarily upregulated were associated with the TGF-β, TLR, and Jak-Stat pathways. These changes affected numerous cytokines (*Cxcl11, Cxcl9, Cxcl10*), receptors (e.g., *Tlr8, Tlr7, Tlr9, Csf3r*), and transcription factors (e.g., *Stat1, Stat2,* and *Irf9*). The DEGs tied to the PI signaling pathway were notably repressed, including genes coding for components of phosphorylation cascades. Additionally, we identified *Lta4h* as a proximal, likely direct target, which was consistently repressed following zymosan treatment in EGR2-null AMs.

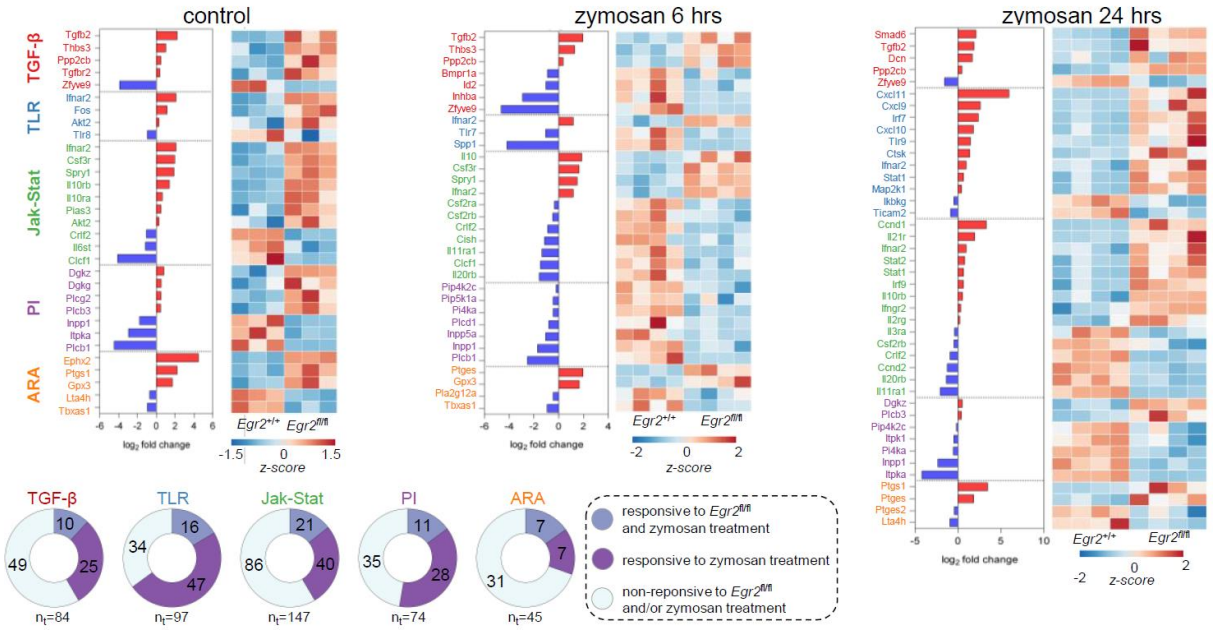

Figure 44. The different inflammatory signaling pathways influenced by zymosan in EGR2 KO AMs. The bar charts and heatmaps illustrate the DEGs between *Egr2*$^{+/+}$ and *Egr2*$^{fl/fl}$ AMs both under control conditions and after 6- and 24 hours zymosan treatments (300 µg). Depicted are specific signaling pathways: TGF-β, TLR, JAK/STAT, PI, and ARA. The bar charts provide the fold-difference in average gene expression values, while the heatmaps display the row-normalized expression patterns of the shown genes. Pie charts indicate the number of genes from the selected pathways that remain unchanged or change significantly ($p \leq 0.05$) under different treatment conditions in *Egr2*$^{+/+}$ and *Egr2*$^{fl/fl}$ AMs (RNA-seq).

Given that transcriptional changes significantly impacted genes encoding cytokines and lipid mediator-synthesizing enzymes, we measured the cytokine profile using an ELISA-based array from BAL fluid and ARA metabolism-related lipid mediators via mass spectrometry from total lung homogenate. These methods revealed a notable decrease in IL-4 protein levels 6 hours after zymosan treatment and an increase in the levels of C-C Motif Chemokine Ligand 17 (CCL17), CXCL11, and Colony Stimulating Factor 1 (CSF1) after 24 hours of treatment (Figure 45 A). The induction of CXCL11 is particularly noteworthy as this cytokine is not induced when EGR2 is present (Figure 45 B, C), indicating a novel and highly specific response. Among ARA-derived lipid mediators, RvE1 was undetectable in the lungs of EGR2-deficient mice (Figure 45 C). This lipid mediator, produced by the Leukotriene A4 Hydrolase

(LTA4H) enzyme, plays a crucial role in resolving inflammation. Although *Lta4h* expression is reduced in zymosan-treated EGR2-null AMs (Figure 45 B).

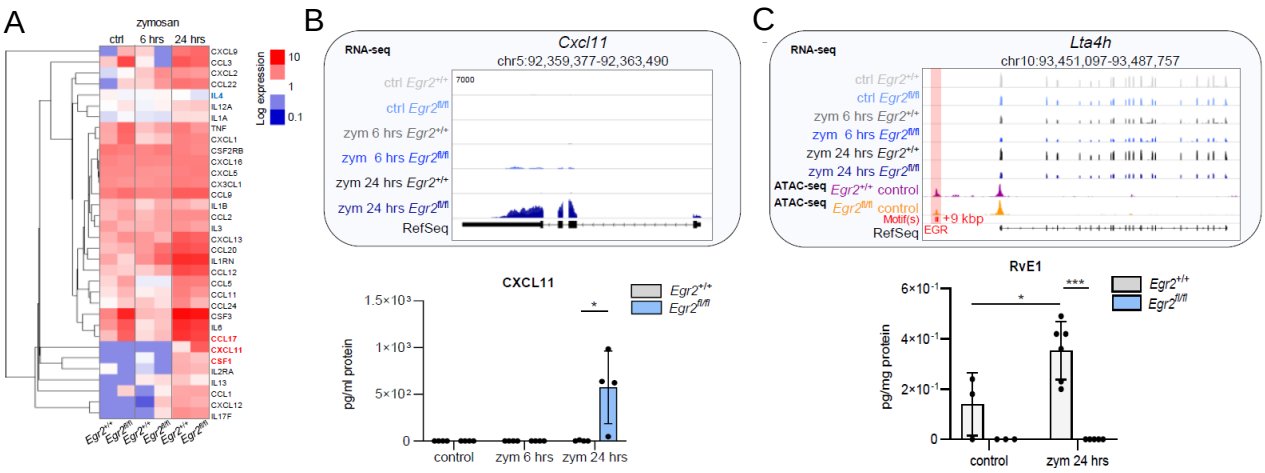

Figure 45. (A) The average protein content of BAL fluid from control, 6-, and 24 hours zymosan-treated (300 µg) samples, determined using a cytokine array (n = 4 per treatment condition, 1-way ANOVA test with Tukey's post hoc test, $P \leq 0.05$). (B) IGV visualization shows RNA- and ATAC-seq coverages for *Egr2*$^{+/+}$ and *Egr2*$^{fl/fl}$ AMs along with the presence of EGR motifs on the *Lta4h* gene. (C) CXCL11 protein levels in BALF under various treatment conditions measured by cytokine array and the quantity of RvE1 in the total lung homogenate of *Egr2*$^{+/+}$ (n = 3) and *Egr2*$^{fl/fl}$ (n = 6) mice, analyzed by liquid chromatography-tandem mass spectrometry (LC-MS/MS).

It seems that EGR2 acts as a specific and selective regulator of a distinct subset of immune effector mechanisms in AMs. We further examined the inflammatory process by analyzing the histology of paraffin-embedded, H&E-stained lung samples after 24 and 72 hours of zymosan treatment. Comparable infiltration of PMNs was observed in both WT and *Egr2*$^{fl/fl}$ mice 24 hours after zymosan exposure, although *Egr2*$^{fl/fl}$ lungs showed a greater presence of macrophage-like mononuclear cells with large, irregular nuclei. Additionally, after 72 hours, the alveoli in the lungs of *Egr2*$^{fl/fl}$ mice remained unresolved, and there was a progression towards tissue remodeling and incipient fibrosis (Figure 46).

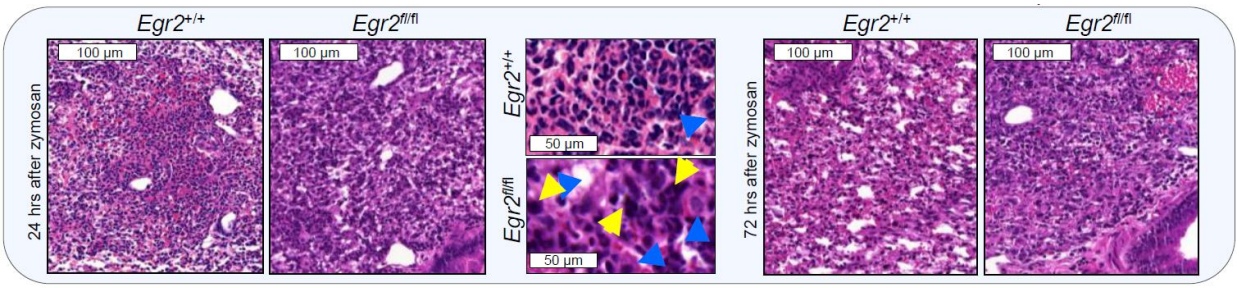

Figure 46. The histological analysis of zymosan-treated lungs. Representative H&E-stained, paraffin-embedded lung sections from *Egr2*$^{+/+}$ and *Egr2*$^{fl/fl}$ mice 24 and 72 hours following *in vivo* zymosan treatment (300 µg) at high magnification (original magnification, 630×). In *Egr2*$^{+/+}$ lungs, typical acute purulent inflammation is evident 24 hours after zymosan administration, characterized by numerous PMNs. In contrast, *Egr2*$^{fl/fl}$ lungs, containing EGR2-deficient AMs, show inflammatory infiltrates with increased numbers of large macrophages (blue arrows) and occasionally large, abnormal-appearing, chromatin-rich nuclei (yellow arrows).

These results indicate that EGR2 selectively influences the initial *in situ* transcriptional mechanism of the zymosan-induced inflammatory response. The absence of this transcription factor results in an unresolved inflammatory phenotype *in vivo* through both direct and indirect mechanisms.

Inadequate response to *Aspergillus fumigatus* in AMs lacking EGR2

Finally, we expanded our research to include pathophysiologically relevant *ex vivo* and *in vivo* fungal infection models. To compare how control and *Egr2*$^{fl/fl}$ AMs interact with fungal pathogens, we utilized *ex vivo* and *in vivo* infection models of *Aspergillus fumigatus*. Initially, we treated *Egr2*$^{+/+}$ and *Egr2*$^{fl/fl}$ AMs, isolated from BAL, with *AF* conidia for 1 hour, allowing the AMs to internalize the particles. At that point, and after an additional 6 hours of incubation, we lysed the cell cultures and measured the samples' colony forming capacity (Figure 47 A). We observed a significant decrease in CFUs after 1 hour which indicates the reduced capacity of phagocytosis, and a significant increase at 7 hours which marks the impared intracellular fungal inactivation and killing in EGR2-null AMs (Figure 47 B). Furthermore, the ratio of

internalized and inactivated *AF* conidia was lower in *Egr2*$^{fl/fl}$ AMs. Using time-lapse microscopy, we monitored the morphological changes following the internalization of *AF* conidia (Figure 47 C). We found that EGR2 deficiency in AMs resulted in a greater proportion of hyphae-containing AMs and an earlier onset of hyphae growth compared to WT cells (Figure 47 D).

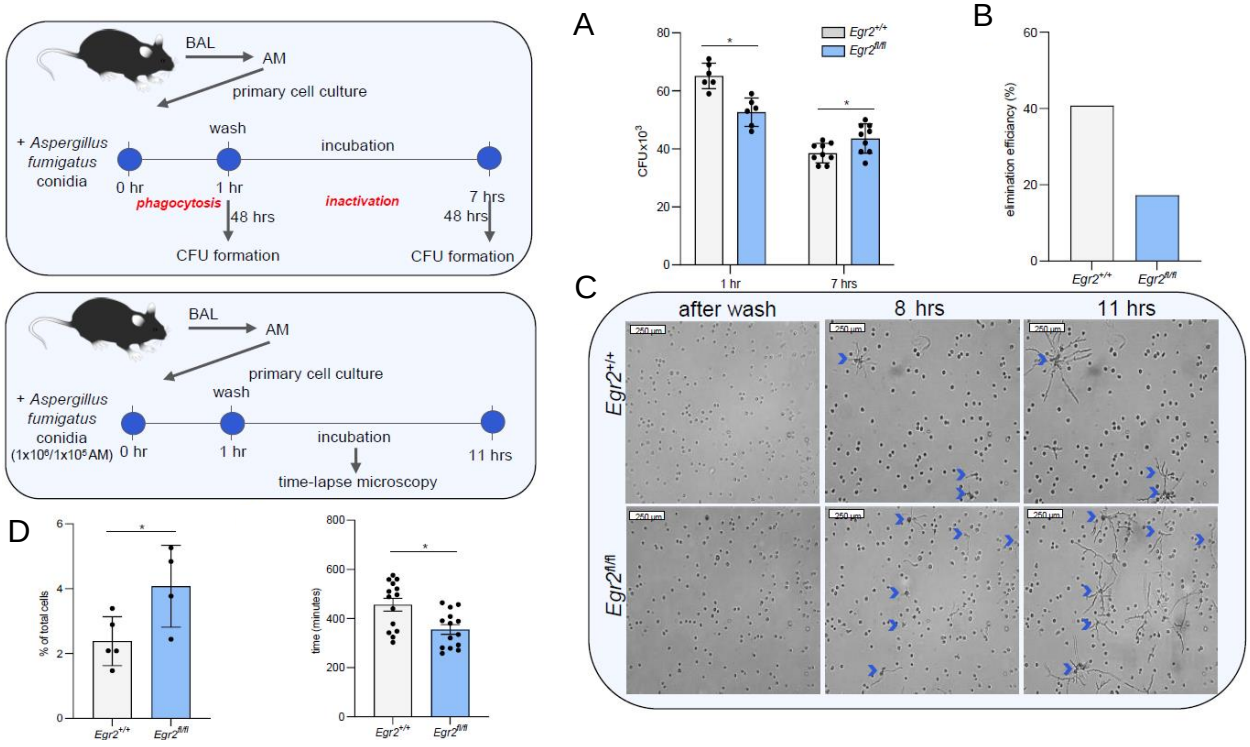

Figure 47. *Ex vivo* examination of EGR2-mediates antifungal effect of AMs. (A) An overview of the experimental setup for evaluating the elimination efficiency of AMs *ex vivo* using colony formation assay and time-lapse microscopy. (B) Bar graphs depict the (mean±SEM) count of *AF* colonies following 1 hour and 7 hours of cotreatment with *Egr2*$^{+/+}$ (n_{1hr} = 6, n_{3hrs} = 9) and *Egr2*$^{fl/fl}$ (n_{1hr} = 6, n_{3hrs} = 9) AMs and the elimination percentage of *AF* conidia is determined from the average colony-forming capacity following the uptake and elimination period. (C) Representative images from time-lapse microscopy show *AF* conidia after being washed from *Egr2*$^{+/+}$ and *Egr2*$^{fl/fl}$ AM coculture at 8 and 11 hours (blue arrows: hypha-containing AMs). (D) The (mean ± SEM) of hypha-containing AMs after 11 hours in *Egr2*$^{+/+}$ and *Egr2*$^{fl/fl}$ cells and the (mean± SEM) timing of the onset of hypha growth in *Egr2*$^{+/+}$ (n=14) and *Egr2*$^{fl/fl}$ (n=14) AMs, assessed via time-lapse microscopic imagery.

We also investigated the *in vivo* effects of *AF* conidia through intranasal infection. We monitored changes in body mass, colony forming capacity, viabale hypha containing AM counting and conducted histological analysis of the lungs. Clinically, no significant differences were observed in WT mice under the test conditions following infection. However, *Egr2*$^{fl/fl}$ mice quickly began to lose body weight (Figure 48 A). The most pronounced differences compared to control animals were observed on the 5th and 6th days of infection.

To assess the pulmonary fungal burden, particularly during the period dominated by the innate immune response, we collected BAL from both *Egr2*$^{+/+}$ and *Egr2*$^{fl/fl}$ lungs. CD45+ cells were then plated in cell culture dishes, and changes were monitored using time-lapse microscopy. This approach revealed a higher proportion of hypha-containing AMs in *Egr2*$^{fl/fl}$ lungs compared to the WT. Additionally, after a two-day *AF* infection, the *Egr2*$^{fl/fl}$ lung homogenates exhibited significantly greater colony formation capacity than those from *Egr2*$^{+/+}$ mice, highlighting the crucial role of myeloid EGR2 in the antifungal response *in vivo* (Figure 48 B).

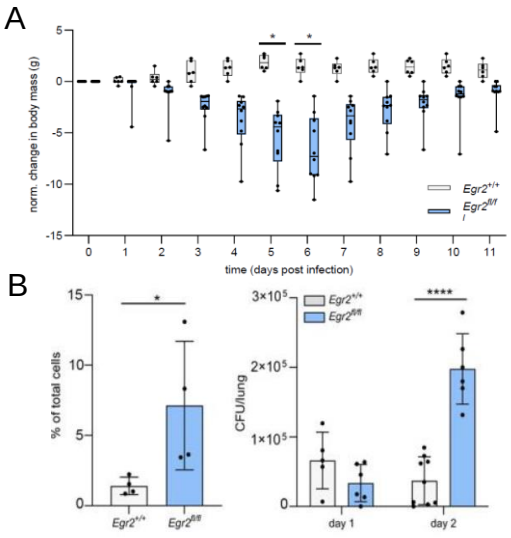

Figure 48. Reduced clearance of *AF* in mice lacking EGR2 in myeloid cells. (A) Variation in body mass for *Egr2*$^{+/+}$ (n = 6) and *Egr2*$^{fl/fl}$ (n = 9) mice after *AF* infection, normalized to the average untreated body mass. **(B)** The (mean±SEM) percentage of hypha-containing *Egr2*$^{+/+}$ and *Egr2*$^{fl/fl}$ AMs after 24 hours *AF* infection, based on time-lapse microscopy and the bar plots on right showing the (mean±SEM) number of *AF* colonies following 1- and 2 days *AF* infection in *Egr2*$^{+/+}$ (n_{day1}=5, n_{day2}=9) and *Egr2*$^{fl/fl}$ (n_{day1}=6, n_{day2}=6) lungs.

Histological analyses indicated a trend of unresolved, prolonged inflammation with early onset of progressive pulmonary fibrosis in lung tissue samples specifically deficient in myeloid EGR2 by day 5 following *AF* inoculation; this was corroborated by Masson's trichrome staining. In contrast, the lungs with normal WT AMs ($Egr2^{+/+}$) demonstrated regressing inflammation by day 5, showing partial alveolar resolution without fibrosis (Figure 49).

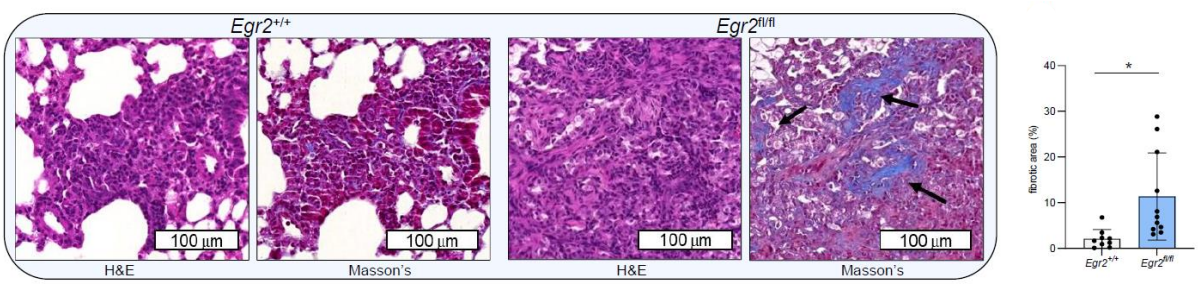

Figure 49. The myeloid specific EGR2 deficiency leads enhanced pulmonary fibrosis in *AF* infection. Representative paraffin-embedded images (H&E-stained and Masson's trichrome-stained) of WT and EGR2 KO lungs following a 5 days of *AF* infection (arrows mark fibrotic areas). The bar graph shows the Fibrotic area percentage (mean ± SEM) in inflamed fields derived from Masson's trichrome-stained lungs of $Egr2^{+/+}$ (n=9) and $Egr2^{fl/fl}$ (n=11) mice 5 days post-infection.

AF is an opportunistic pathogen, and severe or fatal *AF* infections occur only in immunocompromised patients. Thus, cyclophosphamide (CP)-induced immunosuppression serves as an appropriate model, leading to rapid *aspergilloma* formation in the lungs. We employed this agent in combination with gentamycin bacterial prophylaxis to evaluate the effects of myeloid-specific EGR2 loss under immunosuppressive conditions. Initially, we used flow cytometry to assess changes in the number of various immune cells (AMs, monocytes, PMNs, B cells, CD4+, and CD8+ T cells) in the lung after 1 day of infection. CP treatment resulted in a significant decrease in the number of B and CD4+ T cells and a slight, though not significant, reduction in AMs and CD8+ T cells in the lungs of both WT and EGR2-deficient

mice compared to non-immunocompromised infections. The reduction in monocyte and neutrophil numbers was noticeable only in control animals (Figure 50).

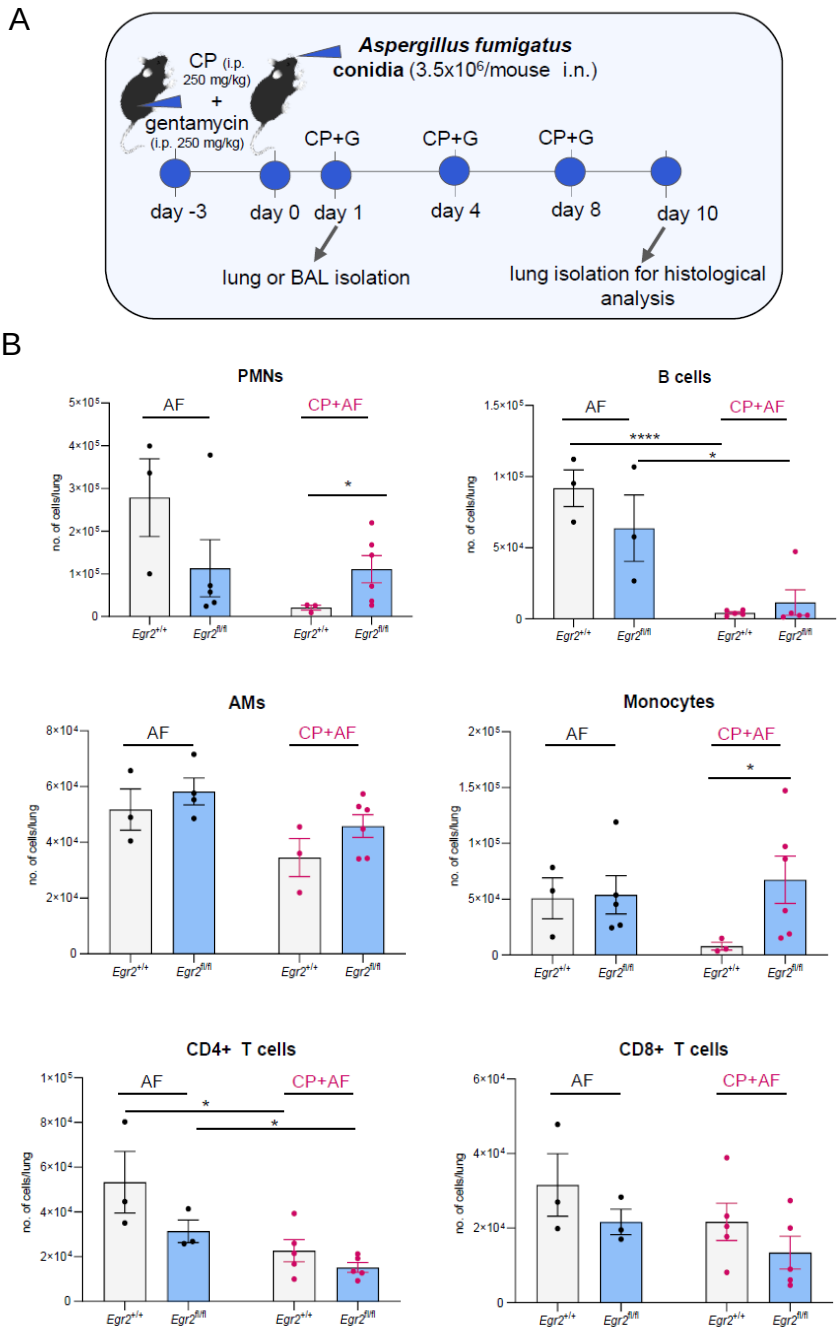

Figure 50. Comparison of cellular changes during *in vivo Aspergillus fumigatus* lung infection with or without cyclophosphamide-induced immunosuppression. (A) Schematic overview of the *in vivo* cyclophosphamide (CP) immunosuppression and *AF* infection in a pneumonia model. **(B)** The count of various immune cell types isolated from total lung samples of 24-hour *AF*-infected *Egr2*$^{+/+}$ (n=3) and *Egr2*$^{fl/fl}$ (n=3 or n=5) mice, with or without prior CP treatment.

Next examined the BALF isolated from the lungs one day after *AF* infection. Using the BCA method, we did not observe any significant changes in total protein levels across different conditions (Figure 51 A). However, under immunosuppression, we found significantly higher LDH activity (Figure 51 B) and a tendency for increased concentrations of inflammatory cytokines (TNFα, IL-6) and profibrotic markers (CXCL9, CXCL11, CXCL13) in *Egr2*$^{fl/fl}$ mice compared to controls, as measured by ELISA (Figure 51 C).

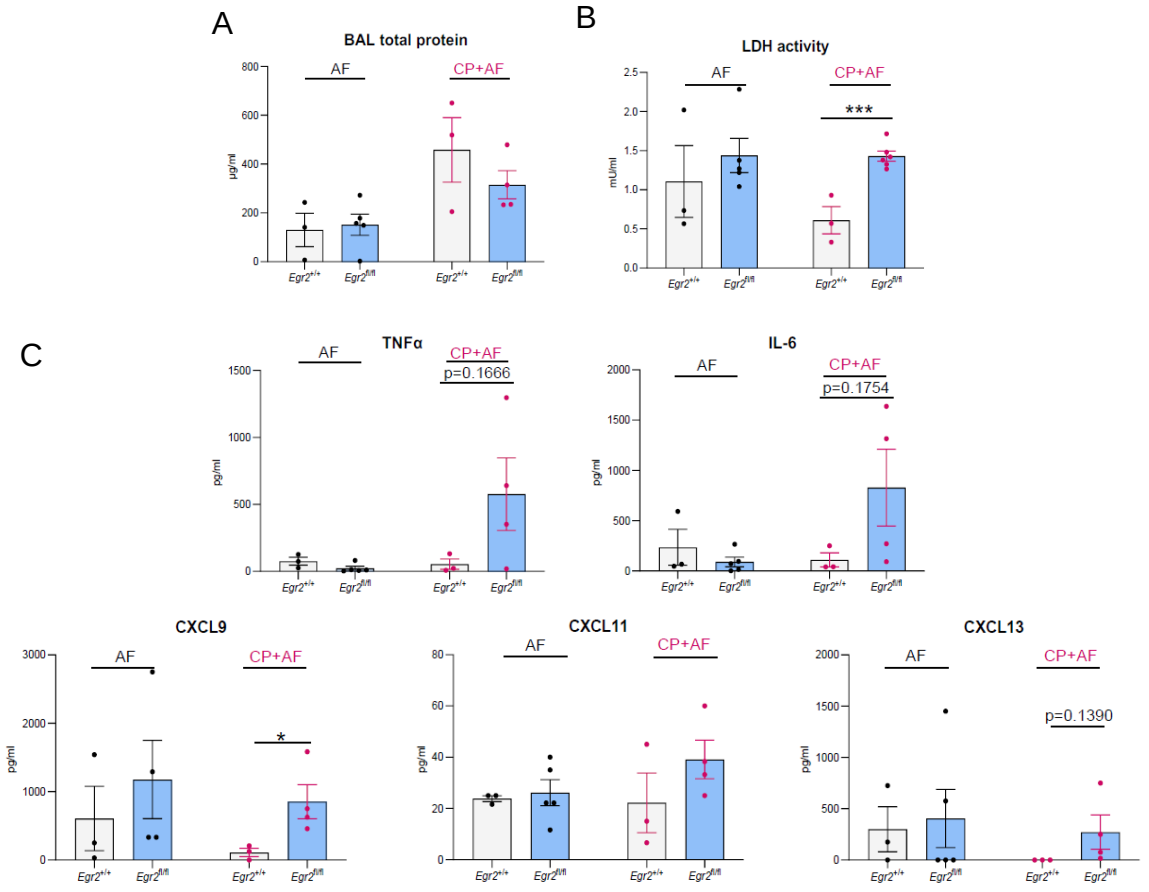

Figure 51. Comparison of molecular changes during *in vivo Aspergillus fumigatus* lung infection with or without cyclophosphamide-induced immunosuppression. Bar graphs showing the total protein levels in BALF, determined by BCA assay **(A)** and the LDH activity **(B)** in BALF following 24 hours of *AF* infection, with or without CP-induced immunosuppression from *Egr2*$^{+/+}$ (n=3) and *Egr2*$^{fl/fl}$ (n=5 or n=4) mice. **(C)** Quantities of inflammatory marker proteins (TNFα and IL-6) and fibrotic marker cytokines (CXCL9, CXCL11, CXCL13) in BALF collected after 24 hours of AF infection from both AF-infected and CP-pretreated, AF-infected *Egr2*$^{+/+}$ (n=3) and *Egr2*$^{fl/fl}$ (n=5 or n=4) mice, measured by ELISA assays.

During the infection, both control and *Egr2*$^{fl/fl}$ mice showed similar survival rates (Figure 52 A), although *Egr2*$^{fl/fl}$ mice experienced significantly greater weight loss by day 10 post-infection (Figure 52 B).

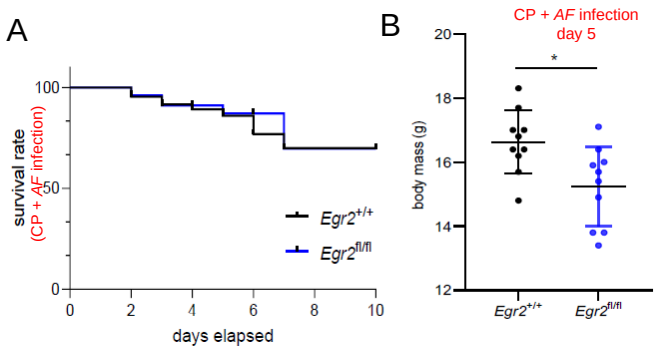

Figure 52. Survival analysis during cyclophosphamide-induced immunosuppression and *Aspergillus fumigatus* infection. (A) The Kaplan-Meier survival curve illustrates the survival rate of CP-immunosuppressed and AF-infected mice (*Egr2*$^{+/+}$ (n=15) and *Egr2*$^{fl/fl}$ (n=11)). **(B)** The change in body mass of *Egr2*$^{+/+}$ (n=10) and *Egr2*$^{fl/fl}$ (n=10) mice 5 days after *in vivo* intranasal *AF* infection with concurrent CP immunosuppression.

Histological analysis of lung sections from both groups, stained with H&E, PAS, and Grocott's method, revealed significantly larger *aspergillomas* containing *AF* hyphae and necrotizing inflammation characterized predominantly by large macrophage-like mononuclear cells with pleomorphic large nuclei or apoptotic cells in *Egr2*$^{fl/fl}$ mice (Figure 53).

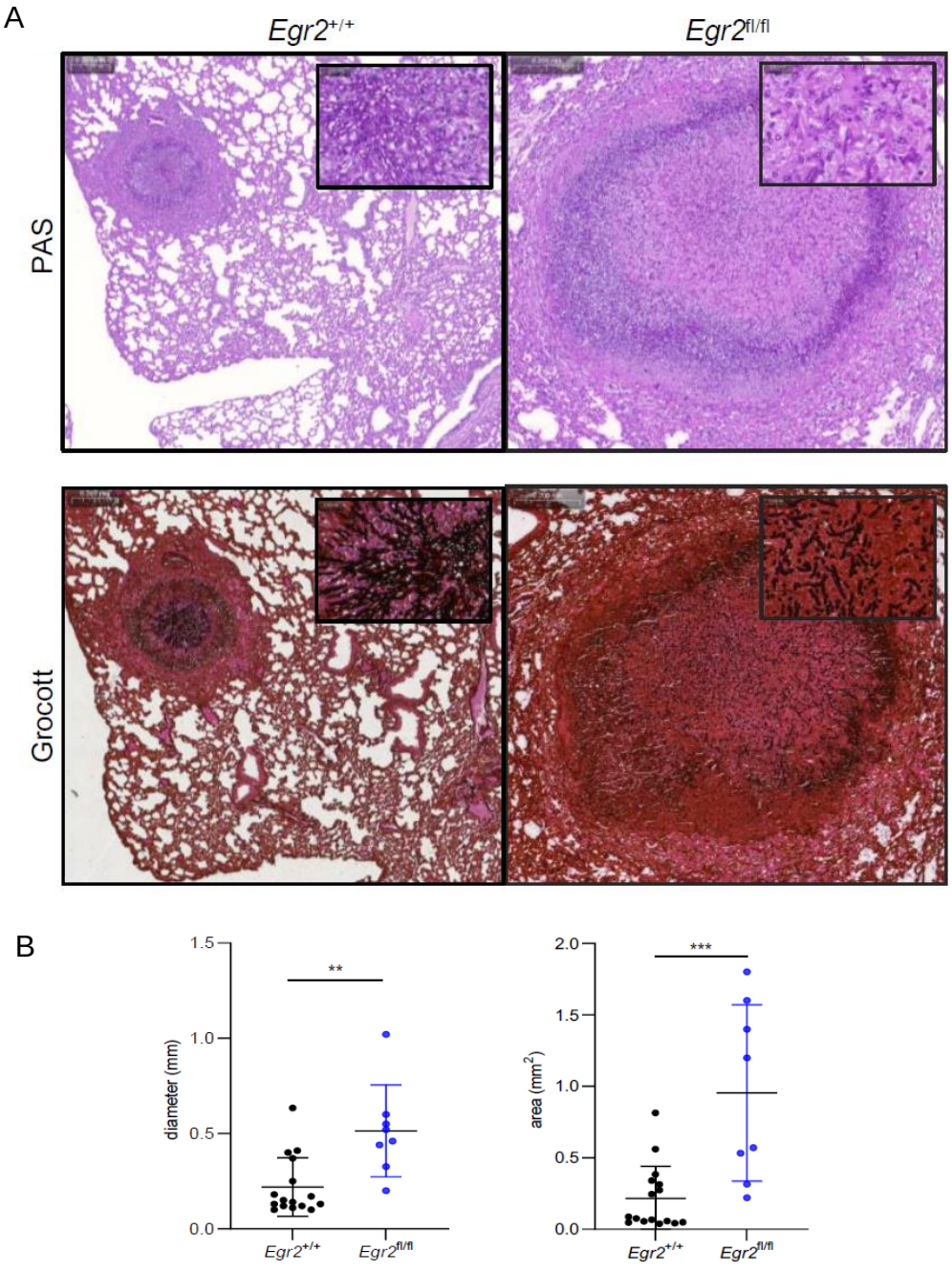

Figure 53. Histological analysis of fungal burdens in *Egr2*$^{fl/fl}$ mice during cyclophosphamide-induced immunosuppression and *Aspergillus fumigatus* infection. (A) Representative images of paraffin-embedded lung samples from *Egr2*$^{+/+}$ and *Egr2*$^{fl/fl}$ mice following CP pretreatment and *AF* exposure via the airway, stained with PAS and Grocott's methenamine-silver. These images reveal pulmonary *aspergillomas* and highlight the presence of fungal elements with magnified insets showcasing details. **(B)** The mean±SEM of *aspergilloma* diameters and areas measured 10 days post-AF infection and CP immunosuppression are shown in representative paraffin-embedded and Grocott-stained sections from *Egr2*$^{+/+}$ (n=6) and *Egr2*$^{fl/fl}$ (n=6) lung samples.

The lungs of *Egr2*$^{fl/fl}$ mice harbored persistent inflammatory cells which induced large spindle-shaped cells, indicative of activated fibroblast morphologies (Figure 53, yellow arrows). Masson's staining of these areas revealed coarse collagen deposits, indicating significant fibrosis (Figure 53, blue fibrillar staining).

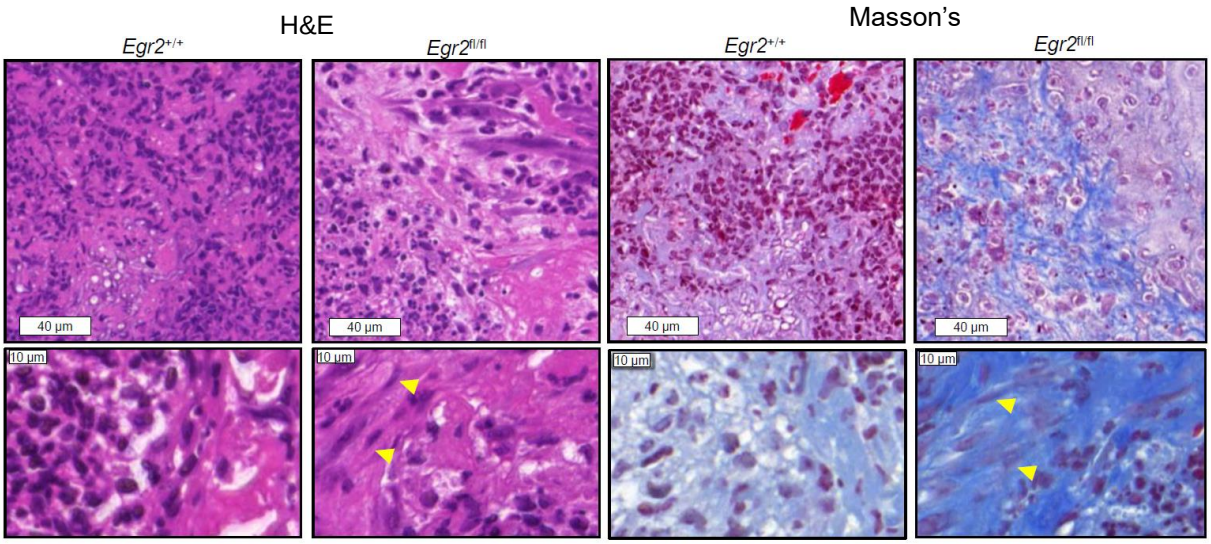

Figure 53. Histological analysis of fibrosis in *Egr2*$^{fl/fl}$ mice during cyclophosphamide-induced immunosuppression and *Aspergillus fumigatus* infection. Representative images of paraffin-embedded, hematoxylin and eosin (H&E), and Masson's trichrome-stained lung sections from CP-immunosuppressed and AF-infected *Egr2*$^{+/+}$ and *Egr2*$^{fl/fl}$ mice after 10 days of infection. In *Egr2*$^{fl/fl}$ samples, persistent inflammatory cells lead to the formation of large spindle cells, indicative of activated fibroblasts (yellow arrows). Masson's trichrome staining of these regions reveals coarse collagen deposits, indicative of significant fibrosis (blue fibrillar staining).

These results collectively offer further *in vivo* evidence of the crucial role EGR2 plays in the antifungal activity of AMs, although it is important to note that the observed findings reflect a complex multicellular phenotype.

VII. Discussion

EGR2 is a late-stage regulator of alternative macrophage polarization

Understanding the hierarchical transcriptional program governing macrophage polarization in both healthy and diseased states is crucial for advancing knowledge of cell type specification and developing targeted therapies. These therapies aim to reprogram macrophages to enhance beneficial phenotypes while minimizing harmful ones. In our study, we identified EGR2, a zinc finger transcription factor, as a key component of the IL-4-mediated and STAT6-dependent alternative polarization program. EGR2 connects early, transient events to later, more stable ones, establishing critical hierarchical relationships among various transcription factors. Acting as a molecular linchpin, EGR2 links the transient STAT6 signal to enduring epigenomic changes, supporting stable gene expression. We leveraged the mapping of genome activity, using active enhancer markers P300 and H3K27ac, over a time course of macrophage polarization to study both the immediate and long-term effects of IL-4-activated STAT6. This strategy led to the description of EGR2, a powerful transcriptional regulator with previously unrecognized functions in myeloid cells. While *Egr2* had been reported as an IL-4-induced gene in macrophages in transcriptome-wide analyses, its specific roles had remained unclear. In our model, *Egr* genes are minimally expressed in unstimulated macrophages. IL-4 selectively induces *Egr2*.

The reanalysis of mouse tissue-resident macrophage RNA-seq data revealed that *Egr2* exhibits a lung-restricted expression pattern in the steady state. Combined with findings about basophil-derived IL-13, the other cytokine responsible for alternative macrophage polarization in addition to IL4, and its importance in AM function (Cohen et al. 2018), the results support EGR2's *in vivo* role. This has prompted further investigations into EGR2's function within lung-resident macrophage subsets.

The function of EGR2 as an auxiliary or secondary LDTF

AM identity is established by general macrophage LDTFs such as PU.1 and C/EBPβ, along with the lipid-regulated nuclear receptor PPARγ, which is essential for AM differentiation. However, EGR2 stands out as a distinctive component due to its specialized function: it directly activates only a limited subset of mature AM marker genes, such as SiglecF, while leaving others unchanged, like *Car4*, *Il1rn*, and *Krt19*. Uniquely, the absence of EGR2 does not lead to a complete blockage of differentiation or widespread functional shortcomings as seen with PU.1 across all macrophage types or with PPARγ in AMs. Our findings support this view; EGR2 deficiency caused only a partial reduction in differentiation-dependent gene expression, with most inflammatory and phagocytic responses remaining intact. Thus, EGR2 acts more as an accessory or secondary LDTF, collaborating with other factors to specify and enhance certain aspects of AM identity and function, rather than serving as a primary determinant.

The dual mechanism of EGR2 action

EGR2 serves multiple roles throughout the body, playing vital parts in embryonic development and hindbrain formation as a positive regulator of r3 and r5 rhombomeres and a repressor of r2 and r4 rhombomeres. More broadly, EGR proteins, including EGR2, are involved in the differentiation of myeloid cells, monocytes, and macrophages, functioning both as transcriptional activators and repressors. However, some claims about their pivotal role in macrophage versus neutrophil differentiation have been challenged by genetic studies showing no significant impact on macrophage differentiation from the deletion of EGR combinations *in vitro* or *in vivo* (Carter 2007).

EGR2, however, plays a critical role in the terminal differentiation stage of human monocytes to macrophages, as identified in numerous studies associating it with AMs. Recent

research using genetic models similar to ours has confirmed the necessity of EGR2, which we further explored, showing its likely integration into the AM epigenome as a direct DNA-bound transcriptional activator and epigenomic marker (McCowan 2021). This is suggested by the enrichment of the EGR motif in chromatin regions that close in the absence of EGR2, while those that open do not show such enrichment. This indicates EGR2 is unlikely to act as a repressor through direct DNA-binding but may have repressive effects through protein interactions or indirect pathways.

Determining the AM EGR2 cistrome will further clarify these mechanisms, especially given the enrichment of C/EBP binding sites where chromatin closes, hinting at possible collaboration between EGR2 and C/EBP in AMs.

Our approach combined chromatin openness and motif analyses with eRNA expression validation to identify direct proximal targets and enhancers that depend on EGR2, which was corroborated by CUT&RUN analysis showing active promoter histone mark H3K4me3. Findings indicated a likely cooperative action between C/EBP and EGR2, aligning with previous studies in human macrophages where EGR2 motifs supported the PU.1-AP-1-C/EBP regulatory complex (Pham 2012).

As for gene activation, EGR2 directly regulates Dectin-1, a key player in antifungal response and phagocytosis, thereby positioning EGR2 upstream of clinically important pathways involved in fungal recognition and clearance.

EGR2 also plays a role in responses to zymosan, a representative pathogen challenge, which are altered in its absence, hinting at distinct specificities for EGR2. This involves genes regulated by EGR2 in steady-state conditions or upon zymosan stimulation, suggesting that chromatin-bound EGR2 might modulate the inducibility of inflammatory gene expression.

Moreover, EGR2 links distinct stimuli with silent bookmarking functions revealed upon exposure to specific conditions, explaining the high number of genomic sites closing in EGR2's absence and their connection to non-cognate stimuli like the zymosan response.

The impact of EGR2 deficiency on lung pathophysiology and its clinical significance

The clinical significance of these findings is multifaceted. Firstly, EGR2 is an evolutionarily conserved transcription regulator in AMs. Detailed analysis of altered gene sets reveals that EGR2 plays a critical role in defining the function of AMs, specifically in phagocytosis and Dectin-1 mediated fungal recognition, internalization, and killing. This gene network is particularly important in the context of lung health, as it relates to conditions such as invasive *Aspergillosis* and fungal allergies, highlighting the need for a specialized transcriptional regulator. Single nucleotide polymorphisms (SNPs) in Dectin-1 have been linked to *Aspergillosis* and other fungal infections in human populations. Our data support the involvement of EGR2 in selective responses against specific pathogens.

Furthermore, histological analysis of lung tissue in both steady-state and following zymosan and *Aspergillus fumigatus* treatment corresponds with observed transcriptional and phenotypical changes. In a steady-state, myeloid-specific deficiency of EGR2 results in increased cellularity in interalveolar spaces, with some mononuclear cells showing larger size and irregular nuclear structures, possibly indicating poorly differentiated AMs. Morphological changes are more pronounced in pathogen-activated inflammatory cells in EGR2-deficient lungs, particularly large macrophage-like inflammatory cells with irregular nuclei, compared to control lungs with wild-type AMs. Additionally, prolonged inflammation with greater fibrosis was noted in EGR2-deficient lungs during zymosan or *AF*-induced inflammation. These fibrosis patterns are morphologically similar to "*bronchiolitis obliterans* with organizing *pneumonia*" (BOOP) in humans.

Using a cyclophosphamide-based immunosuppression model, which mimics the immunocompromised state of patients with invasive *Aspergillosis*, we provided further evidence for increased *aspergilloma* formation and enhanced fibrosis in the lungs. Studies by Perlman and colleagues have shown that monocyte-derived cells are responsible for fibrosis following injury, as AMs are replaced by circulating monocytes over time. However, circulating monocytes are unlikely contributors to the changes observed in our studies, since we analyzed steady-state AMs and the experimental timelines were short (6 and 24 hours for zymosan, and 5 days for *AF*) to expect significant monocyte infiltration.

In addition to monocytes, neutrophil granulocytes are crucial in antifungal responses. AMs regulate neutrophil recruitment, priming, and apoptosis during inflammation, while neutrophils contribute to the reprogramming of macrophages from pro-inflammatory to pro-resolving states. The myeloid-specific EGR2 deficiency may affect polymorphonuclear neutrophils (PMNs), potentially modulating the described complex pathological phenotype.

Interestingly, we observed a reduction in the inflammation-resolving lipid mediator RvE1 in the lungs of EGR2-deficient mice, which may relate to reduced LTA4H levels in EGR2-deficient AMs. RvE1 plays roles in promoting macrophage phagocytosis during zymosan-initiated inflammation resolution and offers protective benefits in asthma and allergic airway inflammation.

VIII. Summary

Our research demonstrates that EGR2 is a crucial epigenomic and transcriptional modulator of alternative polarization and AM gene expression in steady-state and inflammatory conditions. Through distinct mechanisms such as direct transcriptional regulation and silent bookmarking, EGR2 controls cell-type-specific gene expression and function. Given its specific role in AMs, EGR2 presents a potential target for therapeutic intervention using small molecules or through its upstream regulators to modulate AM function and antifungal response.

As summary, in our findings we demonstrated that (1) EGR2 acts as a late-stage regulator of alternative macrophage polarization in BMDMs, and (2) as part of the AM epigenome activating gene expression likely a DNA-bound transcriptional activator. (3) It serves as a proximal nexus regulator for a subset of terminal stage lineage marker genes and numerous phagocytosis-related genes in AMs and (4) regulates Dectin-1 and Dectin-1-mediated phagocytosis of zymosan and fungi. (5) Some zymosan-induced inflammatory events are modulated by myeloid EGR2 as an epigenomic bookmarker, leading to increased and/or newly induced profibrotic cytokines (e.g., CXCL11) and reduced production of resolving lipid mediators (e.g., RvE1) when EGR2 is deficient. (6) Myeloid specific loss of EGR2 in AMs manifests in impaired inflammation resolution and compromised fungal killing during *Aspergillus fumigatus* infection.

IX. Összefoglaló

Kutatásunk bizonyítja, hogy az EGR2 az alternatív makrofág polarizáció és az alveoláris makrofágok génexpressziójának kulcs epigenomikus és transzkripciós modulátora fiziológiás és gyulladásos körülmények között. Mint közvetlen transzkripciós szabályozó és úgynevetett "csendes genomi könyvjelző" szabályozza a sejtspecifikus génexpressziót és funkciókat, illetve a gombaellenes választ.

Összefoglalva, eredményeink által igazoltuk, hogy (1) az EGR2 az alternatív makrofág polarizáció késői stádiumú szabályozójaként működik csontvelői eredetű makrofágokban, illetve (2) valószínű DNS-kötött transzkripciós aktivátorként modulálja az alveoláris makrofágok specifikus génkifejeződést. (3) Proximális nexus szabályozója egyes terminális stádiumban érintett érési marker gén, illetve számos fagocitózishoz kötödő gén expressziójának. (4) Igazoltuk az EGR2 jelentős szerepét a Dectin-1 dependens zimozán és *Aspergillus fumigatus* fagocitózisban, valamint (5) a zimozán által indukált gyulladásos események szabályozásában. A myeloid specifikus EGR2, mint epigenomikus könyvjelző modulálja profibrotikus citokinek (pl. CXCL11) és lipid mediátorok (pl. RvE1) termelését, hiányában ezek kifejeződése és szintézise csökken vagy megszűnik. (6) Az *Aspergillus fumigatus* fertőzés során az EGR2 myeloid specifikus hiánya az *Aspergillus fumigatus* fertőzés során a patogén eliminálási hatékonyságának csökkenésében és gyulladás oldódásának romlásában nyilvánul meg.

X. Keywords

alternative macrophage polarization, bone marrow-derived macrophage, Early Growth Response 2 (EGR2), transcription factor, alveolar macrophage, transcription, epigenomics, phagocytosis, zymosan, *Aspergillus fumigatus*, lung fibrosis

XI. Kulcszavak

alternatív makrofág polarizáció, csontvelői eredetű makrofág, Early Growth Response 2 (EGR2), transzkripciós factor, alveoláris makrofág, transzkripció, epigenomika, fagocitózis, zimozán, *Aspergillus fumigatus*, tüdőfibrózis

XII. Acknowledgements

I would like to express my heartfelt gratitude to all those who have supported me throughout my PhD study.

First and foremost, I would like to thank my supervisor, Prof. Laszlo Nagy for their unwavering support, insightful guidance, and constant encouragement.

I am grateful to Prof. Jozsef Tozser the head of the Department of Biochemistry and Molecular Biology.

I am also thankful for my previous tutors Zoltan Simandi PhD and Zsolt Czimmerer PhD for teach me the basics of scientific work and thinking.

I owe a special thanks to my past and recent colleagues and friends in the Nuclear Receptor Research Laboratory for their camaraderie and collaboration. Especially for Dora Bojcsuk PhD who helped me in the bioinformatical analysis. The discussions we had and the support we provided each other made this challenging journey much easier.

I should acknowledge for all of my collaborators, especially for Zsuzsa Mathene Szigeti PhD and Viktoria Baksa who helped me in the *in vivo* experiments.

I would like to say special thanks to Marta Beladi, Timea Silye-Cseh and Aniko Kerekgyartone Nagy for their technical assistance.

A heartfelt thank you goes to my family for their love, patience, and understanding during the long hours I spent on research.

Finally, I want to express my gratitude to all the participants in my study and anyone else who contributed to my research.

XIII. References

Allard, B., A. Panariti and J. G. Martin (2018). "Alveolar Macrophages in the Resolution of Inflammation, Tissue Repair, and Tolerance to Infection." Front Immunol 9: 1777.

Amit, I., D. R. Winter and S. Jung (2016). "The role of the local environment and epigenetics in shaping macrophage identity and their effect on tissue homeostasis." Nat Immunol 17(1): 18-25.

Atri, C., F. Z. Guerfali and D. Laouini (2018). "Role of Human Macrophage Polarization in Inflammation during Infectious Diseases." Int J Mol Sci 19(6).

Beckmann, A. M. and P. A. Wilce (1997). "Egr transcription factors in the nervous system." Neurochem Int 31(4): 477-510; discussion 517-476.

Bonnardel, J., W. T'Jonck, D. Gaublomme, R. Browaeys, C. L. Scott, L. Martens, B. Vanneste, S. De Prijck, S. A. Nedospasov, A. Kremer, E. Van Hamme, P. Borghgraef, W. Toussaint, P. De Bleser, I. Mannaerts, A. Beschin, L. A. van Grunsven, B. N. Lambrecht, T. Taghon, S. Lippens, D. Elewaut, Y. Saeys and M. Guilliams (2019). "Stellate Cells, Hepatocytes, and Endothelial Cells Imprint the Kupffer Cell Identity on Monocytes Colonizing the Liver Macrophage Niche." Immunity 51(4): 638-654 e639.

Boto, P., T. B. Gerzsenyi, A. Lengyel, B. Szunyog and I. Szatmari (2021). "Zbtb46-dependent altered developmental program in embryonic stem cell-derived blood cell progenitors." Stem Cells 39(10): 1322-1334.

Brown, G. C. (2024). "Cell death by phagocytosis." Nat Rev Immunol 24(2): 91-102.

Caligiuri, M. A. (2008). "Human natural killer cells." Blood 112(3): 461-469.

Carter, J. H. and W. G. Tourtellotte (2007). "Early growth response transcriptional regulators are dispensable for macrophage differentiation." J Immunol 178(5): 3038-3047.

Cheng, P., S. Li and H. Chen (2021). "Macrophages in Lung Injury, Repair, and Fibrosis." Cells 10(2).

Cohen, M., A. Giladi, A. D. Gorki, D. G. Solodkin, M. Zada, A. Hladik, A. Miklosi, T. M. Salame, K. B. Halpern, E. David, S. Itzkovitz, T. Harkany, S. Knapp and I. Amit (2018). "Lung Single-Cell Signaling Interaction Map Reveals Basophil Role in Macrophage Imprinting." Cell 175(4): 1031-1044 e1018.

Collin, M. and F. Ginhoux (2019). "Human dendritic cells." Semin Cell Dev Biol 86: 1-2.

Creyghton, M. P., A. W. Cheng, G. G. Welstead, T. Kooistra, B. W. Carey, E. J. Steine, J. Hanna, M. A. Lodato, G. M. Frampton, P. A. Sharp, L. A. Boyer, R. A. Young and R. Jaenisch (2010). "Histone H3K27ac separates active from poised enhancers and predicts developmental state." Proc Natl Acad Sci U S A 107(50): 21931-21936.

Czimmerer, Z., B. Daniel, A. Horvath, D. Ruckerl, G. Nagy, M. Kiss, M. Peloquin, M. M. Budai, I. Cuaranta-Monroy, Z. Simandi, L. Steiner, B. Nagy, Jr., S. Poliska, C. Banko, Z. Bacso, I. G. Schulman, S. Sauer, J. F. Deleuze, J. E. Allen, S. Benko and L. Nagy (2018). "The Transcription Factor STAT6 Mediates Direct Repression of Inflammatory Enhancers and Limits Activation of Alternatively Polarized Macrophages." Immunity 48(1): 75-90 e76.

Daniel, B., G. Nagy, N. Hah, A. Horvath, Z. Czimmerer, S. Poliska, T. Gyuris, J. Keirsse, C. Gysemans, J. A. Van Ginderachter, B. L. Balint, R. M. Evans, E. Barta and L. Nagy (2014). "The active enhancer network operated by liganded RXR supports angiogenic activity in macrophages." Genes Dev 28(14): 1562-1577.

DiVincenzo, C., C. D. Elzinga, A. C. Medeiros, I. Karbassi, J. R. Jones, M. C. Evans, C. D. Braastad, C. M. Bishop, M. Jaremko, Z. Wang, K. Liaquat, C. A. Hoffman, M. D. York, S. D. Batish, J. R. Lupski and J. J. Higgins (2014). "The allelic spectrum of Charcot-Marie-Tooth disease in over 17,000 individuals with neuropathy." Mol Genet Genomic Med 2(6): 522-529.

Gao, Y., Y. Wang, D. Chauss, A. V. Villarino, V. M. Link, H. Nagashima, C. A. Spinner, V. N. Koparde, N. Bouladoux, M. S. Abers, T. J. Break, L. B. Chopp, J. H. Park, J. Zhu, D. L. Wiest, W. J. Leonard, M. S. Lionakis, J. J. O'Shea, B. Afzali, Y. Belkaid and V. Lazarevic (2023). "Transcription factor EGR2 controls homing and pathogenicity of T(H)17 cells in the central nervous system." Nat Immunol 24(8): 1331-1344.

Gautier, E. L., T. Shay, J. Miller, M. Greter, C. Jakubzick, S. Ivanov, J. Helft, A. Chow, K. G. Elpek, S. Gordonov, A. R. Mazloom, A. Ma'ayan, W. J. Chua, T. H. Hansen, S. J. Turley, M. Merad, G. J. Randolph and C. Immunological Genome (2012). "Gene-expression profiles and transcriptional regulatory pathways that underlie the identity and diversity of mouse tissue macrophages." Nat Immunol 13(11): 1118-1128.

Ginhoux, F. (2014). "Fate PPAR-titioning: PPAR-gamma 'instructs' alveolar macrophage development." Nat Immunol 15(11): 1005-1007.

Giudicelli, F., E. Taillebourg, P. Charnay and P. Gilardi-Hebenstreit (2001). "Krox-20 patterns the hindbrain through both cell-autonomous and non cell-autonomous mechanisms." Genes Dev 15(5): 567-580.

Giudicelli, F., E. Taillebourg, P. Charnay and P. Gilardi-Hebenstreit (2001). "Krox-20 patterns the hindbrain through both cell-autonomous and non cell-autonomous mechanisms." Genes Dev 15(5): 567-580.

Glass, C. K. and G. Natoli (2016). "Molecular control of activation and priming in macrophages." Nat Immunol 17(1): 26-33.

Grandi, F. C., H. Modi, L. Kampman and M. R. Corces (2022). "Chromatin accessibility profiling by ATAC-seq." Nat Protoc 17(6): 1518-1552.

Guilliams, M., I. De Kleer, S. Henri, S. Post, L. Vanhoutte, S. De Prijck, K. Deswarte, B. Malissen, H. Hammad and B. N. Lambrecht (2013). "Alveolar macrophages develop from fetal monocytes that differentiate into long-lived cells in the first week of life via GM-CSF." J Exp Med 210(10): 1977-1992.

Guilliams, M., G. R. Thierry, J. Bonnardel and M. Bajenoff (2020). "Establishment and Maintenance of the Macrophage Niche." Immunity 52(3): 434-451.

Hoeffel, G., Y. Wang, M. Greter, P. See, P. Teo, B. Malleret, M. Leboeuf, D. Low, G. Oller, F. Almeida, S. H. Choy, M. Grisotto, L. Renia, S. J. Conway, E. R. Stanley, J. K. Chan, L. G. Ng, I. M. Samokhvalov, M. Merad and F. Ginhoux (2012). "Adult Langerhans cells derive predominantly from embryonic fetal liver monocytes with a minor contribution of yolk sac-derived macrophages." J Exp Med 209(6): 1167-1181.

Horvath, A., B. Daniel, L. Szeles, I. Cuaranta-Monroy, Z. Czimmerer, L. Ozgyin, L. Steiner, M. Kiss, Z. Simandi, S. Poliska, N. Giannakis, E. Raineri, I. G. Gut, B. Nagy and L. Nagy (2019). "Labelled regulatory elements are pervasive features of the macrophage genome and are dynamically utilized by classical and alternative polarization signals." Nucleic Acids Res 47(6): 2778-2792.

Hou, H., Y. Guo, Q. Chang, T. Luo, X. Wu and X. Zhao (2017). "C-type Lectin Receptor: Old Friend and New Player." Med Chem 13(6): 536-543.

Jarjour, N. N., E. A. Schwarzkopf, T. R. Bradstreet, I. Shchukina, C. C. Lin, S. C. Huang, C. W. Lai, M. E. Cook, R. Taneja, T. S. Stappenbeck, G. J. Randolph, M. N. Artyomov, J. F. Urban, Jr. and B. T. Edelson (2019). "Bhlhe40 mediates tissue-specific control of macrophage proliferation in homeostasis and type 2 immunity." Nat Immunol 20(6): 687-700.

Joshi, N., J. M. Walter and A. V. Misharin (2018). "Alveolar Macrophages." Cell Immunol 330: 86-90.

Kovach, M. A. and T. J. Standiford (2011). "Toll like receptors in diseases of the lung." Int Immunopharmacol 11(10): 1399-1406.

Lavin, Y., D. Winter, R. Blecher-Gonen, E. David, H. Keren-Shaul, M. Merad, S. Jung and I. Amit (2014). "Tissue-resident macrophage enhancer landscapes are shaped by the local microenvironment." Cell 159(6): 1312-1326.

Lazarov, T., S. Juarez-Carreno, N. Cox and F. Geissmann (2023). "Physiology and diseases of tissue-resident macrophages." Nature 618(7966): 698-707.

Liao, X., N. Sharma, F. Kapadia, G. Zhou, Y. Lu, H. Hong, K. Paruchuri, G. H. Mahabeleshwar, E. Dalmas, N. Venteclef, C. A. Flask, J. Kim, B. W. Doreian, K. Q. Lu, K. H. Kaestner, A. Hamik, K. Clement and M. K. Jain (2011). "Kruppel-like factor 4 regulates macrophage polarization." J Clin Invest 121(7): 2736-2749.

Liew, P. X. and P. Kubes (2019). "The Neutrophil's Role During Health and Disease." Physiol Rev 99(2): 1223-1248.

Machado, M., J. Fortun and P. Munoz (2024). "Invasive aspergillosis: A comprehensive review." Med Clin (Barc) 163(4): 189-198.

McCowan, J., F. Fercoq, P. M. Kirkwood, W. T'Jonck, L. M. Hegarty, C. M. Mawer, R. Cunningham, A. S. Mirchandani, A. Hoy, D. C. Humphries, G. R. Jones, C. G. Hansen, N. Hirani, S. J. Jenkins, S. Henri, B. Malissen, S. R. Walmsley, D. H. Dockrell, P. T. K. Saunders, L. M. Carlin and C. C. Bain (2021). "The transcription factor EGR2 is indispensable for tissue-specific imprinting of alveolar macrophages in health and tissue repair." Sci Immunol 6(65): eabj2132.

Meers, M. P., T. D. Bryson, J. G. Henikoff and S. Henikoff (2019). "Improved CUT&RUN chromatin profiling tools." Elife 8.

Morita, K., T. Okamura, S. Sumitomo, Y. Iwasaki, K. Fujio and K. Yamamoto (2016). "Emerging roles of Egr2 and Egr3 in the control of systemic autoimmunity." Rheumatology (Oxford) 55(suppl 2): ii76-ii81.

Murase, M., T. Kawasaki, R. Hakozaki, T. Sueyoshi, D. D. P. Putri, Y. Kitai, S. Sato, M. Ikawa and T. Kawai (2018). "Intravesicular Acidification Regulates Lipopolysaccharide Inflammation and Tolerance through TLR4 Trafficking." J Immunol 200(8): 2798-2808.

Nakato, R. and T. Sakata (2021). "Methods for ChIP-seq analysis: A practical workflow and advanced applications." Methods 187: 44-53.

Odegaard, J. I., R. R. Ricardo-Gonzalez, M. H. Goforth, C. R. Morel, V. Subramanian, L. Mukundan, A. Red Eagle, D. Vats, F. Brombacher, A. W. Ferrante and A. Chawla (2007). "Macrophage-specific PPARgamma controls alternative activation and improves insulin resistance." Nature 447(7148): 1116-1120.

Onomoto, K., K. Onoguchi and M. Yoneyama (2021). "Regulation of RIG-I-like receptor-mediated signaling: interaction between host and viral factors." Cell Mol Immunol 18(3): 539-555.

Palstra, R. J. and F. Grosveld (2012). "Transcription factor binding at enhancers: shaping a genomic regulatory landscape in flux." Front Genet 3: 195.

Pan, Y., Y. Yu, X. Wang and T. Zhang (2020). "Tumor-Associated Macrophages in Tumor Immunity." Front Immunol 11: 583084.

Pello, O. M., M. De Pizzol, M. Mirolo, L. Soucek, L. Zammataro, A. Amabile, A. Doni, M. Nebuloni, L. B. Swigart, G. I. Evan, A. Mantovani and M. Locati (2012). "Role of c-MYC in alternative activation of human macrophages and tumor-associated macrophage biology." Blood 119(2): 411-421.

Pham, T. H., C. Benner, M. Lichtinger, L. Schwarzfischer, Y. Hu, R. Andreesen, W. Chen and M. Rehli (2012). "Dynamic epigenetic enhancer signatures reveal key transcription factors associated with monocytic differentiation states." Blood 119(24): e161-171.

Satoh, T., O. Takeuchi, A. Vandenbon, K. Yasuda, Y. Tanaka, Y. Kumagai, T. Miyake, K. Matsushita, T. Okazaki, T. Saitoh, K. Honma, T. Matsuyama, K. Yui, T. Tsujimura, D. M. Standley, K. Nakanishi, K. Nakai and S. Akira (2010). "The Jmjd3-Irf4 axis regulates M2 macrophage polarization and host responses against helminth infection." Nat Immunol 11(10): 936-944.

Schneider, C., S. P. Nobs, M. Kurrer, H. Rehrauer, C. Thiele and M. Kopf (2014). "Induction of the nuclear receptor PPAR-gamma by the cytokine GM-CSF is critical for the differentiation of fetal monocytes into alveolar macrophages." Nat Immunol 15(11): 1026-1037.

Shapouri-Moghaddam, A., S. Mohammadian, H. Vazini, M. Taghadosi, S. A. Esmaeili, F. Mardani, B. Seifi, A. Mohammadi, J. T. Afshari and A. Sahebkar (2018). "Macrophage plasticity, polarization, and function in health and disease." J Cell Physiol 233(9): 6425-6440.

Shibata, Y., P. Y. Berclaz, Z. C. Chroneos, M. Yoshida, J. A. Whitsett and B. C. Trapnell (2001). "GM-CSF regulates alveolar macrophage differentiation and innate immunity in the lung through PU.1." Immunity 15(4): 557-567.

Snaka, T. and N. Fasel (2020). "Behind the Scenes: Nod-Like Receptor X1 Controls Inflammation and Metabolism." Front Cell Infect Microbiol 10: 609812.

Trapnell, B. C. and J. A. Whitsett (2002). "Gm-CSF regulates pulmonary surfactant homeostasis and alveolar macrophage-mediated innate host defense." Annu Rev Physiol 64: 775-802.

Vassiliou, E. and R. Farias-Pereira (2023). "Impact of Lipid Metabolism on Macrophage Polarization: Implications for Inflammation and Tumor Immunity." Int J Mol Sci 24(15).

Videla, L. A., R. Valenzuela, A. Del Campo and J. Zuniga-Hernandez (2023). "Omega-3 Lipid Mediators: Modulation of the M1/M2 Macrophage Phenotype and Its Protective Role in Chronic Liver Diseases." Int J Mol Sci 24(21).

Vivier, E., D. Artis, M. Colonna, A. Diefenbach, J. P. Di Santo, G. Eberl, S. Koyasu, R. M. Locksley, A. N. J. McKenzie, R. E. Mebius, F. Powrie and H. Spits (2018). "Innate Lymphoid Cells: 10 Years On." Cell 174(5): 1054-1066.

Withanage, M. H. H., H. Liang and E. Zeng (2022). "RNA-Seq Experiment and Data Analysis." Methods Mol Biol 2418: 405-424.

Wynn, T. A. and K. M. Vannella (2016). "Macrophages in Tissue Repair, Regeneration, and Fibrosis." Immunity 44(3): 450-462.

Yu, X., A. Buttgereit, I. Lelios, S. G. Utz, D. Cansever, B. Becher and M. Greter (2017). "The Cytokine TGF-beta Promotes the Development and Homeostasis of Alveolar Macrophages." Immunity 47(5): 903-912 e904.

XIV. List of publications

UNIVERSITY AND NATIONAL LIBRARY
UNIVERSITY OF DEBRECEN
H-4002 Egyetem tér 1, Debrecen
Phone: +3652/410-443, email: publikaciok@lib.unideb.hu

Registry number: DEENK/535/2024.PL
Subject: PhD Publication List

Candidate: Zsuzsanna Kolostyák
Doctoral School: Doctoral School of Molecular Cellular and Immune Biology
MTMT ID: 10075231

List of publications related to the dissertation

1. **Kolostyák, Z.**, Bojcsuk, D., Baksa, V., Máthéné Szigeti, Z., Bene, K., Czimmerer, Z., Botó, P., Fadel, L., Póliska, S., Halász, L., Tzerpos, P., Berger, W. K., Villabona-Rueda, A., Varga, Z., Kovács, T., Patsalos, A., Pap, A., Vámosi, G., Bai, P., Dezső, B., Spite, M., D'Alessio,, F. R., Szatmári, I., Nagy, L.: EGR2 is an epigenomic regulator of phagocytosis and antifungal immunity in alveolar macrophages.
JCI Insight. 9 (17), 1-21, 2024.
DOI: http://dx.doi.org/10.1172/jci.insight.164009
IF: 6.3 (2023)

2. Dániel, B., Czimmerer, Z., Halász, L., Botó, P., **Kolostyák, Z.**, Póliska, S., Berger, W. K., Tzerpos, P., Nagy, G., Horváth, A., Hajas, G., Silye-Cseh, T., Nagy, A., Sauer, S., Francois-Deleuze, J., Szatmári, I., Bácsi, A., Nagy, L.: The transcription factor EGR2 is the molecular linchpin connecting STAT6 activation to the late, stable epigenomic program of alternative macrophage polarization.
Genes Dev. 34 (21-22), 1474-1492, 2020.
DOI: http://dx.doi.org/10.1101/gad.343038.120
IF: 11.361

List of other publications

3. Jambrovics, K., Botó, P., Pap, A., Sarang, Z., **Kolostyák, Z.**, Czimmerer, Z., Szatmári, I., Fésüs, L., Uray, I. P., Balajthy, Z.: Transglutaminase 2 associated with PI3K and PTEN in a membrane-bound signalosome platform blunts cell death.
Cell Death Dis. 14 (3), 1-10, 2023.
DOI: http://dx.doi.org/10.1038/s41419-023-05748-6
IF: 8.1

4. Czimmerer, Z., Halász, L., Dániel, B., Varga, Z., Bene, K., Domokos, A., Hoeksema, M., Shen, Z., Berger, W. K., Silye-Cseh, T., Jambrovics, K., **Kolostyák, Z.**, Fenyvesi, F., Váradi, J., Póliska, S., Hajas, G., Szatmári, I., Glass, C. K., Bácsi, A., Nagy, L.: The epigenetic state of IL-4-polarized macrophages enables inflammatory cistromic expansion and extended synergistic response to TLR ligands.
Immunity. 55 (11), 2006-2026, 2022.
DOI: http://dx.doi.org/10.1016/j.immuni.2022.10.004
IF: 32.4

5. Fadel, L., Rehó, B., Volkó, J., Bojcsuk, D., **Kolostyák, Z.**, Nagy, G., Müller, G., Simándi, Z., Hegedűs, É., Szabó, G., Tóth, K., Nagy, L., Vámosi, G.: Agonist binding directs dynamic competition among nuclear receptors for heterodimerization with retinoid X receptor.
J. Biol. Chem. 295 (29), 10045-10061, 2020.
DOI: http://dx.doi.org/10.1074/jbc.RA119.011614
IF: 5.157

6. Simándi, Z., Pájer, K., Károlyi, K., Sieler, T., Jiang, L. L., **Kolostyák, Z.**, Sári, Z., Fekecs, Z., Pap, A., Patsalos, A., Contreras, G. A., Rehó, B., Papp, Z., Guo, X., Horváth, A., Kiss, G., Keresztessy, Z., Vámosi, G., Hickman, J., Xu, H., Dormann, D., Hortobágyi, T., Antal, M., Nógrádi, A., Nagy, L.: Arginine Methyltransferase PRMT8 Provides Cellular Stress Tolerance in Aging Motoneurons.
J. Neurosci. 38 (35), 7683-7700, 2018.
DOI: http://dx.doi.org/10.1523/JNEUROSCI.3389-17.2018
IF: 6.074

7. Czimmerer, Z., Horváth, A., Dániel, B., Nagy, G., Cuaranta-Monroy, I., Kiss, M., **Kolostyák, Z.**, Póliska, S., Steiner, L., Giannakis, N., Varga, T., Nagy, L.: Dynamic transcriptional control of macrophage miRNA signature via inflammation responsive enhancers revealed using a combination of next generation sequencing-based approaches.
Biochim. Biophys. Acta. Gene Regul. Mech. 1861 (1), 14-28, 2018.
DOI: http://dx.doi.org/10.1016/j.bbagrm.2017.11.003
IF: 4.599

8. Dániel, B., Nagy, G., Czimmerer, Z., Horváth, A., Hammers, D. W., Cuaranta-Monroy, I., Póliska, S., Tzerpos, P., **Kolostyák, Z.**, Hays, T. T., Patsalos, A., Houtman, R., Sauer, S., Francois-Deleuze, J., Rastinejad, F., Bálint, B. L., Sweeney, H. L., Nagy, L.: The Nuclear Receptor PPAR[gamma] Controls Progressive Macrophage Polarization as a Ligand-Insensitive Epigenomic Ratchet of Transcriptional Memory.
Immunity. 49 (4), 615-626, 2018.
DOI: http://dx.doi.org/10.1016/j.immuni.2018.09.005
IF: 21.522

UNIVERSITY AND NATIONAL LIBRARY
UNIVERSITY OF DEBRECEN
H-4002 Egyetem tér 1, Debrecen
Phone: +3652/410-443, email: publikaciok@lib.unideb.hu

9. Kiss, M., Czimmerer, Z., Nagy, G., Bieniasz-Krzywiec, P., Ehling, M., Pap, A., Póliska, S., Botó, P., Tzerpos, P., Horváth, A., **Kolostyák, Z.**, Dániel, B., Szatmári, I., Mazzone, M., Nagy, L.: Retinoid X receptor suppresses a metastasis-promoting transcriptional program in myeloid cells via a ligand-insensitive mechanism.
Proc. Natl. Acad. Sci. U. S. A. 114 (40), 10725-10730, 2017.
DOI: http://dx.doi.org/10.1073/pnas.1700785114
IF: 9.504

10. Cuaranta-Monroy, I., Simándi, Z., **Kolostyák, Z.**, Doan-Xuan, Q. M., Póliska, S., Horváth, A., Nagy, G., Bacsó, Z., Nagy, L.: Highly efficient differentiation of embryonic stem cells into adipocytes by ascorbic acid.
Stem Cell Res. 13 (1), 88-97, 2014.
DOI: http://dx.doi.org/10.1016/j.scr.2014.04.015
IF: 3.693

Total IF of journals (all publications): 108,71
Total IF of journals (publications related to the dissertation): 17,661

The Candidate's publication data submitted to the iDEa Tudóstér have been validated by DEENK on the basis of the Journal Citation Report (Impact Factor) database.

29 October, 2024